# Estimation of the sensitivity of Picea abies and Fagus sylvatica to the effects of abiotic stresses

Laboratory of Tandetron

Pavel Coufalík

Proposal ID

267

**Report regarding proposal "Estimation of the sensitivity of *Picea abies* and *Fagus sylvatica* to the effects of abiotic stresses"**

P. Coufalík, Institute of Analytical Chemistry of the CAS, Brno, Czech Republic
K. Večeřová, Global Change Research Institute of the CAS, Brno, Czech Republic
V. Havránek, Nuclear Physics Institute of the CAS, Řež, Czech Republic

The trees of *Picea abies* and *Fagus sylvatica* were exposed to CdO nanoparticles (NPs) generated in thermal reactor [1]. The experiment was performed as one and two week's exposure in chambers at two concentration levels of NPs. The number of NPs at the size between 7 and 60 nm was approximately 2 $e^5$ particles/$cm^3$, and 4.4 $e^6$ particles/$cm^3$ at the maximum concentration. The eight cuts of *Picea abies* needles (the thickness of 10 and 20 µm, cross sections and longitudinal cuts), and four cuts of *Fagus sylvatica* leaves (10 and 20 µm, cross and surface sections) were prepared on the cryotome.
The samples were subjected to the PIXE (stoma on the Fig. 1.) and STIM during four days (31.5.–1.6. and 12.–13.10.) from the allocated beamdays. The resolution was approximately 1 µm at E = 2.9 MeV. The limit of detection of cadmium was 2 µg/g. The presence of cadmium on the surface of samples was confirmed by scattered beam, however, no cadmium was detected inside the stomata.
The total contents of cadmium in samples at the highest NPs concentrations were 2.3 and 2.1 µg/g for *Picea abies* and *Fagus sylvatica*, respectively. The phytotoxicity of CdO NPs has already been observed at lower concentration levels (e.g. a decrease of photosynthetic pigments). A serious damage of plants occurred after the first week of the experiment at high concentrations of NPs. Therefore, tested concentrations are critical to the carrying out of the experiment, and cannot be further increased. Thus, the use of PIXE for the imaging of NPs in leaf interiors appears to be problematic due to an insufficient limit of quantification of the method.

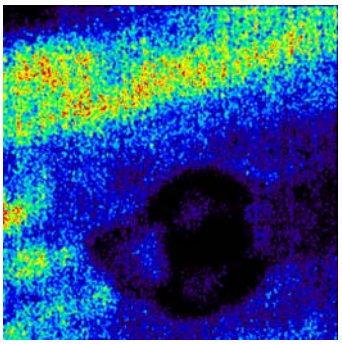

Fig. 1. Stoma of *Picea abies* needle imaged by the absence of calcium (100 x 100 µm)

**Reference**

1. L. Bláhová, J. Kohoutek, J. Lebedová, L. Bláha, Z. Večeřa, M. Buchtová, I. Míšek, K. Hilscherová, Anal. Bioanal. Chem. 406 (2014) 5867.

# Heavy Ion Micromachining of Optical Devices

Laboratory of Tandetron

István Rajta

Proposal ID

142

**21 May 2015 at 12:10**

# Design and fabrication of waveguides and optical gratings in crystals and glasses via swift heavy ion irradiation

BANYASZ, Istvan 1*; OLIVARES VILLEGAS, José 2; BERNESCHI, Simone 3; PELLI, Stefano 4; NUNZI CONTI, Gualtiero 3; RIGHINI, Giancarlo 5; PEÑA RODRIGUEZ, Ovidio 6; RAJTA, István 7; NAGY, Gyula 7; HAVRANEK, Vladimir 8; VOSECEK, Vaclav 8; ZOLNAI, Zsolt 9; VERES, Miklos 1; HIMICS, Laszlo 1

1 Wigner Research Centre for Physics, Budapest, Hungary; 2 Instituto de Óptica 'Daza de Valdés', CSIC, Madrdi, Spain; 3 Instituto di Fisica Applicata"Nello Carrara", Sesto Fiorentino, Italy; 4 Instituto di Fisica "Nello Carrara", Sesto Fiorentino, Italy; 5 “Enrico Fermi” Center for Study and Research; 6 Institute of Nuclear Fusión, Universidad Politécnica de Madrid, Spain; 7 Institute of Nuclear Research of the Hungarian Academy of Sciences. Debrecen, Hungary; 8 Nuclear Physics Institute of the ASCR, Rez, Czech Republic; 9 Centre for Energy Research of the Hungarian Academy of Sciences, Budapest, Hungary

Active and passive optical waveguides are fundamental elements in modern telecommunications systems. A great number of optical crystals and glasses were identified and are used as good optoelectronic materials. However, fabrication of waveguides in some of those materials remains still a challenging task due to their susceptibility to mechanical or chemical damages during processing. Researches were initiated on ion beam fabrication of optical waveguides in tellurite glasses. Channel waveguides were written in Er: $TeO_2$–$WO_3$ glass through a special silicon mask using 1.5 MeV N+ irradiation. This method was improved by increasing N+ energy to 3.5 MeV to achieve confinement at the 1550 nm wavelength, too. An alternative method, direct writing of the channel waveguides in the tellurite glass using focussed beams of 6–11 MeV C3+ and C5+ and 5 and 10 MeV N3+, has also been developed. Channel waveguides were fabricated in undoped eulytine- ($Bi_4Ge_3O_{12}$) and sillenite type ($Bi_{12}GeO_{20}$) bismuth germanate crystals using both a special silicon mask and a thick SU8 photoresist mask and 3.5 MeV N+ irradiation. By using even higher energy irradiation, 25 MeV C5+ at low doses, planar optical waveguides were fabricated in sillenite-type BGO crystal.
Focussed ion beam (11 MeV C3+, 10 MeV N3+) irradiation was also used to fabricate transmission optical gratings in Pyrex and Er:
TeO2–WO3 glasses, sillenite type BGO and LiNbO3 crystals. The waveguides were studied by phase contrast and interference microscopy and micro Raman spectroscopy. Guiding properties were checked by using m-line spectroscopy and the end fire method.

# Study of isotopically enriched (10B/11B and 12C/13C  boron doped diamond layers grown using MW PECVD

Neutron Physics Laboratory - Nuclear analytical methods with neutrons

Andy  Taylor

Proposal ID

271

# Report regarding proposal "Study of isotopically enriched ($^{10}$B/$^{11}$B and $^{12}$C/$^{13}$C boron doped diamond layers grown using MW PECVD"

A. Taylor and V. Mortet, Institute of Physics, Academy of Sciences CR, Czech Republic

O. Frank, J. Heyrovsky Institute of Physical Chemistry, Academy of Sciences CR, Prague, Czech Republic

J. Vacik, Nuclear Physics Institute, Rez, Czech Republic

Within the framework of the "Study of isotopically enriched ($^{10}$B/$^{11}$B and $^{12}$C/$^{13}$C boron doped diamond layers grown using MW PECVD" a set of boron-doped diamond layers have been evaluated using several analytical techniques, amongst them Neutron Depth Profiling, Hall effect measurement, SIMS (final results pending) and Raman spectroscopy (plus standard morphology characterization by SEM and AFM). The current data gathered (see table below) shows slight discrepancies between the boron concentrations obtained by NDP and the carrier concentration obtained by Hall effect.

| | | | NDP – $^{10}$B atomic concentration (at.cm$^{3}$) | Hall – concentration (cm$^{-3}$) |
|---|---|---|---|---|
| B/C: 500 ppm | $^{13}$C | $^{11}$B | 5.5 x $10^{20}$ | 3.34 x $10^{20}$ |
| | $^{13}$C | $^{10}$B | 9.0 x $10^{20}$ | 3.54 x $10^{19}$ |
| B/C: 3000 ppm | $^{13}$C | $^{11}$B | 20 x $10^{20}$ | 1.15 x $10^{21}$ |
| | $^{13}$C | $^{10}$B | 65 x $10^{20}$ | 5.65 x $10^{20}$ |

Even though some discrepancies can be expected, the observed trends provoke deeper insights into the phenomena of boron incorporation into the diamond lattice and carrier activation/suppression. These issues are currently being addressed with a more detailed analysis of the Hall effect data. Once there is more clarity in the obtained information, the measured boron/carrier concentrations will be used for modelling of Raman spectra and consequently for the elucidation of the origins of so-far debated Raman features in BDD at 500 and 1200 cm-1 (see figure below).

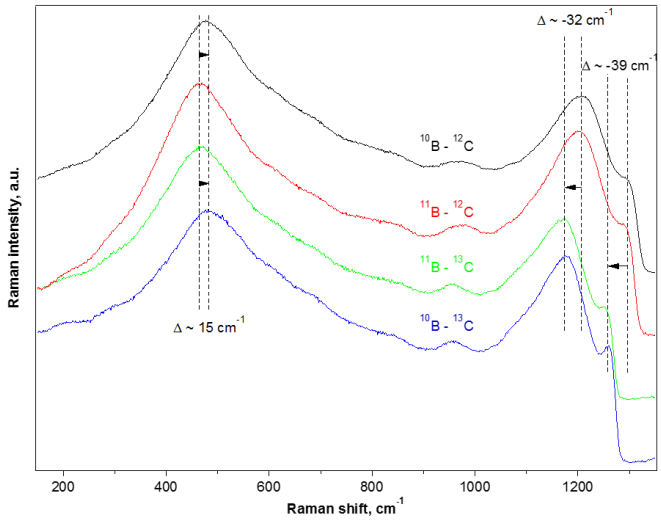


*Raman spectra (laser excitation 633 nm) of nano-crystalline boron doped diamond layers with 3000 ppm B/C content in the gas phase. Isotopic composition is indicated for each spectrum (note: $^{11}$B denotes natural boron concentration, i.e., 80 % $^{11}$B and 20 % $^{10}$B). Dashed vertical lines with horizontal arrows show the maximum shifts of the principal Raman features from the $^{11}$B-$^{12}$C BDD (natural isotopic composition). The spectra are normalized to the amplitude of the ~ 500 cm$^{-1}$ feature and offset for clarity.*

# Heavy ion micromachining on PDMS

Laboratory of Tandetron

István Rajta

Proposal ID

143

# PDMS compaction by heavy ions

A.T.T. Szabó[1], S.Z. Szilasi[1], G.U.L. Nagy[1], R. Huszánk, V. Havranek[2], V. Vosecek[2], V. Lavrentiev[2] and I. Rajta[1]

[1]MTA Atomki, Institute for Nuclear Research, Hungarian Academy of Sciences,
H-4001 Debrecen, P.O. Box 51, Hungary
[2]Nuclear Physics Institute AV CR, Řež near Prague, 250 68, Czech Republic

***Basis:***

1) Poly(dimethylsiloxane) (PDMS) irradiated with high energy ion beam suffers compaction due to the chemical changes in the material [1].
2) In the case of patterned irradiations, the surface between the irradiated and unirradiated areas has regular curvature thanks to its elastic nature [2].

***Importance:*** Practical applications in proton beam writing (PBW) technique, for instance creation of microlenses [3].

***Present aim:***

1) Study of the effects of ion fluence and surface patterning on compaction in the PDMS irradiated by high-energy $C^{4+}$ and $N^{4+}$ ions using atomic force microscopy.
2) Demonstration of the possible applications of these results through the realization of convex microlenses.

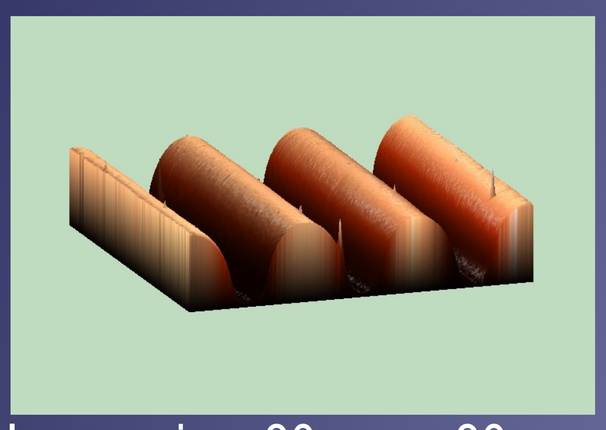

Image size: 80 μm x 80 μm

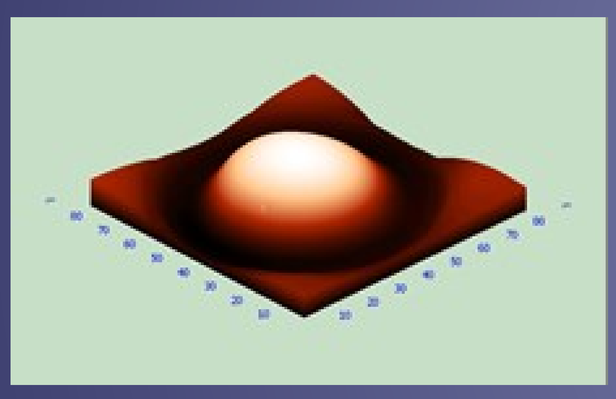

Image size: 80 μm x 80 μm

***Irradiation facility:*** 3 MV Tandetron accelerator (INP ASCR)
***Microbeam parameters:*** 1μm × 1μm spot size; 1mm × 1mm scan size; 11.535 MeV $C^{4+}$ ions, and 10.5 MeV $N^{4+}$ Ions
***Samples:*** PDMS made of Sylgard 184 kit (Dow-Corning) spin coated in 15μm thickness onto glass substrate.
***The micropatterns fabricated by the microbeam:***

1) Parallel stripes with width/spacing of
   15μm/30μm; 25μm/50μm; 25μm /100μm;
   fluences 0.5 – 500 nC/mm$^2$ ($1.6 \times 10^{10}$ – $3.1 \times 10^{13}$ ions/cm$^2$).
2) Convex microlenses with diameter of d=60μm;
   fluences 30 – 300 nC/mm$^2$ ($3.1 \times 10^{10}$ – $4.0 \times 10^{12}$ ions/cm$^2$).

***Characterization method:*** Atomic force microscopy (NTEGRA AFM microscope, NT-MDT, NPI facility).

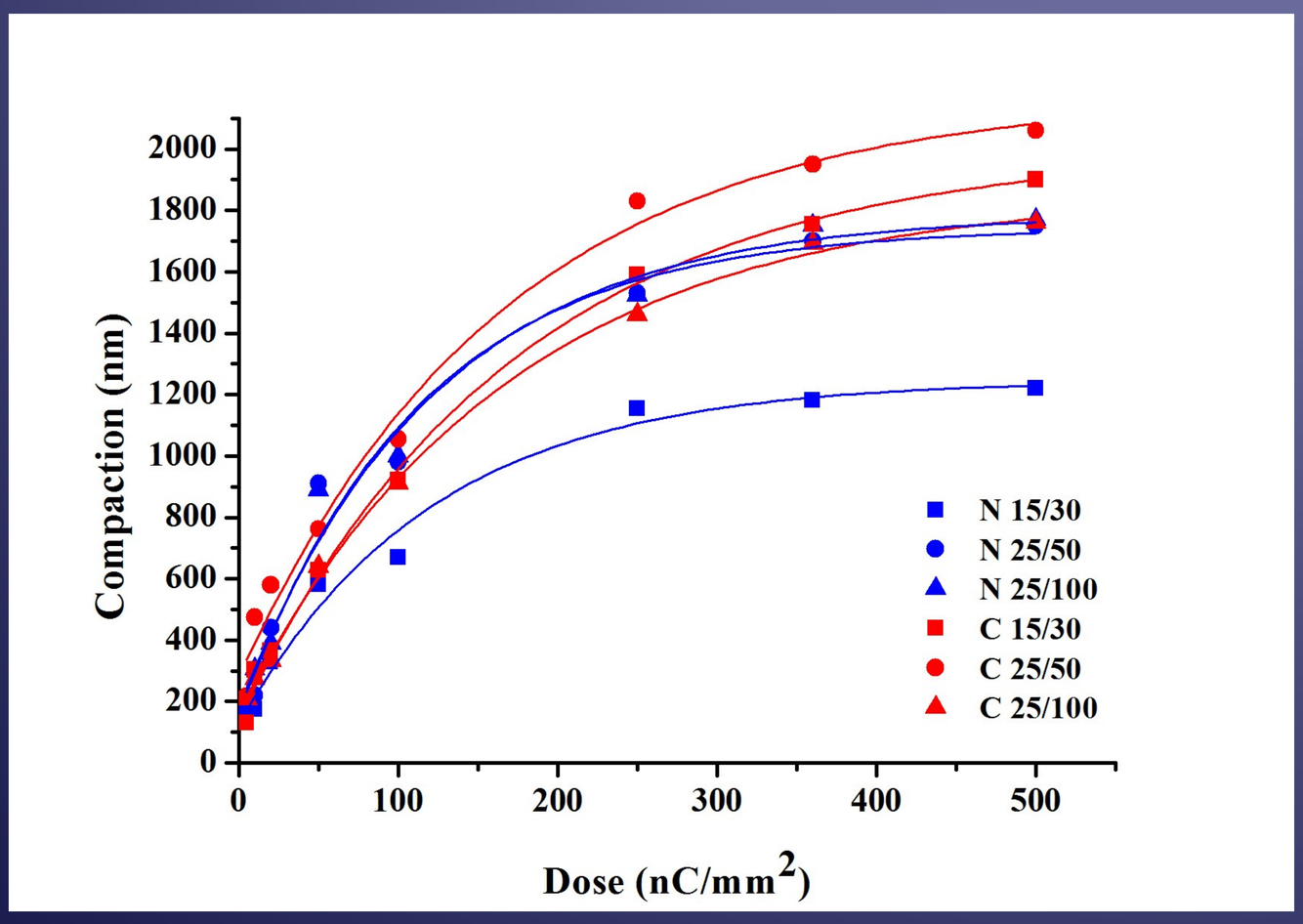


Topography image

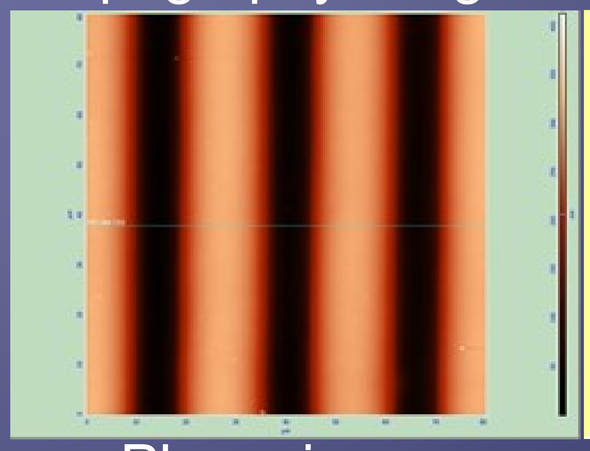

X profile

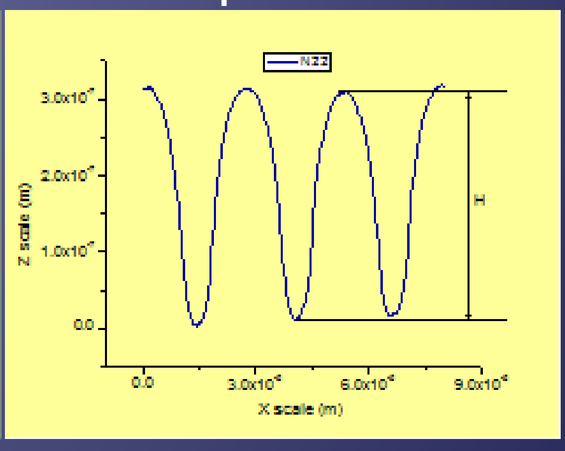


Phase image

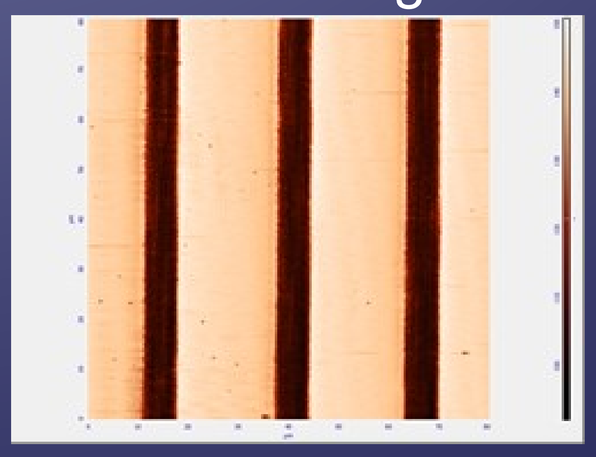

The typical AFM results taken from the stripes-like patterned PDMS.
The presented "phase image" confirms the chemical changes in PDMS upon the irradiation.

***Conclusion:*** The degree of PDMS compaction gradually increases with fluence demonstrating a tendency to be saturated at the highest fluences for both kinds of the applied ions. In case of the $N^{4+}$ ions the saturated compaction is achieved at lower fluences as compared with that for the $C^{4+}$ irradiated PDMS.

***References:***

1) S.Z. Szilasi, R. Huszánk, A. Csik, Cs. Cserháti, I. Rajta: *PDMS patterning by proton beam*. NIMB 267 (2009) 2296.
2) S.Z. Szilasi, J. Kokavecz, R. Huszánk, I. Rajta: *Compaction of PDMS due to proton beam irradiation*. Appl. Surf. Sci. 257 (2011) 4612.
3) S.Z. Szilasi, N. Hegman, A. Csik, I. Rajta: *Creation of convex microlenses in PDMS with focused MeV ion beam*. Microelectr. Eng. 88 (2011) 2885.

This work was supported by the TAMOP 4.2.2.A-11/1/KONV-2012-0036 project, which is co-financed by the European Union and European Social Fund.

# Boron doped nano-crystalline diamond growth by MW-LA-PECVD: temperature and boron precursor effects

Neutron Physics Laboratory - Nuclear analytical methods with neutrons

Andy Taylor

Proposal ID

272

# Report regarding proposal “Boron doped nano-crystalline diamond growth by MW-LA-PECVD: temperature and boron precursor effects”

A. Taylor, P. Ashcheulov and V. Mortet, Institute of Physics, Academy of Sciences CR, Czech Republic

J. Vacik, Nuclear Physics Institute, Rez, Czech Republic

The electrical conductivity of the boron doped nanocrystalline diamond (BNCD) layers deposited by microwave plasma enhanced chemical vapour deposition with linear antenna delivery (MW-LA-PECVD) has been shown to be lower in comparison to layers deposited using conventional microwave deposition systems. In this study we investigate the effect of temperature and boron precursor (trimethylboron vs diborane) with the aim of producing layers with higher conductivity.

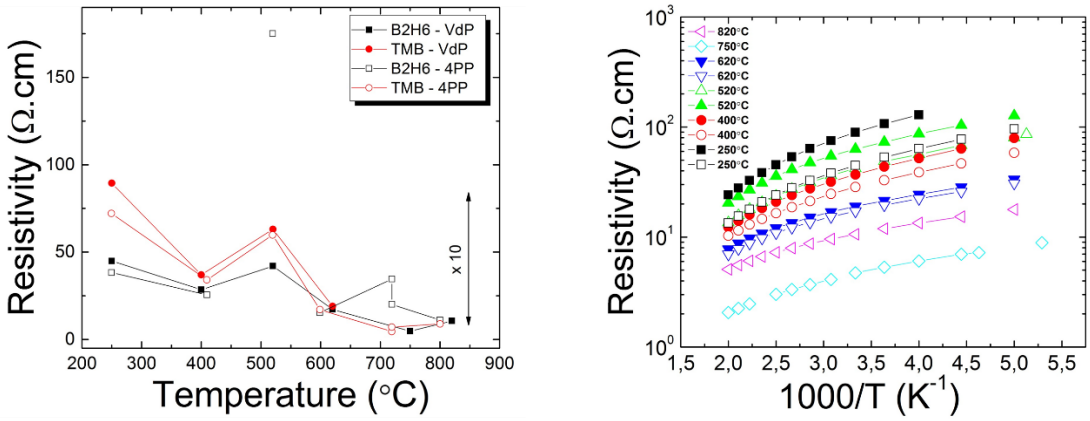


Fig. 1 Electrical resistivity measurements showing a 10 times decrease in resistivity values as the growth temperature increases. However, no differences are observed for changes in precursor.

Neutron depth profile measurements were performed on BNCD samples prepared with each precursor and grown at the highest (800 °C) and lowest (250 °C) temperatures in order to further clarify the above electrical resistivity results.

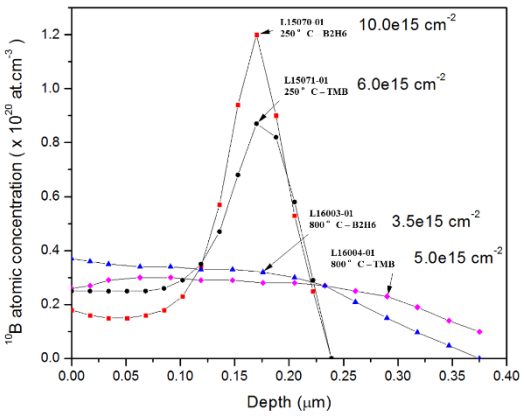


Fig. 2 (left) shows rather consistent levels of $^{10}B$ for both samples grown at the highest temperature, whilst for the samples grown at the lowest temperature a sharp rise is observed close to the layer/substrate interface, it is not clear why this occurs. Interestingly, where the profiles are “flat” the difference in $^{10}B$ content differs only by 2x compared to the 10x increase seen from the electrical measurements. However, overall levels are lower than that of previously reported BNCD layers with high conductivity (5 x $10^{20}$ at.cm$^{-3}$) [1], therefore further work is in progress to further tune the growth chemistry to attain such layers.

*[1] A. Taylor et al: Diam. Relat. Mater. 47 (2014) 27 - 34*

# Preparation, modification and characterization of materials by radiation

Laboratory of Tandetron

Marie Davidkova

Proposal ID

18

**Report regarding proposal "Preparation, modification and characterization of materials by radiation"**

**M. Davídková, A. Michaelidesová, J. Vachelová, Nuclear Physics Institute of the CAS, Řež, Czech Republic**
**L. Bačáková, M. Vandrovcová, Institute of Physiology of the CAS, Prague, Czech Republic**

External microbeam of Tandetron accelerator has been applied to study response of normal cell line to ionizing radiation of different quality. Biological efficiency of proton and alpha particle beams was compared. Human normal neonatal skin fibroblasts were irradiated by 1.1 MeV proton and 2.5 MeV alpha particle beams. Cells were grown on Lumox dishes with Teflon bottom membrane (Sarstedt) in Dulbecco's Modified Eagle's medium (Sigma-Aldrich) supplemented with 15% fetal bovine serum (FBS—BIOSERA) and standard antibiotics (100 U/ml penicillin and 0.1 mg/ml streptomycin (Sigma-Aldrich). Confluent cell monolayers were irradiated by doses 0.5, 1, 3 and 5 Gy of protons or alpha particles. Biological response of fibroblasts to acute irradiation was assessed using clonogenic and micronuclei formation assays.

Colony formation analysis as survival test was performed for 250 or 500 cells per dish growing during 14 days in standard conditions for cell cultivation. Photo of dishes with colonies obtained by seeding of 500 cells per dish irradiated by 0, 0.5, 1, 3, 5 Gy of alpha particle beam is shown on figure 1a.

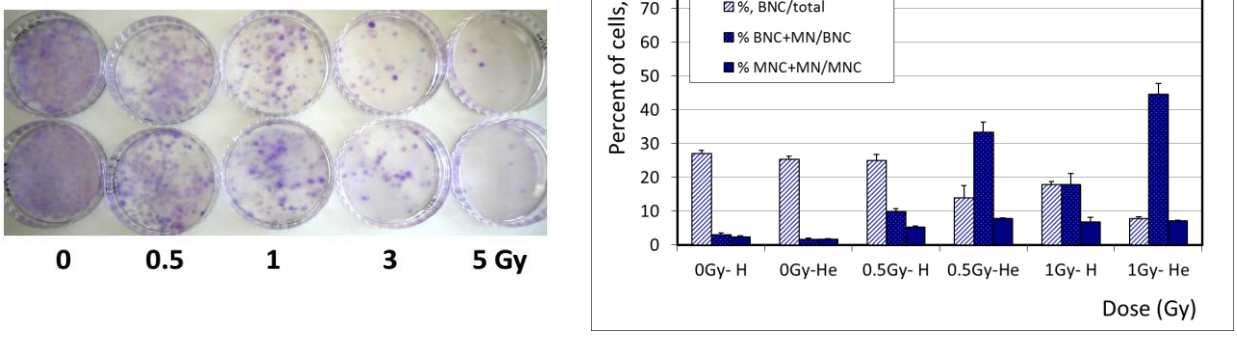


a) b)

Figure 1: a) colony formation of human fibroblasts irradiated by alpha particles. b) micronuclei formation in human neonatal fibroblasts after irradiation by different doses of protons and alpha particles.

Results of micronuclei formation test for alpha and proton irradiation at the same dose range show that alpha particles cause heavier DNA damage. For instance, 45% binuclear cells (BNC) containing micronuclei (MN) has been observed after irradiation by 1 Gy of alpha particles in comparison to about 18% BNC+MN after proton irradiation (figure 1b). Higher doses of alpha irradiation induced also cell senescence, which was not observed in proton-irradiated cells. Further increase of MN formation after 3-5 Gy alpha-irradiation was stopped by the replicative senescence in alpha-irradiation treated cells but not in proton-irradiated.

This pilot study was supported by the project of the Czech Science Foundation No. P108/12/G108.

# Effect of high LET radiation on specific interaction of proteins with DNA.

Laboratory of Cyclotron and Fast Neutron Generators

Marie Davidkova

Proposal ID

21

## Průběžná zpráva o realizaci projektu za rok 2012

Projekt je řešen jako příspěvek řešitelského týmu k mezinárodnímu projektu COST MP1002 "Nano-scale insights in ion beam cancer therapy (Nano-IBCT, Nano-aspekty iontové terapie nádorů)“. Řešitelská laboratoř je součástí pracovní skupiny WG5 Radiobiologické efekty (detekce dvojných zlomů DNA, predikce a buněčné projevy poškození). Cílem projektu je určit jakým způsobem ovlivňuje radiační poškození reparačních proteinů rychlost a správnost reparačních mechanismů v buňkách.

Ozařování biologických vzorků na urychlovačích v ÚJF v Řeži, cyklotron U120M a tandetron, je specifické díky energiím dostupných nabitých částic. Maximální energie protonů na cyklotronu U120M je přibližně 34 MeV, na tandetronu 6 MeV. Dosah těchto iontů ve vodě je pouze několik desítek μm až mm (protony 6 MeV mají ve vodě dosah přibližně 0,5 mm, 34 MeV 11 mm), proto je třeba pracovat s tenkými vrstvičkami vzorků.

Bylo navrženo a testováno několik možných řešení:

a) Prototypové plastové nebo kovové kroužky držící velmi tenkou Mylar folii vyrobené v ODZ ÚJF
b) Sterilní Petriho misky s kruhovým otvorem ve dně, na které je nalepeno krycí mikroskopické sklíčko
c) Komerčně dostupné plastové misky, u kterých je dno a případně i víčko nahrazeno Mylar folií (firma Chemplex, USA).

Navržená řešení byly testovány během ozařování na cyklotronu U120M. Pro další experimenty s neonatálními dermálními fibroblasty se jeví jako nejvhodnější řešení varianta c. Pro experimenty realizované ve spolupráci s kolegy z Biofyzikálního ústavu AV ČR v Brně, kdy byly buňky analyzovány metodou FISH (fluorescenční in situ hybridizace) se jeví výhodnější uspořádání v Petriho miskách (varianta b). Buňky rostou přímo na mikroskopickém sklíčku, po ozáření jsou dále zpracovány a analyzovány fluorescenčním mikroskopem. DNA ve vodných roztocích jsou ozařovány v úzkých plastových mikrozkumavkách.

Podíl přímého a nepřímého účinku ve stopách protonů byl studován s použitím DNA plasmidů pBR322 ve vodných roztocích. Vzorky obsahovaly různé koncentrace sloučenin vychytávající hydroxylové radikály (kumarin-3-karboxylová kyselina, dimethylsulfoxid nebo glycylglycin). Metodou agarózové elektroforézy byly stanoveny výtěžky jednoduchých a dvojných zlomů DNA. V závislosti na koncentraci vychytávače lze odhadnout podíl přímého poškození DNA a příspěvek nepřímého poškození prostřednictvím OH radikálů. Tyto informace budou velmi zajímavým výstupem projektu, zvláště pokud získáme větší rozsah různých iontů a energií.

Radiační poškození proteinů bylo studováno u restrikčních enzymů HindIII a PvuII. Enzymy ozářené rostoucími dávkami záření byly inkubovány s pCDNA3 plasmidy a vzorky byly poté analyzovány metodou agarózové elektroforézy. Funkční enzymy rozpoznávají specifickou sekvenci bazí a v tomto místě DNA štěpí. Proteiny poškozené zářením postupně ztrácejí schopnost rozpoznat a štěpit DNA. Bylo sledováno snižování aktivity enzymů s rostoucí dávkou záření.

V prvním roce řešení projektu nebylo plánováno získání výsledků pro buněčné kultury. V rámci přípravy byly nicméně připraveny metodiky pro realizaci experimentů, potřebné laboratorní uspořádání a byly realizovány první pilotní experimenty. Křivky přežití byly měřeny pro konfluentní neonatální fibroblasty pěstované na 2,5 μm Mylar foliích a ozářených rostoucími dávkami gama záření a 15 a 30MeV protonů. V ozářených vzorcích bylo stanoveno přežití buněk a četnost výskytu mikrojader. Experimenty budou zopakovány, doplněny a analyzovány. Ve spolupráci s Biofyzikálním ústavem AV ČR, v.v.i. proběhly i první experimenty zaměřené na reparaci DSB v neonatálních fibroblastech v závislosti na struktuře chromatinu v buněčném jádru.

# Test of the neutron depth profiling chamber and readout electronics

Neutron Physics Laboratory - Nuclear analytical methods with neutrons

Egor Vezhlev

Proposal ID

277

**Report regarding proposal #277 "Test of the neutron depth profiling chamber and readout electronics"**

E. Vezhlev[1], A. Ioffe[1], V. Ossovyi[1], I. Tomandl[2] and J. Vacik[2]

[1] Jülich Centre for Neutron Science (JCNS) at Heinz Maier-Leibnitz Zentrum (MLZ), Forschungszentrum Jülich GmbH, 85748 Garching, Germany

[2] Nuclear Physics Institute, 25068 Rez, Czech Republic

The main aim of the proposed experiment was a test of the newly designed and built at JCNS NDP chamber. The idea was to benchmark the performance of the vacuum chamber and readout analog electronics (spectroscopic chain). 5 days of the beamtime were used for installation and alignment of the chamber, adjusting the setup to minimize the electronic noise and background contributions and measurements with standard NDP samples: SRM 2137 (Boron implant in Silicon), SRM93a (Borosilicate glass), LiB standard NDP sample provided by the instrument scientist. JCNS NDP chamber was installed at T-NDP beamline right after the main vacuum chamber of the instrument. It was connected to the onsite oil-free vacuum pump via plastic flange for insulation from electronic noise. Spectroscopic chain was housed in a standalone compact NIM crate, than the digitized signal went to MCA module connected to the PC, where the spectrum was recorded.

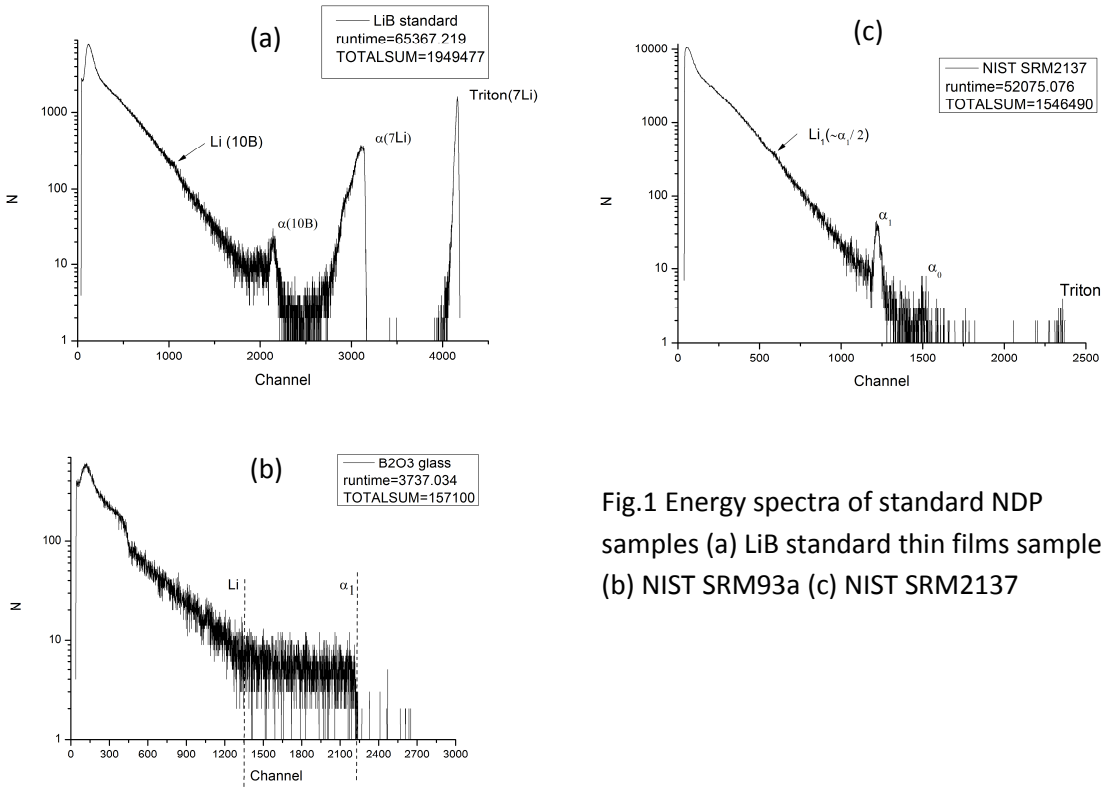


Fig.1 Energy spectra of standard NDP samples (a) LiB standard thin films sample (b) NIST SRM93a (c) NIST SRM2137

Experiment showed predictable results for the set of samples. The noise tail (preferably coming from background) was relatively high in comparison with steadily operating NDP setup at the beamline but the main energy peaks were still distinguishable.

# Cross-section measurements of the 16O(n,tot) reaction in the neutron energy range 20-35 MeV

Laboratory of Cyclotron and Fast Neutron Generators

Mitja Majerle

Proposal ID

279

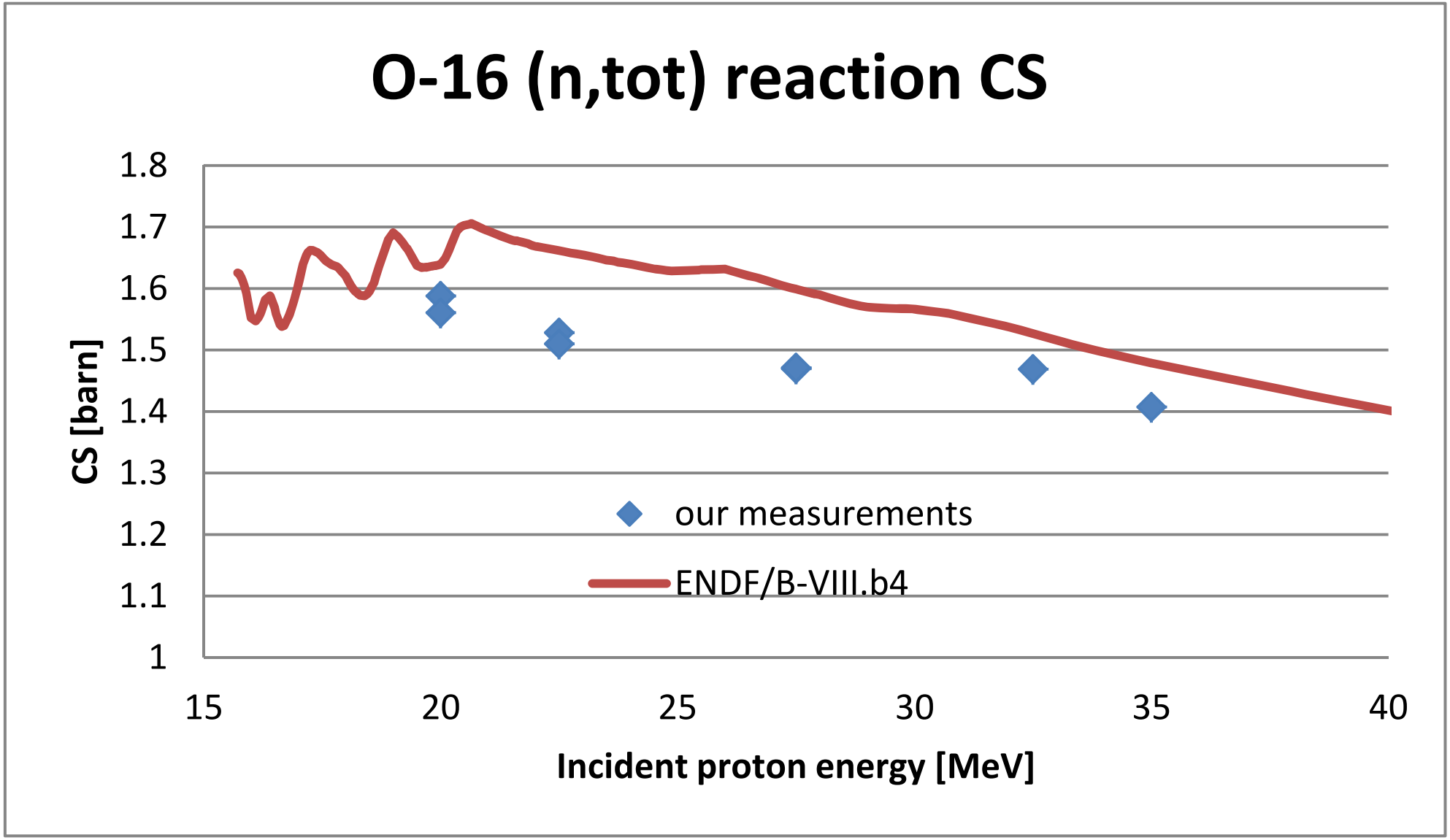
O-16 (n,tot) reaction CS
CS [barn]
1.8
1.7
1.6
1.5
1.4
1.3
1.2
1.1
1
15
20
25
30
35
40
Incident proton energy [MeV]
our measurements
ENDF/B-VIII.b4

# Bright fluorescent nanodiamonds with controlled shape

Laboratory of Cyclotron and Fast Neutron Generators

Petr Cígler

Proposal ID

152

**Report regarding project "Bright fluorescent nanodiamonds with controlled shape"**

Proposer: Petr Cígler, Institute of Organic Chemistry and Biochemistry of the CAS
Registered co-proposer: Jan Štursa, Institute of Nuclear Physics of the CAS

In this project we focused on shaping of nanodiamond (ND) particles to become pseudospherical and on generation of fluorescence defects in these NDs. First, the NDs were chemically processed to round their crystalline interface. We used molten potassium nitrate which caused a controllable etching of crystal edges and vertexes. Using this material, we performed the irradiation experiments in cyclotron to generate vacancies according to the planed scheme, including control particles without etched surface. The resulting irradiated NDs were annealed to generate fluorescent NV centers. In this way we successfully produced both pseudospheric and angular fluorescent NDs. We evaluated their spectral properties and characterized them with various physico-chemical methods (such as zeta potential measurements, dynamic light scattering, transmission electron microscopy, Raman spectroscopy). Using the prepared fluorescent NDs we have performed 7 studies [1-7] which all have been published in high impact journals. We also wrote one chapter for *Methods in Pharmacology and Toxicology* series. Another manuscript has been recently submitted.

**References dedicated to the project:**

1) Petrakova V., Rehor I., Stursa J., Ledvina M., Nesladek M., Cigler P.: Charge-sensitive fluorescent nanosensors created from nanodiamonds. *Nanoscale*, **2015**, *7*, 12307-12311.
2) Slegerova J., Hajek M., Rehor I., Sedlak F., Stursa J., Hruby M. and Cigler P. Designing the nanobiointerface of fluorescent nanodiamonds: highly selective targeting of glioma cancer cells. *Nanoscale*, **2015**, *7*, 415-420.
3) Havlik J., Raabova H., Gulka M., Petrakova V., Krecmarova M., Masek V., Lousa P., Stursa J., Boyen H.-G., Nesladek M., Cigler P.: Benchtop Fluorination of Fluorescent Nanodiamonds on a Preparative Scale: Toward Unusually Hydrophilic Bright Particles. *Adv. Funct Mater.*, **2016**, *26*, 4134–4142.
4) Stursa J., Havlik J., Petrakova V., Gulka M., Ralis J., Zach V., Pulec Z., Stepan V., Zargaleh S. A., Ledvina M., Nesladek M., Treussart F., Cigler P.: Mass production of fluorescent nanodiamonds with a narrow emission intensity distribution. *Carbon*, **2016**, *96*, 812-818.
5) Petrakova V., Benson V., Buncek M., Fiserova A., Ledvina M., Stursa J., Cigler P. and Nesladek M.: Imaging of transfection and intracellular release of intact, non-labeled DNA using fluorescent nanodiamonds. *Nanoscale*, **2016**, *8*, 12002–12012.
6) Vavra J., Rehor I., Rendler T., Jani M., Bednar J., Baksh M. M., Zappe A., Wrachtrup J., Cigler P.: Supported lipid bilayers on fluorescent nanodiamonds: a structurally defined and versatile coating for bioapplications. *Adv. Funct. Mater.* **2018**, 1803406.
7) Havlik J., Petrakova V., Kucka J., Raabova H., Panek D., Stepan V., Zlamalova Cilova Z., Reineck P., Stursa J., Kucera J., Hruby M., Cigler P.: Extremely rapid isotropic irradiation of nanoparticles with ions generated in situ by a nuclear reaction. *Nature Comm.* **2018**, DOI: 10.1038/s41467-018-06789-8.

Book Chapter:
Neburkova J., Hajek M., Rehor I., Schimer J., Sedlak F., Stursa J., Hruby M., and Cigler P.: Targeting Glioma Cancer Cells with Fluorescent Nanodiamonds via Integrin Receptors. In *Methods in Pharmacology and Toxicology*, E. Patsenker (ed.). pp. 169-189, Humana Press, New York, NY 2018.

# Interaction of detonation nanodiamond clusters in thixotropic aqueous suspensions

Neutron Physics Laboratory - Neutron diffraction

Oleksandr Tomchuk

Proposal ID

280

**Report regarding proposal "Interaction of detonation nanodiamond clusters in thixotropic aqueous suspensions"**

**O.V. Tomchuk, M.V. Avdeev, FLNP JINR, Russia**
**A.T. Dideikin, A.E. Alexenskii, A.Ya. Vul, Ioffe Physical-Technical Institute, Russia**
**V. Ryukhtin, Nucl. Physics Inst., Rez, Czech Republic**

Detonation nanodiamond (DND) aqueous suspensions are of current interest in view of their developing technical and, especially, biomedical applications. Despite the electrostatic stabilization, there is a tendency in DND suspensions toward the aggregation. Nevertheless, DND suspensions remain stable as a whole showing a cluster-cluster interaction which can lead to rheological effects such as thixotropy. SANS study ($q_{min}$≈0.1 nm$^{-1}$) found no differences between the cases of positively and negatively stabilized DND particles, i.e. on the nanoscale two type of suspensions are absolutely identical [1]. Thus, special interest is the study of the interaction of diamond clusters on submicron-micron structural level, because this may be the cause of mentioned thixotropic effect, and VSANS experiment was required.

Neutron VSANS experiments were performed on DND suspensions with concentrations 5.05 wt.% and 2.25 wt.% using the MAUD instrument. The motivation for the experiments was to determine details of the structure and interaction in aqueous suspensions with positive charge stabilization produced by annealing detonation nanodiamonds (DND) in hydrogen atmosphere on a submicron scale to explain the macroscopic rheological properties.

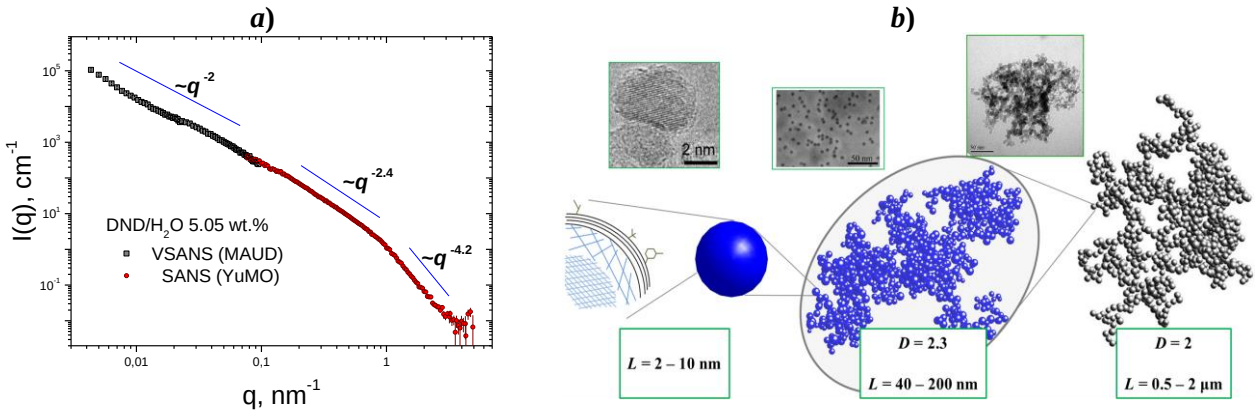


**Fig. 1.** ***a)*** Example VSANS/SANS data for DND/water system. Straight lines indicate the ranges of power-law scattering characteristic for scattering by a diffuse surface of detonation diamond nanoparticles (large *q*), the fractal structure of clusters (intermediate *q*), and the fractal structure of secondary associates (smallest *q*), respectively. ***b)*** The proposed schematic view of the multilevel structure of the aqueous suspension of detonation nanodiamonds with positive charge stabilization based on scattering data.

The investigation of the DND-water suspension on the MAUD diffractometer allowed us to detect the structural level of the secondary association of nanodiamond fractal clusters on a submicron scale, which is responsible for the rheological properties of the system, and more specifically for thixotropy. The data significantly expand the range of scattering vectors available to standard small-angle neutron instruments, and at the same time are well matched in the crossover range. Mentioned structural level is a gaussian-like fractal network connecting the primary fractal clusters of nanodiamonds. It is unstable, because it can be destroyed by a small mechanical shock (shaking), but it is restored during the day. This effect is an exceptional feature of systems with positive charge stabilization and is not observed in previously investigated systems with negative charge stabilization.

1. Avdeev M.V. et al., *Chem. Phys. Lett.* (2016) **658**, 58.

# Elemental Composition of High Entropy Alloy Sample

Neutron Physics Laboratory - Nuclear analytical methods with neutrons

Kateina Dragounová

Proposal ID

282

**Report on instrumental neutron activation analysis of HEA sample**

A flat piece of a High Entropy Alloy (HEA) of approximately rectangular shape (3 x 8 mm, ~ 1 mm thick) was available for analysis. It was broken in a clamp with its jaws covered with phenol formaldehyde resin bonded paper (FR–2 material) to avoid contamination into six pieces with masses in the range of 45 – 137 mg. To make sure that no contamination occurred, the broken pieces were shortly boiled in 0.1 M HNO3 prepared from sub-boiled HNO3 diluted with deionized water, so that about 0.5 % of the original sample mass was dissolved. The cleaned samples were washed with ethylalkohol and air dried. The samples were heat sealed into pre-cleaned polyethylene (PE) disk shaped capsules made by sealing PE foils of 0.2 mm thickness with 25 mm and 20 mm diameter for irradiation with thermal and epithermal neutrons, respectively. For quality control purposes, 75 – 100 mg aliquots of NIST standard reference material (SRM) 1633b Constituent Elements in Coal Fly Ash were prepared for irradiation as the HEA samples.

Three modes of INAA based on irradiation in the experimental reactor LVR-15 of the Research Centre Řež were used with minor modifications. Short-time irradiation for 30 s with the whole reactor neutron spectrum (S-INAA) was carried out in an irradiation channel located at the outskirts of the active core behind a beryllium reflector, in which fluence rates of thermal, epithermal and fast neutrons were 3.2×1013, 1.1×1013, and 1.1×1013 cm-2 s-1, respectively. Short-time irradiation for 45 s with epithermal and fast neutrons (S-ENAA) was carried out in the same channel. Thermal neutrons were shielded off by placing the samples into a disk shaped Cd box with 1-mm thick walls. Both short-time irradiation modes were carried out using a pneumatic facility with transport time of 3.5 s. The samples, MES calibrators, blank PE capsules and quality control samples were irradiated individually together with neutron flux monitors (5-mg disks of 0.1% Au–Al foil, IRMM, Belgium, Nuclear reference material IRMM-530a, 0.1mm thickness) to check the neutron fluence rate stability in time. Long-time irradiation for 2 h with the whole reactor neutron spectrum (L-INAA) was performed in a channel located in the Be reflector, in which fluence rates of thermal, epithermal and fast neutrons were 3.6×1013, 8.4×1012, and 8.6×1012 cm-2 s-1, respectively. In this case, the samples, MES calibrators, blank PE capsules and quality control samples were stacked together to form a column that was inserted into an aluminium irradiation can. Iron monitors (50-mg disks) were inserted between each set of 5 samples and/or calibrators to determine the axial neutron flux gradient. The sample masses for S-INAA and S-ENAA were in the range of 45 – 88 mg, those for L-INAA spanned from 116 mg to 137 mg. Gamma-ray spectrometry measurements were performed using two coaxial HPGe detectors. Both HPGe detectors were interfaced to a Canberra Genie 2000 computer controlled gamma-spectrometry analyzer through a chain of associated linear electronics, which included a Canberra 599 Loss Free Counting module to correct the variable count-rate and dead time. Canberra Genie 2000 software was used for evaluation of gamma-ray spectra.

A proxy analysis using X-ray fluorescence analysis was also carried out to assay Pb, which cannot be determined by INAA. The analysis performed at two 0.25x0.25 mm spots yielded Pb concentrations of 1.075% and 1.200 %. The results obtained may be biased ± 20 % rel., because no matrix matched calibration material was available.

Conclusion

The INAA measurement provided the required elemental composition of the tested HEA sample. Concentration of Pb amounting ca 1.1 %wt. was determined from the X-ray fluorescence analysis. The obtained INAA results were presented, together with other characterizations of the sample, at the 18th International Conference on Texture of Materials (ICOTOM-18) in St. George, Utah, USA, and the related paper submitted to IOP Journal of Physics C.

# RBS-ERDA analysis of metal / a-C:H nanocomposite films

Laboratory of Tandetron

Jan Hanuš

Proposal ID

157

Report regarding proposal "RBS-ERDA analysis of metal / a-C:H nanocomposite films"

J. Hanuš, O. Kylián, A. Shukurov, H. Biederman, Charles University in Prague, Czech Republic

A. Macková, Nucl. Physics Inst., Rez, Czech Republic

Metal / hard plasma polymer nanocomposite films are widely used in many applications as a gas barrier films or protective coatings. If copper is selected as a metal part of the nanocomposite the film benefits of its antibacterial properties and the nanocomposite coating can be used in biomedical applications as protective coating with antibacterial properties. One of the crucial parameters of the nanocomposite coatings is a proper estimation of the metal content in the film and, in case of hard amorphous hydrocarbon films (a-C:H), also estimation of the hydrogen content. Hydrogen concentration cannot be measured by the XPS and metal concentration measured by this technique is often underestimated due to the extreme surface sensitivity of the analysis. Combination of RBS and ERDA was used for proper elemental composition analysis of the whole volume of the nanocomposite coatings.

Samples with different Cu concentration were prepared by combination of PECVD process and Cu nanoparticles deposition by means of Gas Aggregation Source. It was shown that RBS, ERDA gives about ten times higher Cu concentration compared to the XPS (tab. 1). ERDA analysis showed that hydrogen content in the a-C:H matrix is about 30 at% which is a value typical for such type of hard polymeric films. The thickness of the coating is during depth profiling by RBS , ERDA normally calculated from known density of the film. In this case the calculation was done vice-versa, i.e. from the known thickness of the film (measured by spectroscopic ellipsometry) was calculated the density of the film (denoted in tab. 1 as 'measured') . Those results were compared with the theoretically calculated film density from known elemental composition (denoted in tab. 1 as 'theoretical'). Significant difference between those two densities, especially in case of high Cu content, indicates porosity of the coating. The presented results were published in Plasma Processes and Polymers:

Jan Hanuš,* Tereza Steinhartová, Ondřej Kylián, Jaroslav Kousal, Petr Malinský, Andrei Choukourov, Anna Macková, Hynek Biederman, Deposition of Cu/a-C:H Nanocomposite Films, Plasma Proc. And Pol. DOI: 10.1002/ppap.201500208

*Table 1.* Elemental composition measured by XPS and RBS, ERDA as a function of DC magnetron current. In the last three columns are the thickness of the coating measured by ellipsometry (in nm), the density calculated from the known thickness by RBS, ERDA and the density theoretically calculated from the elemental composition obtained by RBS, ERDA methods, both in $g \cdot cm^{-3}$.

| | XPS [at.%] | | | RBS, ERDA [at.%] | | | | | Density [$g \cdot cm^{-3}$] | |
|---|---|---|---|---|---|---|---|---|---|---|
| DC magnetron current [mA] | C | O | Cu | C | O | Cu | H | Thickness [nm] | Measured | Theoretical |
| 50 | 93.8 | 6.2 | 0.0 | 66.1 | 6.4 | 0.0 | 27.5 | 92 | 1.9 | 1.9 |
| 75 | 93.7 | 6.3 | 0.0 | 66.3 | 6.7 | 0.2 | 26.7 | 93 | 1.9 | 1.9 |
| 100 | 91.1 | 8.5 | 0.4 | 62.2 | 8.8 | 5.2 | 23.8 | 121 | 2.0 | 2.4 |
| 150 | 90.1 | 9.3 | 0.7 | 54.0 | 9.6 | 6.2 | 30.1 | 134 | 2.1 | 2.5 |
| 200 | 90.2 | 9.0 | 0.8 | 47.3 | 9.6 | 10.1 | 33.0 | 140 | 2.2 | 2.8 |
| 300 | 88.4 | 10.2 | 1.4 | 48.3 | 10.5 | 12.3 | 28.8 | 203 | 2.3 | 3.1 |

# NDP method to detect the existence of LiTaO3 in Ta2O5/LiTaO3 dual layers

Neutron Physics Laboratory - Nuclear analytical methods with neutrons

Chunguang Chen

Proposal ID

285

# Report regarding proposal "NDP method to detect the existence of $LiTaO_3$ in $Ta_2O_5/LiTaO_3$ dual layers"

Chunguang Chen[1, 2*], Ivo Tomandl[3], Jiří Vacík[3], R.-A. Eichel[2], P. H. L. Notten[1, 2]
[1]Department of Chemistry and Chemical Engineering, Eindhoven University of Technology,
P.O. Box 513, 5600 MB Eindhoven, The Netherlands
[2]Institut für Energie und Klimaforschung (IEK-9), Forschungszentrum Jülich,
D-52425, Jülich, Germany
[3]Nuclear Physics Institute, Academy of Sciences of the Czech Republic,
CZ-25800, Rez Near Prague, Czech Republic
Corresponding:c.chen@tue.nl

As proposed, the $Ta_2O_5$ thin films were deposited as anode materials by of metal-organic chemical vapor deposition (MOCVD) at 425 ℃for building all-solid-state Li-ions batteries. However, bare the storage capacity of the bare $Ta_2O_5$ anode decays rapidly during long cycling (charging/discharing). The capacity deterioration results from the large volumetric changes induced by the (de)lithiation process and the continuous loss and regeneration of the solid electrolyte interface (SEI). To mitigate this, $LiTaO_3$ films are introduced as the artificial SEI to isolate the $Ta_2O_5$ anode from direct contact with the liquid electrolyte and improved electrochemical performance was demonstrated. Nevertheless, in our SEM observations of the $Ta_2O_5/LiTaO_3$ dual layers (as shown in Figure 1), it is difficult to distinguish the interface between $Ta_2O_5$ and $LiTaO_3$. This is mainly due to the fact that the $Ta_2O_5$ and $LiTaO_3$ thin films deposited at 425 ℃ are all amorphous.

To approve the Li-existence in $LiTao_3$ layers, Neutron depth profiling (NDP) method was applied. Successfully, Li element information were found in $LiTaO_3$ layers, as indicated in Figure 2. Interestingly, the depth information of LiTaO3 in $Ta_2O_5/LiTaO_3$ deviated from the real thickness a bit. This can be explained by the Li movement into $Ta_2O_5$ layers during high temperature (425 ℃) deposition. To demonstrate the Li dynamics, further experiments may be necessary, like X-ray photoelectron spectroscopy (XPS) to check the valence details in different XPS sputtering depth.

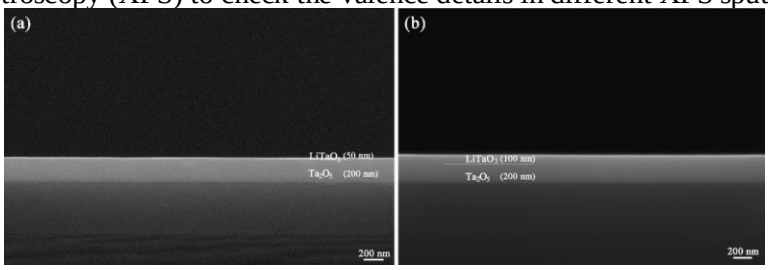


Figure 1. SEM images of the $LiTaO_3$ (50nm (a) and 100nm (b)) coated $Ta_2O_5$ electrodes.

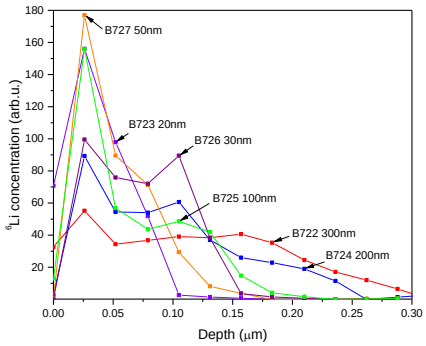


Figure 2. Li depth information in the deposited $Ta_2O_5/LiTaO_3$ dual layers.

**Acknowledgements:** The authors would like to express their thanks to the support from CANAM infrastructure of NPI ASCR Rez.

# Structural modifications of metallic glasses by neutron irradiation

Laboratory of Cyclotron and Fast Neutron Generators

Marcel Miglierini

Proposal ID

286

**Report regarding the experiment ID-286 "Structural modifications of metallic glasses by neutron irradiation"**

Marcel Miglierini, Milan Štefánik and Martin Cesnek

Samples of Fe-based metallic glasses were prepared in a form of ribbons about 1-6 mm wide and about 23 microns thick. The following compositions were produced: $Fe_{76}Mo_8Cu_1B_{15}$, $Fe_{79}Mo_8Cu_1B_{12}$, $Fe_{79}Nb_7Cu_1B_{13}$, and $Fe_{78}Si_9B_{13}$. They were exposed to irradiation with neutrons obtained at the fast neutron facility based on the U-120M isochronous cyclotron of the NPI CAS in Rez.

Irradiation experiments were accomplished during two runs (10.6. and 26.8.2016) to obtain higher total neutron fluences. In both experiments, the p(35)+Be accelerator-driven neutron source with broad spectrum up to 33 MeV was used. The estimated total neutron fluences of $2.7 \times 10^{16}$ n/cm$^2$ at the position of the investigated samples were obtained. After each run, gamma as well as Mössbauer spectra were acquired. The first one served as test for production of radioactive nuclides. The latter spectra were used for assessment of radiation induced effects in the amorphous samples.

As an example, Mössbauer spectra recorded before and after one irradiation cycle are shown in Fig. 1 (left). For $Fe_{78}Si_9B_{13}$ metallic glass, obvious deviations in the intensities of the second and the fifth spectral lines are clearly seen. After irradiation, intensities of these lines have increased which indicates rearrangement of magnetic moments of the resonant atoms. They tend to rotate towards the plane of the ribbon. Such repositioning is caused by internal stresses due to topological modifications of the constituent atoms. So even though the samples are amorphous, we could reveal subtle modifications via magnetic moments.

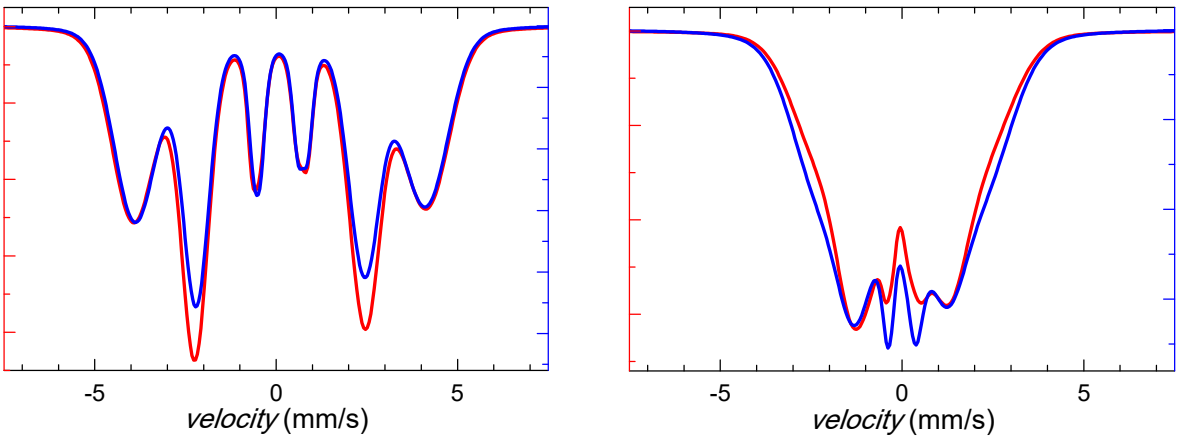


Fig. 1. Mössbauer spectra of as-quenched (blue) and neutron irradiated (red) $Fe_{78}Si_9B_{13}$ (left-hand panel) and $Fe_{79}Nb_7Cu_1B_{13}$ (right-hand panel) metallic glasses.

While the Fe-Si-B metallic glass is ferromagnetic at room temperature, another irradiated amorphous samples are only weakly magnetic. Right-hand panel of Fig. 1 exhibits the case of the $Fe_{79}Nb_7Cu_1B_{13}$ metallic glass. Here, opposite tendency of the moment rotation is observed. In addition, subtle decrease of hyperfine magnetic fields is demonstrated by narrowing of the spectral signal.

We have irradiated also samples of corrosion-resistant steel. As this material features crystalline structure, non-significant deviations were observed in the corresponding Mössbauer spectra.

# Characteritics of Pd and Fe thin films upon a rapid annealing and after modification by 1MeV Ar+ and

Laboratory of Tandetron

Hoa Kim Ngan Nhu-Tarnawska

Proposal ID

287

**Measurements/Experiments in the Laboratory of Tandetron, Nuclear Physics Institute, Academy of Sciences of the Czech Republic (CAS)**
**18-21.07.2016**
in the cooperation with Dr. Anna Mackova

*Nhu-Tarnawska Hoa Kim Ngan, Institute of Physics, Pedagogical University of Krakow, Poland.*

Our main research topic is "investigations the interface properties of nanostructures of advanced materials". We have performed similar investigations using Ion Beam Analysis (IBA) and Ion beam Modifications of Materials (IBMM) but on different materials.
In the submitted proposal in May 2016, we wrote about the measurements on Fe and Pd-based films. However, at the beginning of July 2016, just two weeks before the planning experiment time, we have managed to get several new series of thin films prepared by Molecular Beam Epitaxy (MBE) technique. Thus we decided to perform the proposed experiments on the new films, mostly on $Fe_3O_4$-based and Mn-based films.

**I/ Experiments:**
2 MeV $He^+$ ion beam for RBS, RBS-C and ERDA measurments
2MeV $Au^+$ ion beam with ion fluence of $10^{14}$ ions/$cm^2$ for film modifications
I.1 RBS measurements on the MBE films with different layer thicknesses: a) K1-K3 films ($Fe_3O_4$/Fe/MgO(001)) and b) Mn 16, Mn18, Mn25, Mn30, Mn31-32, Mn35-36 (MgO/Mn(+O)/MgO(001)),
I.2 RBS-C measurements on the K1-K3 films,
I.3 RBS and ERDA measurements on polimer/nanoparticle films on Si(111) substrates prepared by spin coating method,
I.4 IBMM performed for the K1-K3 films,
I.5 Data collection and data analysis.

**II/ Scientific outcome:**
**II.1 Presentations in the international conferences**
1/ M. Krupska, N-T.H. Kim Ngan, S. Sowa, Z. Tarnawski, L. Havela, P. Malinsky, A. Mackova
*Characterization and modification of Fe3O4 thin films*
4th International research and practice conference "Nanotechnology and Nanomaterials" (NANO-2016). August 24-27, 2016. Lviv, Ukraine. Abstract book. ISBN 978-966-8364-94-5. p. 131
2/ M. Krupska, N-T.H. Kim Ngan, S. Sowa, Z. Tarnawski, L. Havela, P. Malinsky, A. Mackova
*Ion beam mixing and interdiffusion in magnetite thin films.*
Nanomaterials: Application & Properties '2016 (NAP-2016), September 14-19, 2016. Lviv, Ukraine. Book of abstracts.
3/ M. Krupska, N-T.H. Kim Ngan, S. Sowa, Z. Tarnawski, L. Havela, A. Mackova, P. Malinsky
*Ion beam mixing in magnetite thin films.*
2nd International Conference on Magnetism and Superconductivity in Selected Systems (StoCP-2016), September 25-30, 2016, Zakopane, Poland. Book of program and abstracts, p.72.

**II.2 Publication**
1. M. Krupska, N.-T. H. Kim-Ngan, S. Sowa, Z. Tarnawski, L. Havela, P. Malinsky, A. Mackova
*Ion beam Mixing and Interdiffusion in Magnetite Thin Films*
Proceedings of the 2016 International Conference Nanomaterials: Applications and Properties (NAP2016, 14-19 September 2016, Lviv, Ukraine), vol. 5 (1) (2016) article 01PCSI11/1-3. ISSN: 2304-1862 (Print), ISSN: 2306-580X (Online). Eds. A.D. Pogrebnjak, Y.M. Shabelnyk. Publisher: Sumy State University, 2016.

**Acknowledgment**
*Two PhD students from Krakow (Magdalena Krupska and Sylwia Sowa) have participated to the experiments in Rez.*
*Measurements were carried out at the CANAM infrastructure of the NPI CAS Rez supported through MEYS project No. LM2015056.*

# NAA measurement of impurity of RBMK stack graphite

Neutron Physics Laboratory - Nuclear analytical methods with neutrons

Plukiene Rita

Proposal ID

288

# Report regarding proposal "NAA measurement of impurity of RBMK stack graphite"

**R. Plukienė, A. Plukis, E. Lagzdina, Center of Physical Sciences and Technology, Lithuania**
**J. Kucera, Nucl. Physics Inst. CAS, Rez, Czech Republic**

Several samples of RBMK graphite of different construction elements (stack column, sleeve and bushing) were analysed with instrumental neutron activation analysis (INAA) method (LVR-15 experimental reactor of the Research Centre Řež, Ltd.) in order to obtain the missing information on impurity distribution in the RBMK graphite for inter-comparison purposes with previously obtained results INAA & GDMS (Ancius et. al 2005) in graphite sleeve and for inter-calibration purposes to compare result obtained by different methods (PGAA (Z. Revay, MLZ), ICP-MS (Puzas et al., 2010).

Samples with mass of about 100 mg were analyzed in duplicates with instrumental neutron activation analysis (INAA) using both short- and long-time irradiations, 2 min. and 3 h, respectively, in the LVR-15 experimental reactor (Research Centre Řež, Ltd.), at a thermal neutron flux of $3 \cdot 10^{13}$ $cm^{-2}$ $s^{-1}$. The induced radionuclides were measured with high efficiency, high resolution coaxial HPGe detectors after several decay times to achieve detection limits of elements determined as low as possible. Altogether 45 elements were determined. The results were in agreement with the U.S. NIST certified values within uncertainty margins, thus proving the accuracy of analysis.

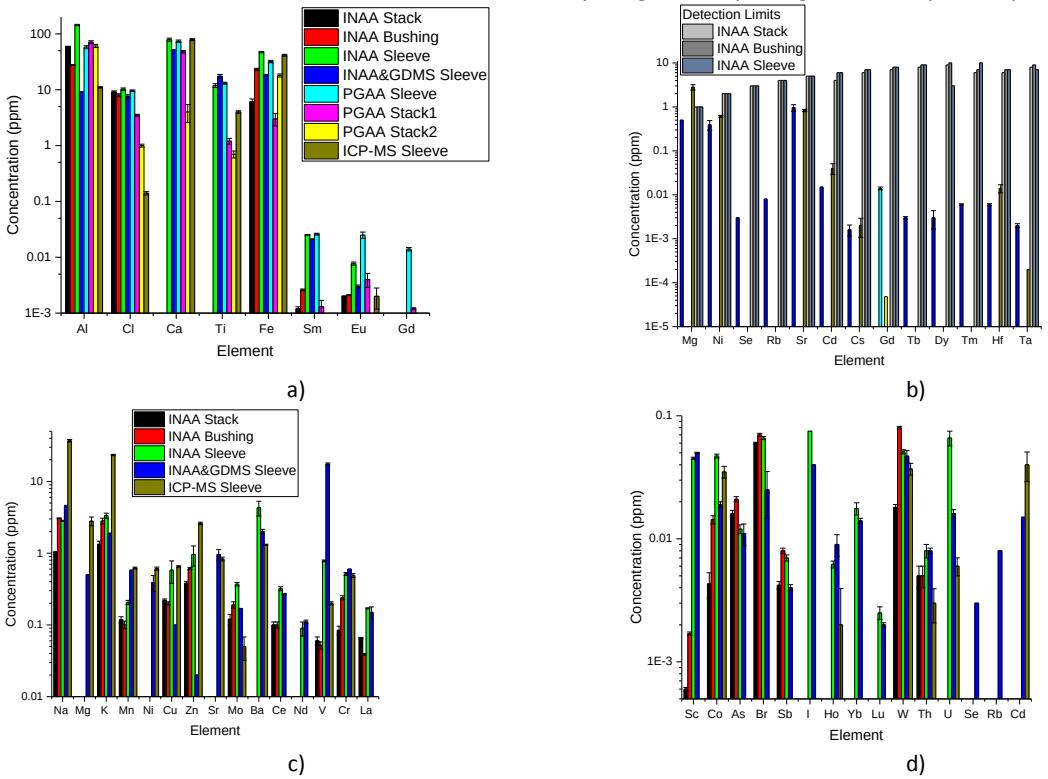


Fig. 1 (a-d) Comparison of INAA (2016), INAA&GDMS (2005), PGAA(2016) and ICP-MS (2010) measurements results on virgin RBMK-1500 graphite samples impurities.

8 elements were measured by all four methods as it is presented in Fig 1a. PGAA agrees with INAA results within uncertainty margins almost for all measured nuclides analysed Cl (in sleeve), Ca (sleeve), Ti (sleeve and stack), Fe (stack), Sm (sleeve and stack) (see Fig 1a). By PGAA method obtained Cl concentration is smaller in the stack comparing with INAA method, but it is still higher than obtained value by ICP-MS. Generally, for all measured impurities, concentrations may vary by order of magnitude comparing stack, sleeve and bushing materials. Concerning some element for which in all INAA cases (stack, bushing, sleeve) only detection limits have been estimated – the estimated impurity values by other methods are below the declared INAA detection limits as it is presented in Fig. 1b). Elements which have been measured in the graphite samples by INAA, INAA&GDMS and ICP-MS methods are presented in Fig.1 (c-d): c) for nuclides in higher concentration; d) for nuclides in lower concentration. RBMK-1500 graphite sleeve impurity values determined by INAA agrees well with INAA&GDMS results for the most of nuclides: Na, Cl, K, Ca, Sc, Ti, Cr, Mn, Ni, Cu, As, Br, Rb, Sr, Ag, Cd, Sb, I, Ba, La, Ce, Nd, Sm, Eu, Dy, Ho, Yb, Lu, Ta, W and Th. Slightly different impurity concentrations have been obtained for Mg, Al, V, Fe, Co, Zn and U. Higher disagreement in graphite impurity concentration for the graphite sleeve samples have been obtained comparing INAA and ICP-MS methods: Na (3:37 ppm); Al (144:11 ppm); Cl (10:0.14 ppm); K (3:23 ppm); Ti (12:4 ppm); Mo (0.4:0.05 ppm); Ba (4.3:1.3 ppm); U (0.066:0.006 ppm), for other impurities the obtained concentration values are comparable.

We should note, that the impurities of RBMK-1500 graphite stack and bushing samples were analysed for the first time. As it appears from the results summarised in Fig.1(a-d) - the stack is "cleaner" comparing with graphite sleeve and bushing material, moreover the similar conclusion was drawn from PGAA results comparing sleeve and stack impurities concentrations.

The obtained INAA data still have to be checked how it will influence the results of MCNP6 and SCALE6.1 model adapted for RBMK-1500 graphite activation case (Plukiene et al. 2011; Plukiene et al., 2014), but the obtained information about different impurity concentrations of some clue nuclides (Cl, Mn, Fe, Co, Ni, Cu, Zn, Sr, Cs, Ba, Eu, U), which can be detected by gamma spectrometry in the spent graphite are of great value. The work on final version of summarised RBMK-1500 graphite impurity concentrations obtained by different methods is in progress and it will be used in the final RBMK-1500 numerical model for graphite radiological characterization.

**References**

Ancius et. al., 2005, Nukleonika 50 (3), 113-120; Puzas et al., 2010, Lith. J. Phys. 50, 445–449.; Plukiene et al., 2011, Prog. in Nuc. Sc. and Tech. 2, 421-426.; Plukiene et al., 2014 Nuc. Eng. and Design 277, 95-105.

# Determination the boron distribution in the boron-doped nanocrystalline diamond layers

Neutron Physics Laboratory - Nuclear analytical methods with neutrons

Petr Ashcheulov

Proposal ID

290

# Determination of the boron distribution in the boron-doped nanocrystalline diamond layers

Petr Ashcheulov

*Institute of Physics, Academy of Sciences of the Czech Republic, v.v.i, Na Slovance 2, 182 21 Prague, Czech Republic*

Microwave plasma enhanced chemical vapour deposition system with linear antenna delivery (MW-LA-PECVD) is a novel technique for the preparation of a large area (currently 30cm$^2$) diamond coatings. MW-LA-PECVD technique allows deposition of nanocrystalline diamond (NCD) layer on a variety of substrates due to its capability of low temperature diamond growth (down to 250°C). It is possible to obtain electrically conductive NCD films by introducing a boron precursor during the growth process. However, the conductivity values of the NCD films obtained in the MW-LA-PECVD reactor are much lower compared to NCD layers obtained by classical MW PECVD technique [1,2]. This effect is partially attributed to the incorporation of boron atoms into the diamond grains within the NCD film and precipitation of boron between diamond grains. Thus, to realize a full potential of coatings obtained by the MW-LA-PECVD technique boron incorporation into the NCD films must be studied in details.

Here, we have investigated the boron concentration profile in the NCD films by the NDP technique to access the boron doping efficiency. Recently, it has been reported that the addition of $CO_2$ is crucial to suppress the concurrent formation of SiC during NCD growth process [3]. NCD layers were grown in the optimized gas mixture (boron-to-carbon ratio of 15000 ppm) of $H_2/CH_4$/TMB with added $CO_2$ gas and results were compared to layers obtained with $H_2/CH_4$/TMB gas admixture with no $CO_2$ addition (Figure 1).

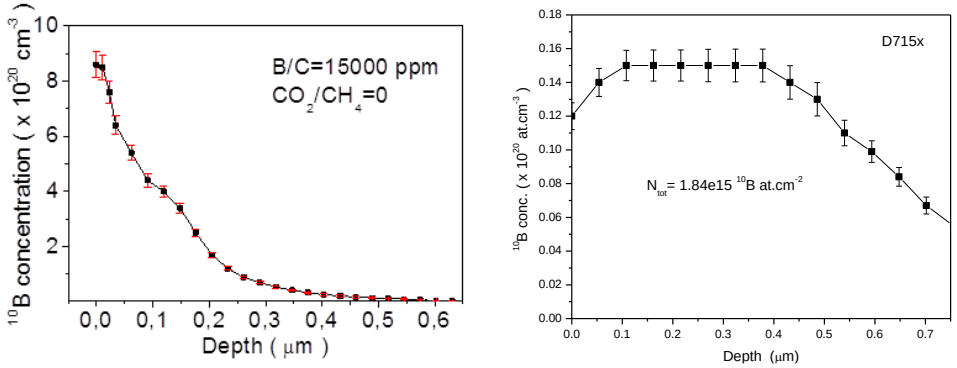


Figure 1. NDP results of samples prepared at 15000 ppm B/C ratio without $CO_2$ (left) and with $CO_2$ addition sufficient to suppress SiC formation(right)

As it seen from Figure 1, the measured boron concentration in the layers obtained without $CO_2$ addition is much higher than in the layer prepared with $CO_2$ added, ~4 × $10^{20}$ at/cm$^3$ (at 100 nm depth) and ~1.5× $10^{19}$ at/cm$^3$ (at 150 nm depth), respectively. Obtained results suggest that the incorporation of boron atoms inside the NCD film has been suppressed by the addition of $CO_2$. Therefore, further optimization of the boron-doping process parameters (CO2/CH4, B/O and B/C ratios, deposition temperature) if the MW-LA-PECVD system is necessary to tune the boron incorporation in the films ensuring the suppression of the concurrent SiC formation.

**References:**

[1] A. Taylor, L. Fekete, P. Hubík, A. Jäger, P. Janícek, V. Mortet, J. Mistrík, and J. Vacík, Diam. Relat. Mater. , 47, 27 (2014)

[2] P. Ashcheulov, J. Šebera, A. Kovalenko, V. Petrák, F. Fendrych, M. Nesládek, A. Taylor, Z. Vlčková Živcová, O. Frank, L. Kavan, M. Dračínský, P. Hubík, Jiří Vacík, I. Kraus, and I. Kratochvílová, "Conductivity of boron-doped polycrystalline diamond films: influence of specific boron defects", The European Physical Journal B, (2013) 86:443

[3] A. Taylor, P. Ashcheulov, M. Čada, L. Fekete, P. Hubík, L. Klimša, J. Olejníček, Z. Remeš, I. Jirka, P. Janíček, E. Bedel-Pereira, J. Kopeček, J. Mistrík, V. Mortet, Effect of plasma composition on nanocrystalline diamond layers deposited by a microwave linear antenna plasma-enhanced chemical vapour deposition system, phys. status solidi a 212 (2015) 2418 - 2423.

# Magnetism in mixed Fe-Mn oxyborates

Neutron Physics Laboratory - Neutron diffraction

Christine Martin

Proposal ID

292

## Magnetism in mixed Fe-Mn oxyborates

**C. Martin, CRISMAT, Caen, France**

**F. Damay, LLB-Saclay, Gif-sur-Yvette, France**

**P. Beran, Nuc. Physics Inst., Rez, Czech Republic**

Two samples belonging to the $Fe_{3-x}Mn_xBO_5$ series (x=1 and 1.5) were first studied on Meredit at RT and 10K. The new meredit-NPD data deals with two other compositions (x=0.25 and 0.75) at several temperatures. The refinement of the structures (including determination of Mn/Fe distribution) coupled with the study of magnetic behaviours (magnetic structures and evolution vs temperature) allow the establishment of a(T,x) magnetic phase diagram. As summarized in the following figures, the amount of Mn does not influence the structure itself but the iron and manganese species distribution on the cationic sub-lattice has a strong impact on the magnetism of the oxyborates. A publication is in preparation.

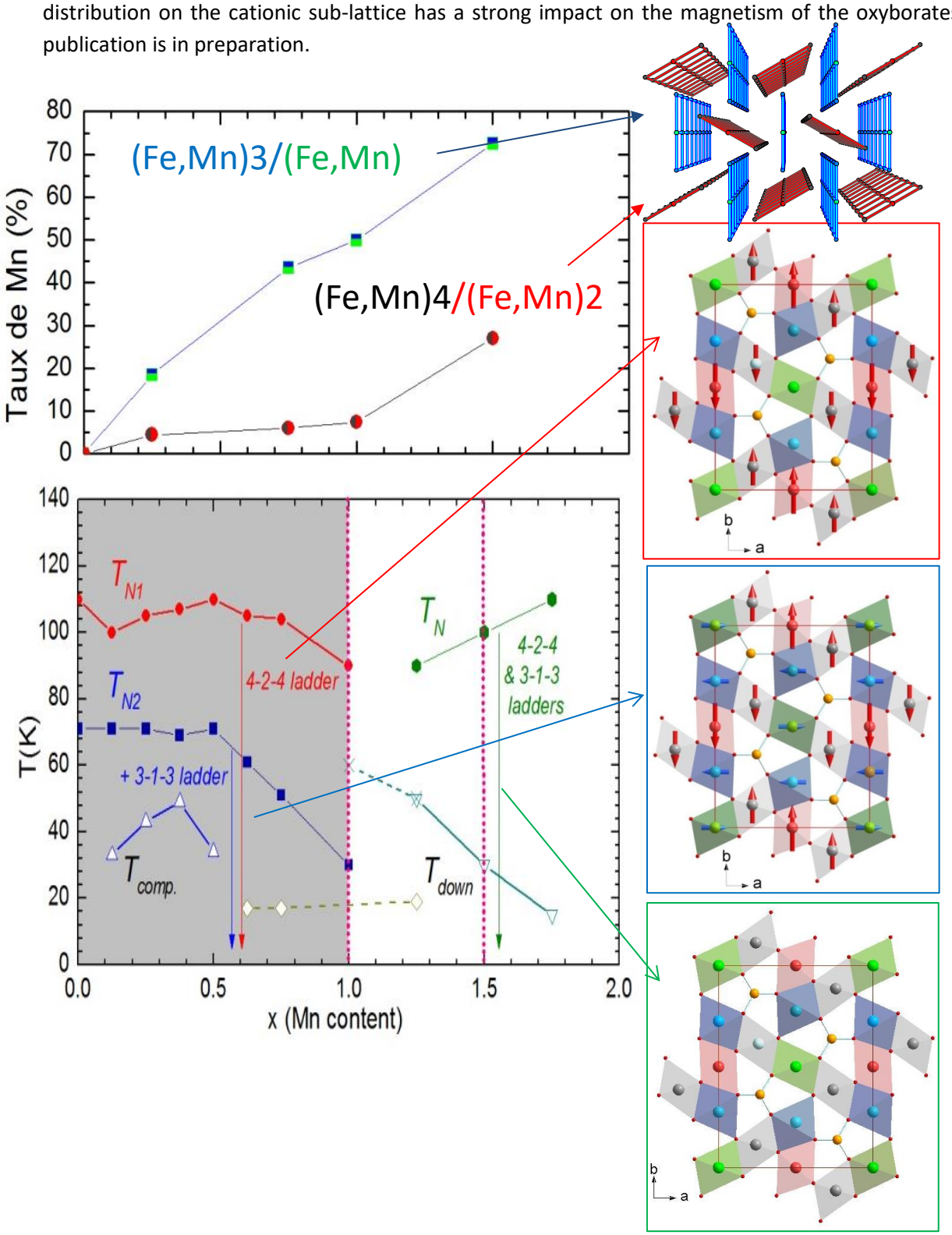

# 197(m)Hg production via the 197Au(d,2n)197Hg reaction

Laboratory of Cyclotron and Fast Neutron Generators

Martin Walther

Proposal ID

293

**Report regarding proposal "$^{197(m)}$Hg production via the $^{197}$Au(d,2n) reaction"**

M. Walther, Helmholtz-Zentrum Dresden-Rossendorf, Institute of Radiopharmaceutical Cancer Research, Germany

O. Lebeda, Nuclear Physics Institute of the CAS, Řež, Czech Republic

The significant larger cross-sections reported for $^{197}$Au(d,2n)$^{197(m)}$Hg reaction [1] compared to the proton induced $^{197}$Au(p,n)$^{197(m)}$Hg reaction could be unambiguously confirmed. With a deuteron beam energy of 16 MeV more than four times higher yields of the metastable no-carrier-added $^{197m}$Hg radionuclide were accessible using comparable beam intensity. Thus it is shown clearly that the limiting factor of the low yield proton based reaction can be overcome using this alternative nuclear reaction. The additional advantage of the higher ratio of the preferable short-lived $^{197m}$Hg radionuclide (ratio $^{197m}$Hg/$^{197}$Hg: ~1.7/1) compared to the proton accessible product (~1/1) [2] also increases the attractiveness of this production route for potential theranostic application.

**TABLE 1.** Hg and Au isotopes after proton or deuteron irradiation of gold in the target solution and product solution after separation using LN resin

| | E particle | $t_{irr}$ | $I_T$ | $m_{Au}$ | $A_{EOB}$ [MBq] in target solution | | | | $A_{EOB}$ [MBq] in product | | | | yield |
|---|---|---|---|---|---|---|---|---|---|---|---|---|---|
| No | | [min] | [µA] | [mg] | $^{197}$Hg | $^{197m}$Hg | $^{196}$Au | $^{198}$Au | $^{197}$Hg | $^{197m}$Hg | $^{196}$Au | $^{198}$Au | |
| 1 | 10 MeV p | 120 | 25 | 185 | 81 | 89 | 0.004 | 0.099 | 75 | 83 | <0.001 | <0.001 | 93% |
| 2 | 12 MeV p | 145 | 20 | 186 | 145 | 160 | 0.021 | 0.184 | 136 | 150 | <0.001 | 0.002 | 94% |
| 3 | 16 MeV d | 120 | 11 | 186 | 272 | 462 | 7 | 156 | 248 | 420 | <0.003 | <0.003 | 91% |
| 4 | 16 MeV d | 150 | 10 | 186 | 332 | 574 | 9 | 193 | 315 | 545 | <0.006 | <0.003 | 95% |

Beside the higher product yield during deuteron irradiation, also the significant formation of gold isotopes as undesired side products must be considered in the workup procedure. Therefore, according to the high requirements, a new resin based Hg/Au separation method was developed. So called LN resin (LaNthanides)[3,4], was successfully tested for this application. The obtained promising results in radionuclide production together with results of labeling - and biological experiments will be published as soon as possible in the current year in peer-reviewed international journals.

## References

[1] F. Tárkányi, F. Ditrói, A. Hermanne, S. Takács, B. Király, H. Yamazaki, M. Baba, A. Mohammadi, A.V. Ignatyuk, Nucl. Instrum. Methods Phys. Res., Sect. B 269, pp. 1389–1400, 2011.

[2] M. Walther, S. Preusche, S. Bartel, G. Wunderlich, R. Freudenberg, J. Steinbach, H.-J. Pietzsch: Appl. Radiat. Isot. 97, pp. 177–181, 2015

[3] E. P. Horwitz, C. A. Bloomquist, Journal of Inorganic Nuclear Chemistry, 37, pp. 425–434 1975.

[4] D. McAlister, E. P. Horwitz, Solvent Extraction and Ion Exchange, 25, (6), pp. 757–769 2007.

# INTERNAL: RBS analysis of rough samples

Laboratory of Tandetron

Petr Malinsky

Proposal ID

166

## Report regarding proposal “RBS analysis of rough samples”

Petr Malinský, Jakub Siegel, Vladimir Hnatowicz, Anna Macková, Václav Švorčík

The proposal was devoted to the study of surface roughness implementation to the analysis of Rutherford Backscattering Spectroscopy (RBS) energy spectra. The surface roughness of analysed samples deteriorates the RBS spectra and can make their interpretation more difficult, ambiguous and in some cases non-evaluable.

A code for the simulation of common RBS spectra implementing surface roughness effects has been written and the feasibility of the code has been demonstrated on real samples with regular roughness, which was determined by AFM method. The spectra, simulated for different ion beam incidence angles, were compared to the experimental ones measured with 2.0 MeV $He^+$ ions in the Tandetron CANAM laboratory of NPI of ASCR, v.v.i. The resulting RBS spectrum was calculated as a sum of the many particular spectra obtained for randomly chosen particle trajectories over sample 3D landscape. The used samples were prepared by the sputtering of a 35-nm-thick gold layer on the surface of the periodically patterned PET substrate.

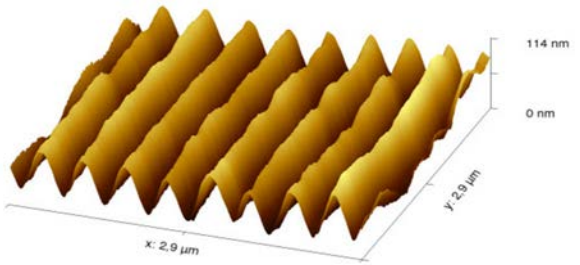


**Figure:** The visualization of the rough surface AFM data that was used as an input for the RBS spectra simulation. The sample was prepared using iradiation by laser beam with an incoming angle 22.5° and subsequently covered by Au.

The RBS spectra measured at glancing angles exhibited a more complex gold signal comprising the main peak and low-energy components corresponding to ion scattering from gold layers on the neighbouring ripples. The relative intensity of the low-energy components was an increasing function of the ion-beam incidence angle. For lower ion beam incident angles the measured gold signal was well reproduced by computer simulation but for larger incident angles the evolution of the gold signal was reproduced just qualitatively. Therefore, the effects of varying gold layer thickness and gold layer inhomogeneity on simulated spectra were examined and it was shown that the simulation with assumption of linearly varying gold layer thickness reproduced the experimental RBS spectra fairly. The next result of the experiment was that required simulated spectrum can be obtained already after summing of about 300 randomly generated particular spectra. Finally we can say that the data of surface roughness obtained from AFM analysis can be used for the simulation of RBS spectra and that the RBS measurements accomplished at glancing angle may indicate the presence of a periodic structure on the sample surface.

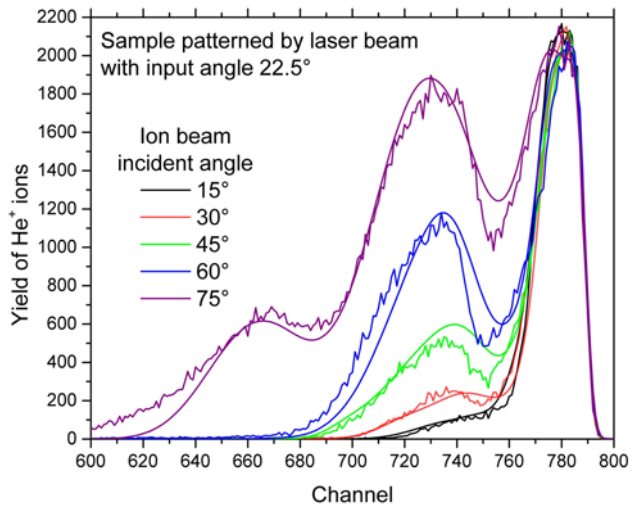


**Figure:** The resulting simulated and experimental spectra of the sample from left Fig. The RBS spectra simulation were perfomed with assumption of linearly changed gold layer thickness between top (20 nm) and bottom (75 nm) of the ripple patterns.

### References

[1] P. Malinský, V. Hnatowicz, A. Macková, Nucl. Instrum. Meth. B 371 (2016) 101-105

[2] M. Mayer, P. Malinský, F. Schiettekatte, Z. Zolnai, Nucl. Instrum. Meth. B 385 (2016) 65-73

[3] P. Malinský, J. Siegel, V. Hnatowicz, A. Macková, V. Švorčík, will be published in Nucl. Instrum. Meth. B

# RBS and channeling measurements on SiO2/Si substrates implanted by high intensity laser

Laboratory of Tandetron

Mariapompea Cutroneo

Proposal ID

167

**Ta-ion implantation induced by a high-intensity laser for plasma diagnostics and target preparation**

M. Cutroneo[1*], P. Malinsky[1,2], A. Mackova[1,2], J. Matousek[2], L. Torrisi[3], P. Slepicka[4], J. Ullschmied[5]

A virgin flat target of Ta has been fixed in the centre of the interaction chamber; $SiO_2$/Si substrates, were placed around the laser-irradiated target. A high density laser deliver its energy onto primary target and in this configuration, ions are created and accelerated by the plasma at the front surface directly illuminated by the laser. The concentration-depth profiles of the implanted Ta ions as well as the integral amount of the implanted species in $SiO_2$/Si substrates were characterised by RBS at the Tandetron Laboratory(NPI), Rez, in the Czech Republic. The depth profiles of the ion-implanted species in Si substrates with different thickness values of the $SiO_2$ layer (42 mm, 148 nm, 281 nm) are determined by RBS analysis as reported in the examples in Figure 3.

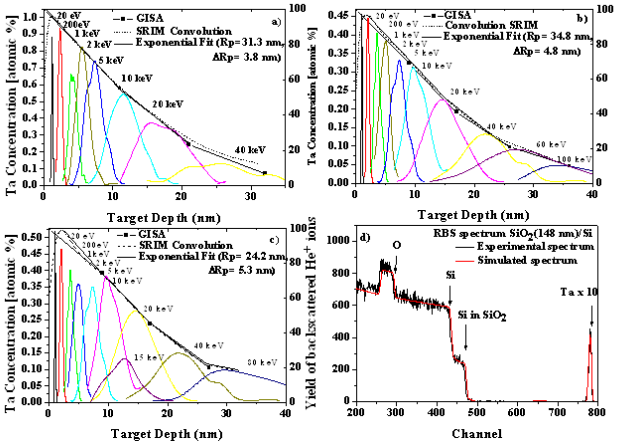


**Figure 3:** A comparison between the experimental depth-profile concentrations of the implanted Ta ions, the simulations of multi-energy Ta-ion implantation using SRIM and the convolution of the simulated multi-energy distributions for implanted ions into the substrate for $Ta^+$ in $SiO_2$(42 nm)/Si (a), $SiO_2$(148 nm)/Si (b), $SiO_2$(281 nm)/Si (c) and RBS spectrum ( Ta peak was magnified 10 times to make it more visible) from which we deduced the depth profile $SiO_2$(148 nm)/Si (d).

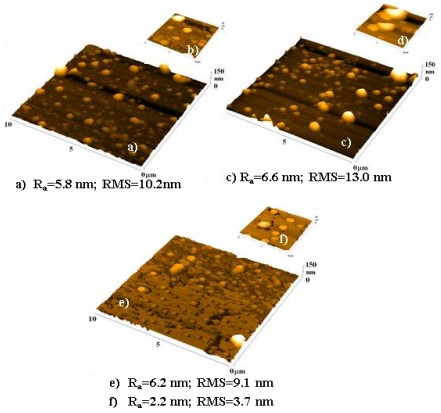


**Figure 4:** The AFM images of $SiO_2$(42 nm)/Si – (a) and insert (b), $SiO_2$(148 nm)/Si – (c) and insert (d), $SiO_2$(281 nm)/Si – (e) and insert (f) implanted at an atomic concentration of 1.05, 0.47 and 0.53 at. %, respectively, according to RBS measurements.

To characterise the changes in the substrate surface morphology, the AFM technique was used. The measurements demonstrate that the surface is covered by a Ta film containing an atomic Ta species and a granular component (Ta clusters) with nanometre-sized distribution as reported in Figure 4. The clusters distributed in the $SiO_2$ layer show 'dome' shaped embedded-like Ta structures, which should indicate that not only ions but also energetic Ta clusters are implanted. On the surface of the first substrate in Figure 4a, implanted at low energy, there are blisters and craters, whereas the substrates implanted at a high energy show only blisters. In the present paper, an innovative technique used for the deposition of the nanometallic structure in the Si-material is investigated. Such particles can be useful due to the modification of Si and $SiO_2$ properties and the creation of Si-nanocrystals for further optical and electrical application. The obtained results are of peculiar importance for many reasons: – it is useful to have offline information on the plasma produced by the laser ablation of the Ta target; the results help to understand and control the physical properties of metallic nanoparticles embedded in $SiO_2$ for the production of ultrafast optical circuits and semiconductor devices that are the future of new-generation optical communications and networks.

[1] M. Cutroneo, P. Malinsky, A. Mackova, J. Matousek, L. Torrisi, P. Slepicka, J. Ullschmied, *Nuclear Instruments and Methods in Physics Research Section B: Beam Interactions with Materials and Atoms,* 365, Part A, 15 December 2015, Pages 384–388

[2] M. Cutroneo, A. Mackova, P. Malinsky, J. Matousek, L. Torrisi, J. Ullschmied, *Nuclear Instruments and Methods in Physics Research B* 354 (2015) 56–59

# Radiation hardness investigation of APD for PSD detector readout at CBM

Laboratory of Cyclotron and Fast Neutron Generators

Vasily Mikhaylov

Proposal ID

169

# Report regarding proposal "Radiation hardness investigation of APD for PSD detector readout at CBM"

**V. Mikhaylov, V. Kushpil, O. Svoboda, A. Kugler, Nucl. Physics Inst., Rez, Czech Republic**

Radiation hardness is a key requirement for the Avalanche PhotoDiodes (APDs) for the future FAIR CBM Projectile Spectator Detector (PSD). APDs will be used for the light readout from the detector scintillators. APDs will be located at the end of the PSD and are required to withstand the total neutron fluence up to 3E12 n/cm2 for the one year of the experiment operation according to FLUKA simulation.

During the proposed experiments we have studied the behavior of APDs produced by Hamamatsu, Ketek, Sensl and Zecotek after the irradiation. On figure 1 one can see example of huge increase in dark currents after the irradiation for Ketek PM-3350 and Hamamatsu S12572-010P APDs [1]. It imposes the requirement for the APDs electronics to be able to supply currents up to 1mA.

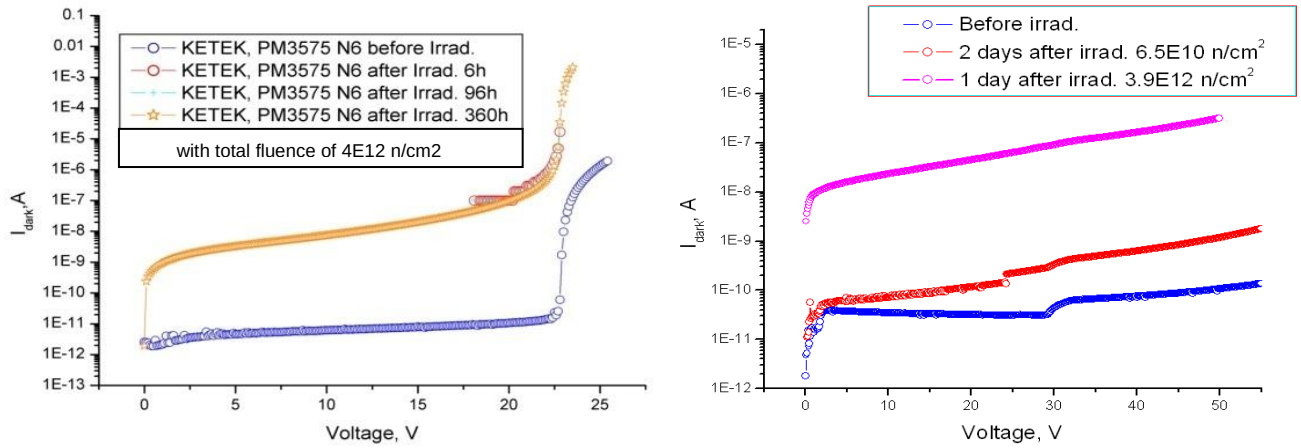


Fig. 1. Dependences of dark current on the reverse voltage for various APDs before and after irradiation with total neutron fluence indicated. Left: Ketek, right: Hamamatsu.

Using developed dedicated setup in our lab, we also studied the internal characteristics of the APDs. With help of Capacitance-Voltage profiling we have analyzed the profile of impurities produced in the APD depletion region as shown on figure 2 [2]. The achieved data is still under evaluation, in future it can be useful for development of readout electronics and improvement of detector technology.

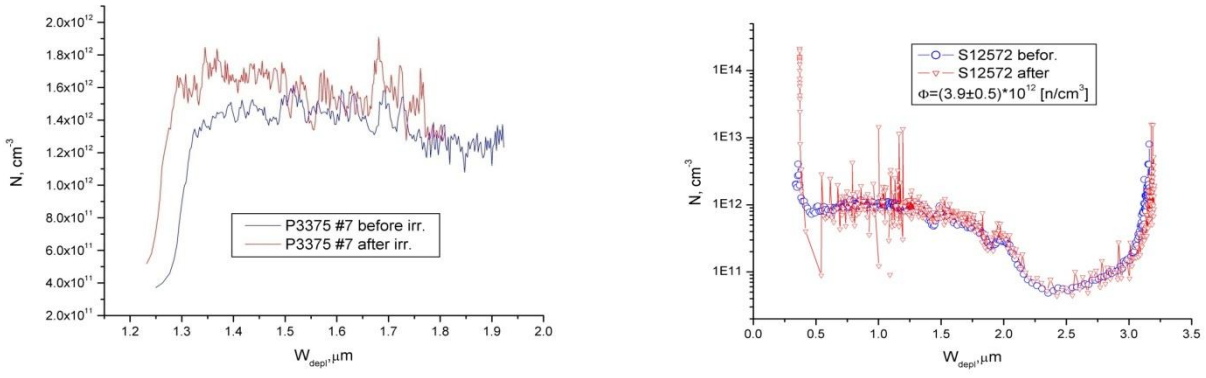


Fig. 2. Distribution of impurities produced in the depletion region on the depletion region width before and after irradiation with total neutron fluence of about 4E12 n/cm2. Left: Ketek, right: Hamamatsu.

**Own references**

1. V. Mikhaylov et al., PoS, http://pos.sissa.it/archive/conferences/234/282/EPS-HEP2015_282.pdf.
2. V. Kushpil et al., NIM A, In Press, 2016, http://dx.doi.org/10.1016/j.nima.2016.06.101.

# Interface properties of exchange-bias UO2-Fe3O4 nanostructures

Laboratory of Tandetron

Ladislav Havela

Proposal ID

170

**Report: Crystal structure of the $CaF_2$-Based $UO_2/Fe_3O_4$ thin films**

Exchange interaction through interface between a ferromagnet and an antiferromagnet may result in the magnetic exchange bias (EB) effect [1]. This property has become of a great technological value for applications in magnetic sensors based on spin-valves or tunnel junctions [2]. In this work, we studied crystal structure in bilayers of antiferromagnetic $UO_2$ (bulk Néel temperature 30.8 K) with ferrimagnetic $Fe_3O_4$, which are known to produce large exchange bias effect [3].

The samples were prepared by reactive sputter deposition from metallic targets on $CaF_2$ (100) substrates. A set of the samples with different $Fe_3O_4$ thicknesses (60-300 Å) were produced while the thickness of the $UO_2$ layer in the samples was kept constant (~300 Å). $UO_2$ was deposited at 850 K, using a partial oxygen pressure of $1.2\times10^{-6}$ mbar (Ar pressure of $6\times10^{-3}$ mbar). $Fe_3O_4$ was deposited on the top of $UO_2$ at the same partial oxygen pressure but at room temperature, in order to avoid interdiffusion. In-situ control of stoichiometry of each deposited layer was carried out using XPS (see inset in Fig. 1 for the XPS spectrum of Fe-2p in magnetite). A Mg cap was deposited for protection on top of each sample. Due to the matching lattice parameters of $UO_2$ and $CaF_2$ the films grew epitaxially in the [100] direction. The structures were further characterized by means of the Rutherford Backscattering Spectroscopy (RBS), which showed no intermixing at the interface (within the depth resolution 1 nm). Very pronounced ion channeling characteristics proved high crystallinity (low defect concentration) of the $UO_2$ layer, which is actually better than that of the (100) $CaF_2$ substrate. The spectra obtained showed well-separated signals from $UO_2$ and magnetite (Fig. 1). A channeling was observed also for the $Fe_3O_4$ layer, but considerably more defects/disorder was found, which could be perhaps related to a combined twinning [3] effect and monoclinic distortion below Verwey transition (120 K), as the samples had been subjected to thermal cycling during the prior magnetic study.

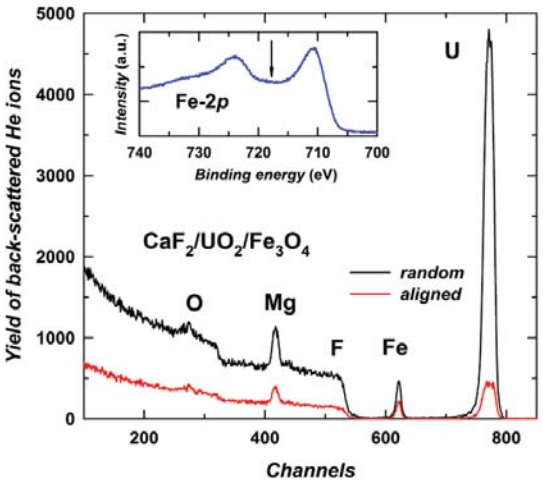


**Yield of back-scattered He ions for the incident beam along the [100] crystallographic direction of the $UO_2$ crystal (aligned) and at a random orientation (random) for the $UO_2/Fe_3O_4$ sample deposited on a $CaF_2$ substrate and capped with Mg. Inset: Fe-2*p* XPS spectrum of magnetite. Arrow indicates a position of a $Fe^{3+}$ satellite line (absent) characteristic of $\gamma$-$Fe_2O_3$.**

The samples were prepared in the framework of the EARL project of the European Commission Joint Research Centre, ITU Karlsruhe. RBS measurements were carried out at the CANAM infrastructure of the NPI ASCR Rez supported through MŠMT project No. LM2011019.

1) W. H. Meiklejohn and C. P. Bean, "New magnetic anisotropy", Phys. Rev. B, 102 1413, (1956). 2) B. Dieny et al, Phys. Rev. B, 43 1297 (1991). 3) E. A. Tereshina et al, Appl. Phys. Lett., 105 122405 (2014).

# Mesostructure of biocompatible interpenetrating composites on the base of bacterial cellulose

Neutron Physics Laboratory - Neutron diffraction

Iurii Chetverikov

Proposal ID

298

# Report for proposal №298

## Mesostructure of biocompatible interpenetrating composites on the base of bacterial cellulose

This proposal is aimed for the structural characterization of new interpenetrating polymeric networks (IPN) made on the base of nanogel films of bacterial cellulose (BC) and polyvinyltriazole (PVT) with/without Cu(II). The critical feature of composites based on BC is the presence of the structural peculiarities on different scale levels. Such peculiarities existed in human biological tissues, such as cartilages or muscle fibers and could be used for artificial producing of these materials. Ultra-small-angle neutron scattering (USANS) method can reveal the micron-scale structure of both BC and IPN on its base, that being no done before. It is essential not only for the fundamental analysis but also for the fabrication of functionalizing organic-inorganic composites on the base of BC with desired mechanical properties. The proposal is also aimed to study both the distribution of Cu(II) and the mesoscopic level of IPN. For this reason, the USANS approach will appropriate because this technique is not harmful to samples, give the possibilities to reveal structures in micro- and mesoscopic scale levels using the contrast variation by $D_2O/H_2O$ or by varying the concentration of Cu(II) dopant. As opposed to the direct measurement techniques such as SEM or AFM, USANS gives a total picture of scattering on the contrasting inhomogeneities in broad range scale, which is primarily crucial for fractal objects with complex hierarchical structure.

The USANS measurements were carried out on the double-bent-crystal SANS diffractometer MAUD in a momentum transferred Q-range of $2\cdot10^{-4} \div 2\cdot10^{-2}$ Å$^{-1}$ at Q-resolution $10^{-4} \div 10^{-3}$ Å$^{-1}$. It was investigated a series of 16 samples of IPN based on BC including PVT and Cu(II). Each sample will be measured in two positions: perpendicular or parallel to a growth surface of BC. Figure 1 shows the typical USANS dependences for composite hydrogels containing Cu(II) (scattering W4) and without copper (scattering W3).

The obtained data are under consideration. The profound analysis will allow estimating the fractal dimensions, ranges of self-similarity, sizes of aggregates, clusters, and particles forming them and will give the new information about the IPN formation processes.

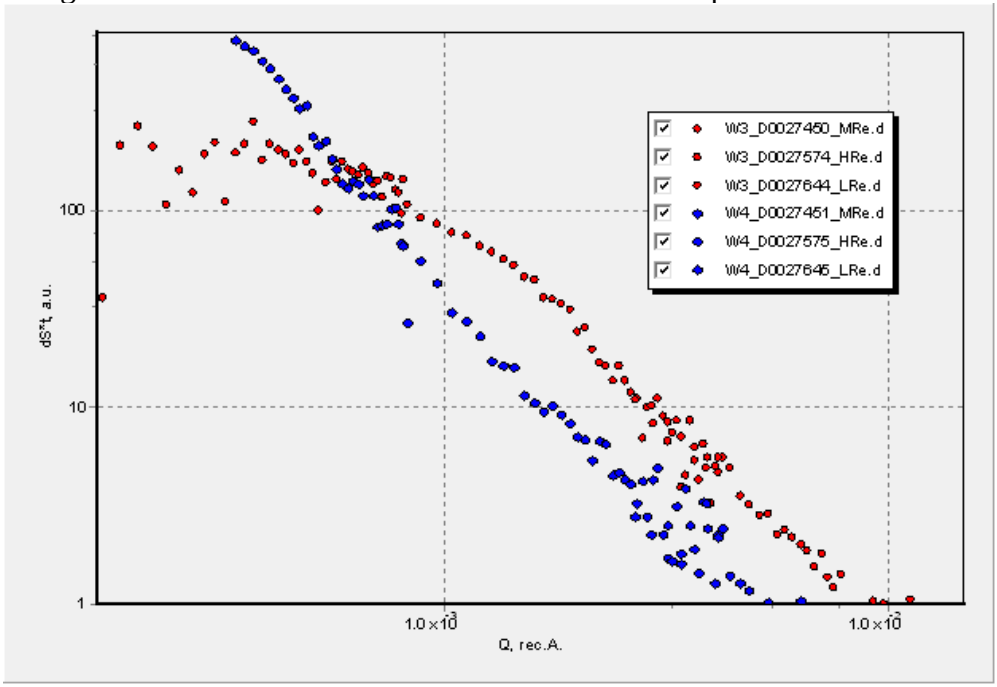


Figure 1. USANS for composite hydrogels containing 6 mass% of Cu(II) (scattering set W4—full blue symbols) and without copper (scattering set W3—full red symbols).

# Ion micro-beam to write dots in PMMA.

Laboratory of Tandetron

Mariapompea Cutroneo

Proposal ID

174

**Micro-patterns fabrication using focused proton beam lithography**

M. Cutroneo [1,*)], V. Havranek [1)], A. Mackova [1,2)], V. Semian [1)], L. Torrisi [3)] and L. Calcagno[4)]

An increasing attractiveness of top-down nanotechnology using proton beams have been gathered to the micro and nano patterning process for polymers. The particle deposited energy in matter changes by changing the type of particles according to the Bragg's law. The main advantages of lithography techniques are:

1) the depth control during the structuring by changing the ion energy,
2) the structure writing without masks,
3) good quality of the sub-surface channels, or micro-tunnels.

Energetic charged particles as MeV protons hit and penetrate into the resist as consequence of the Coulomb interaction between the incident particles with electrons and nuclei of the target. The secondary electrons induced by the primary proton beam have low energies around the ion track that generate main-chain scission in the positive resist materials (such as PMMA) or crosslinking in negative resist( such as SU-8). A high energy proton beam penetrates with the characteristic straight trajectory and deeply into polymer reducing its mean molecular weight in the irradiated area. Later, a suitable developer dissolves the irradiated area, while in the unirradiated one high density 3D micro-nano structures with sharp vertical sidewalls appear written into the resist.

The production of array of properly aligned, parallel channels as a consequence of the ion irradiation process, has been attempted in the past and the achieved results motivated our current research challenge. This paper presents ,an initial study on the production of micro-channles in the PMMA resist using fluences ranging between $3.1 \cdot 10^{13}$ ions/cm$^2$ and $3.7 \cdot 10^{14}$ ions/cm$^2$. The geometry and the angular distribution of the fabricated micro holes into PMMA was observed by the Scanning Transmission Ion Microscopy (STIM) method.

In Fig. 4 are exhibited images of the two dimensional scan indicating the shape of the holes at different depth written in the resist. The irradiation pattern was 1 μm x 1 μm, scan size 50 μm x 50 μm, of 50 mm PMMA foil irradiated at $3.7 \cdot 10^{14}$ ions/cm$^2$ (e.g. 600 nC/mm$^2$) fluence and following chemical etching. PMMA was nearly fully removed. The etching process made the holes larger (roughly 5 μm x 5 μm).

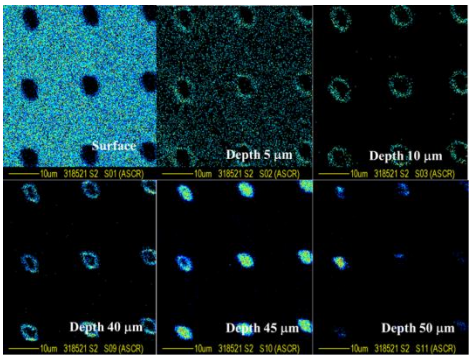


**Fig.4** STIM images for 50 μm PMMA patterned at high fluence

A correct dose, allows to deposit enough energy to create sufficient chain scissions to facilitate the resist dissolution during development. For fluences lower than $6.2 \cdot 10^{13}$ ions/cm$^2$ (100 nC/mm$^2$) the patterns were not fully exposed and PMMA was incompletely removed.

For fluences higher than $3.7 \cdot 10^{14}$ ions/cm$^2$ (600 nC/mm$^2$) start the cross linking. In Fig. 5 is reported a close-up view of the above-mentioned patterns in x 4K magnified pictures.

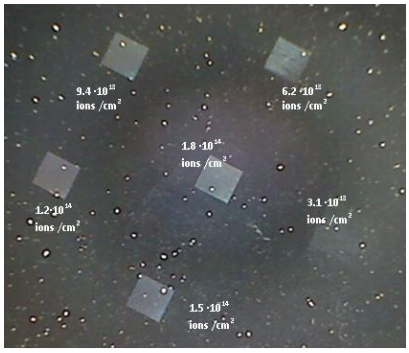


**Fig. 5** The overview optical micrograph image of the arrays consisting of 500 μm x 500 μm scan size exposed at different protons fluences.

Sharp edge and smooth sidewall nano-micro sturctures in PMMA have been realized. This research involves a great research interest due to their advanced applications such as microfluidics, optotronics, bioscience and photonics. The object of our next work will be to investigate in more depth the combination of the proton beam writing and electroplating to improve the production of metallic pillar in PMMA due to the great interest in plasmonics devices and photonics.

[1] M. Cutroneo, V. Havranek, A. Mackova, V. Semian, L. Torrisi and L. Calcagno, " Micro-patterns fabrication using focused proton beam lithography" , *Nuclear Instruments and Methods in Physics Research B* in press ( 2016).

# A structural study and ion irradiation of the silicon crystal layer

Laboratory of Tandetron

Romana Mikšová

Proposal ID

306

**Report regarding proposal "A structural study and ion irradiation of the silicon crystal layer"**

R. Mikšová, A. Macková, A. Jagerová, P. Malinský, Nucl. Physics Inst., Rez, Czech Republic
P. Slepička, V. Švorčík, Inst. Chem. Tech., Prague, Czech Republic

Our results from irradiation of Si-crystal layer on $SiO_2$/Si using 0.4 MeV $Kr^+$, $Ag^+$, $Au^+$ and 5.0 MeV $Ag^{2+}$, $Au^{2+}$ at ion fluences of $0.5\times10^{15}$–$5.0\times10^{15}$ $cm^{-2}$ show that the nuclear-energy loss is dominant for all ion species used in our experiment at the energy of 0.4 MeV and the highest is for $Au^+$ ions. This is clearly proved by RBS-C, where the completely disordered structure in the implanted layer is observed even at the lowest ion-implantation fluence used. The nuclear stopping leads to atomic displacement and the production of vacancies or large-scale defects and the subsequent amorphisation of the implanted layer as was observed in RBS-C measurement, where Si layers were completely amorphised under 0.4 MeV ion implantation performed at the ion fluence of $0.5\times10^{15}cm^{-2}$ (see Figure 1a). Since amorphisation occurs near the end of range damage. For 0.4 MeV ions the end is near Si/$SiO_2$ interface. It is shown in ref. [1] that the critical fluence for amorphisation is lower than $1.0\times10^{14}$ $cm^{-2}$ (at the room temperature), therefore lower as in our experiment.

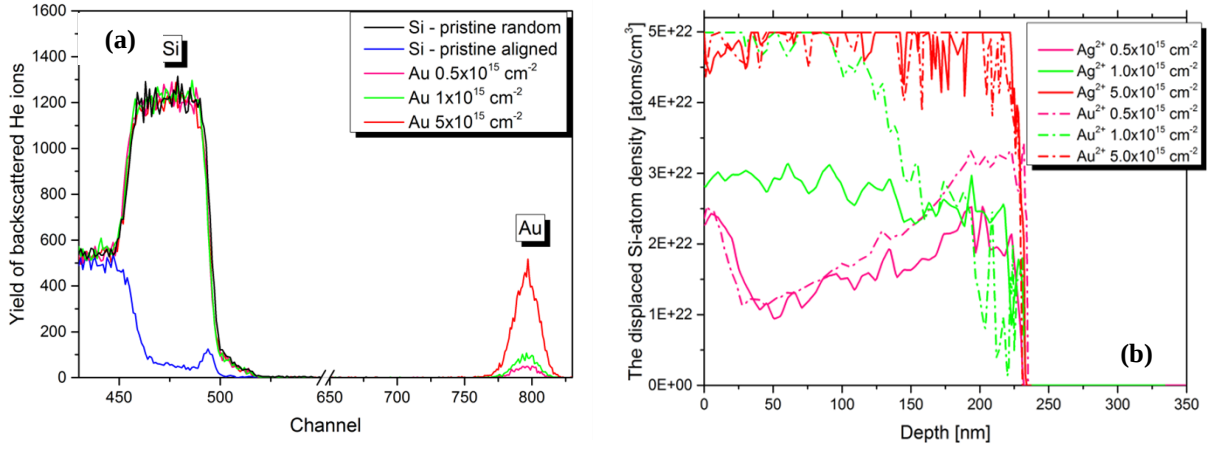


**Figure 1.** The RBS-C of random and aligned spectra of SOI irradiated by 0.4 MeV (a) and 5.0 MeV (b) $Au^+$ at ion fluencies of $0.5\times10^{15}$–$5.0\times10^{15}$ $cm^{-2}$ compared to the aligned spectrum of the virgin SOI sample. The depth profile of the displaced Si-atom density in the Si layer implanted by 5.0 MeV $Ag^+$ and $Au^+$ ions at ion fluences of $0.5\times10^{15}$–$5.0\times10^{15}$ $cm^{-2}$ (b).

In the case of the implantation of 5.0 MeV ions, the SRIM [2] code predicted more vacancies produced by $Au^+$ ions than by $Ag^+$ ions, which is in agreement with RBS-C results, exhibiting more progressive enhancement of Si-atom displacement density with increasing ion fluence for $Au^+$ ions (see Figure 1b). In the case of 5.0 MeV $Ag^+$ and $Au^+$ ions, the ratios $S_e/S_n$ were 3.23 and 1.44 and the projected range of ions is behind $SiO_2$/Si interface, in the Si bulk respectively. All these effects were also observed in RBS-C for the ion fluences above $1\times10^{15}$ $cm^{-2}$. For the lowest ion fluence used, the dynamic annealing is decreasing number of vacancies, which is not included in SRIM simulation as well as the surface damage accumulation is not predicted by SRIM. It can be concluded that 5.0-MeV ions modify the structure causing the changing of axial channels during $He^+$ ion channelling. RBS-C identified the relative number of disordered Si atoms, which was successfully used for the angular-scan simulation in FLUX code [3] for various ion-irradiation fluencies.

AFM found out that 5.0 MeV-ion implantation caused mainly surface smoothening and the average roughness is a descending function of the ion-implantation fluence. This effect can be connected to the progressive surface modification confirmed by RBS analysis, where the silicon-structure degradation may be reflected in smoothening caused by the predominant diffusion mechanism induced by ion implantation. The FTIR analysis confirmed Si crystalline layer modification mainly done by Si-Si bond rupture or modification depending on the prevailing nuclear or electronic stopping, respectively.

The results have been send for publication in Applied Surface Science and Surface Interface Analysis.

[1] L. Pelaz, L.A. Marqués, J. Barbolla, Appl. Phys. Rev. **96** (2004) 5947–5977.

[2] J. F. Ziegler et al., *SRIM: The stopping and range of ions in matter*, Version SRIM-2013. Available at: http://www.srim.org/.

[3] P.J.M. Smulders, D.O. Boerma, Nucl. Instrum. Methods Phys. Res. B 29 (1987) 471–489.

# Effect of high LET radiation on specific interaction of proteins with DNA.

Laboratory of Cyclotron and Fast Neutron Generators

Marie Davidkova

Proposal ID

52

The project “Effect of high LET radiation on specific interaction of proteins with DNA” is a contribution of our laboratory to the international COST project MP1002 "Nano-scale insights in ion beam cancer therapy (Nano-IBCT)“. The laboratory is a member of working group WG5 Radiobiological effects (detection of DNA double strand breaks, prediction and cell damage). The goal of the project is to determine how radiation damage of repair proteins influences rate and fidelity of repair mechanisms in cells. Irradiation of biological samples at accelerators of the Nuclear Physics Institute ASCR in Řež (cyclotron U120M and tandetron) is specific by low energies of incident proton beam. Maximal proton energy at cyclotron U120M is approximately 34 MeV, at tandetron 6 MeV. The range of these ions in water is only several tens of micrometers (range of 6 MeV protons in water is approximately 0.5 mm, in case of 34 MeV protons about 11 mm). Therefore, the experiments should be performed with thin biological samples.

Several particular experimental setups has been designed and tested:
a) own developed prototype rings from plastic or metal extending thin Mylar foil
b) sterile Petriho dishes with glass bottom
c) commercially available plastic dishes with cover and bottom from Mylar foil (Chemplex, USA).
As the best solution for further experiments with neonatal dermal fibroblasts seems the last proposed setup using plastic dishes. Petri dishes with glass bottom will be used for experiments with our colleagues from Biophysical Institute ASCR, which analyze irradiated samples by FISH technique (fluorescence in situ hybridization). Cells are seeded 24 h before irradiation and grown directly on glass slide. DNA plasmids in water solution are irradiated in thin plastic tubes.

The proportion of direct and indirect effects in proton tracks has been followed in pBR322 DNA plasmids in water solution. Samples were irradiated in presence of increasing concentrations of OH radical scavengers (coumarin-3-carboxylic acid, dimethylsulfoxid or glycylglycine). The yields of single and double DNA strand breaks were determined by agarose gel electrophoresis. The contributions of direct and indirect DNA damage in dependence on scavenger concentration has been determined for 30 MeV protons. The experiments will be extended for larger interval of proton energies and also other types of ions.

Radiation damage to proteins has been studied for selected restriction enzymes HindIII and PvuII. Enzymes irradiated by increasing doses were subsequently with DNA pCDNA3 plasmids. Restriction enzymes recognize and cleave specific DNA base sequences. The functionality of irradiated restriction enzymes can be thus followed by agarose gel electrophoresis, where DNA fragments of known size can be easily visualized. Decrease of enzyme activity with increasing absorbed dose has been detected.

During the first year of the project, the results for cell cultures have not been planned. In the frame of planning of experimental studies, methods and experimental setup has been proposed and prepared. The first pilot experiments have been realized too. Cell survival curves have been determined for confluent neonatal fibroblasts grown on 2.5 μm Mylar foils and irradiated by gamma radiation and 15 and 30 MeV protons. In irradiated samples the cell survival and micronuclei formation has been determined. Experiments will be repeated, extended and analyzed. In collaboration with Biophysics Institute ASCR, the first experiments focused to DSB repair in normal neonatal skin fibroblasts have been performed.

# Carbon 12C Test Beam

Laboratory of Cyclotron and Fast Neutron Generators

Tomáš Matlocha

Proposal ID

310

# U-120M carbon $^{12}C^{6+}$ beam test - Final report

**Tomas Matlocha**

### Proposal's realization:

The CANAM proposal id 310 was realized during 5.-7. 4. 2017 as an appendix to a Deflection system test. The U-120M cyclotron was tuned in positive regimes for Deuterium 14.1 MeV and for Deuterium 17.3 MeV. Positive ion beams for various gases were extracted using deflection system to the beamline A diagnostic unit.

### Cyclotron parameters:

**DT 14,1 MeV:**

EMC = D – 318.6 A , C – 313.2 A

f=11.62 MHz, U_dee=30 kV

Udef1=42.9 kV, Udef2=21.6 kV, Udef3=37.8 kV

**DT 17,3 MeV:**

f=12.86 MHz, U_dee=34 kV,

EMC = D – 438.8 A , C – 430.85 A

Udef1=53.6 kV, Udef2=21.7 kV, Udef3=23.8 kV

For DT 14.1 MeV deuterium, helium and methane was filled. For DT 17.3 MeV deuterium, methane and $CO_2$ was filled.

**Ion source in high impedance mode:**

Arc current = 0.13 A  Arc voltage = 1700 V

### Measurement:

Direct beam current over 1nA was measured with cyclotron internal current meters. For currents below 1 nA, the electrometer Keithley 614 was used. The beam diagnostics and the ion energy measurement was done using the silicon pixel detector TimePIX.

The various accelerated ion types were separated by a proper tuning of the resonance by the cyclotron main coil for ion mass to charge ratio m/Q as shown in the table below.

| m/Q [u/e] | EMC (14.1 MeV) | EMC (17.3 MeV) |
|---|---|---|
| **2.014** | 318.6 A | 438.8 A |
| **2.000** | 313.2 A | 430.85 A |

At the resonance for m/Q = 2.014 (deuterium) with ionization of methane a massive fraction of single ionized molecular hydrogen $H_2^+$was measured. Maximal current was 30 uAe. At the resonance for m/Q = 2.000, a maximal measured current was 1pAe. By ionization of $CO_2$, maximal current for m/Q was 100 pAe. The ions clusters detected by the TimePIX detector are in figures below and have area about. 50 x 50 pixels.

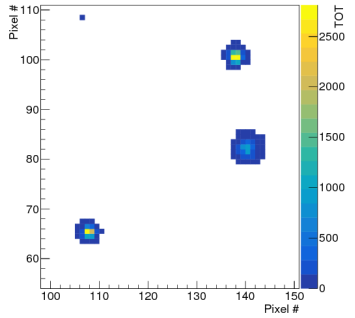


*Fig. 1: Molecular hydrogen H2+*

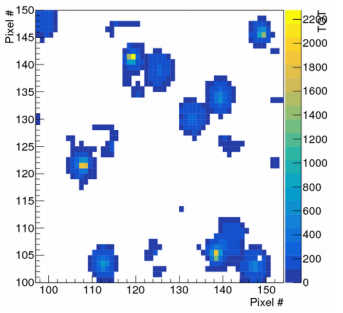


*Fig. 2: Helium 4He 2+*

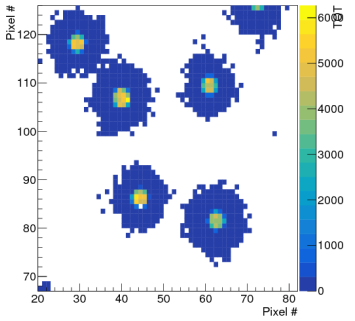


*Fig. 3: Carbon 12C candidate*

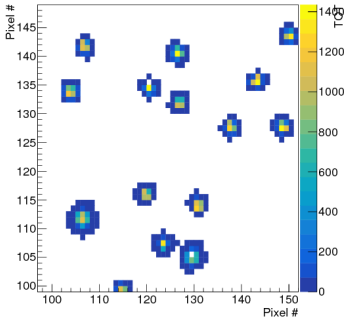


*Fig. 4: Deuterium 2H*

Maximum energy measured for ions accelerated from ionized methane was 25 MeV at 14.1 MeV. Helium $^4He^{2+}$ with 28 MeV should left 16 MeV in 300 um TimePIX silicon chip. Energy deposit in the chip left by deuterium 14 MeV is 3.6 MeV. Carbon $^{12}C^{6+}$at 85 MeV should left its complete energy in the detector. Molecular hydrogen 14 MeV deposit is approx. 8 MeV.

Ion energies obtained by analysis of the TimePIX data are in Fig. 5. The results are strongly affected by changing the TimePIX THL level. The change was necessary because of a high radiation background. Also TimePIX non-linear response and non-ionization loses affected the energy scale in the measured energy distribution. From the comparison of $H_2$ end $^4$He plot can be seen that for $^4$He the real measured ions were probably the molecular hydrogen $H_2^+$, so direct comparison between $^4$He and $^{12}$C is not available.

### Results:

Heavy ions with m/Q ratio in range 1.998 – 2.002 were observed at intensities up to 100 pAe with energy deposit in TimePIX detector approx. 25 MeV. Resolution of carbon and helium ions is not clear. For a clear distinction between these ions with almost identical m/Q, a further measurement with another detector type is necessary.

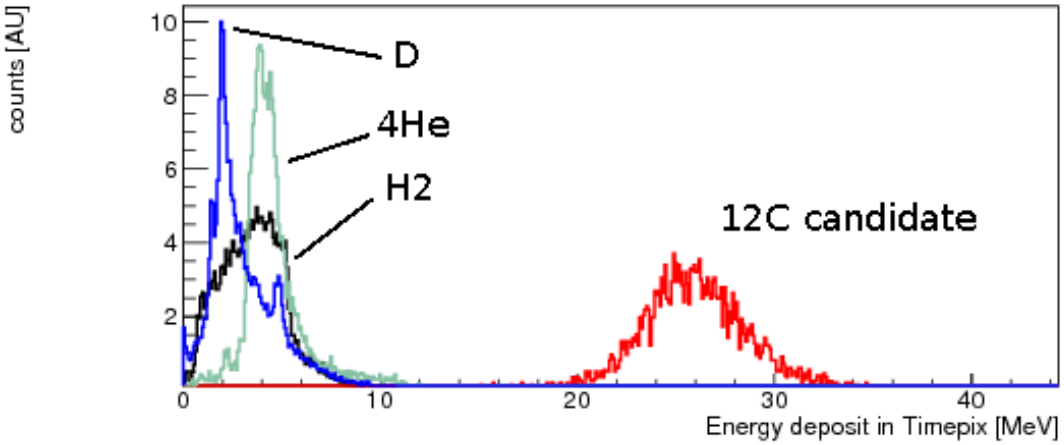


*Fig. 5: Energy plots*

# Residual stress measurement

Neutron Physics Laboratory - Neutron diffraction

Josef Hodek

Proposal ID

311

**Final report 'Residual stress measurement'**

J. Hodek, A. Prantl, COMTES FHT a.s., Dobrany, Czech Republic

Residual stress is hard to obtain for bulk objects. The contour method can determine residual stress distribution for bulk objects. The neutron diffraction measurement was done to obtain measurement that can be comparable to the contour method computation and the finite element method computation of the heat treatment. The sample was a stainless cylinder with sizes D58/60mm. There were measured only strains in two directions due to sizes of the sample. The computation both the contour method and the finite element method were done in MSC MARC computation software.

Comparison was done on the lines 01-04 see Figure 1

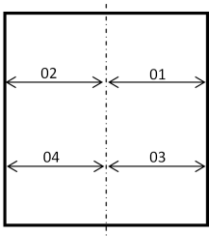


**Figure 1 Identification of the comparison lines**

The strain distributions are on the Figure 2 - Figure 4.

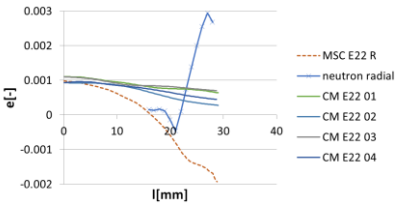


**Figure 2 Strain - radial**

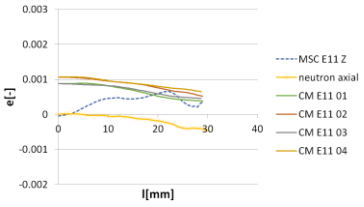


**Figure 3 Strain - axial**

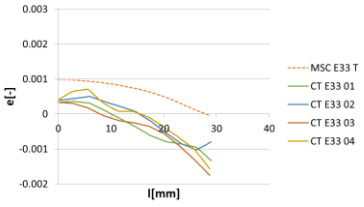


**Figure 4 Strain - tangential**

where: MSC – the finite element computation

CM – the contour method computation

neutron – the neutron diffraction measurement

# Radiation Hardness of Si Pixel Chips and Components for ALICE Inner Tracker System Upgrade Project

Laboratory of Cyclotron and Fast Neutron Generators

Filip Krizek

Proposal ID

313

# Report regarding the proposal: Radiation Hardness of Silicon Pixel Chips and Components for the ALICE Inner Tracking System Upgrade Project

Filip Křížek, Nuclear Physics Institute of CAS

The ALPIDE chips are monolithic active pixel sensors which are going to be used in the upgraded Inner Tracking System (ITS) detector of the ALICE experiment at CERN. In 2017, we continued with the tests of their radiation hardness and we studied the chip performance as a function of the accumulated total ionization dose (TID) and reverse substrate bias. The corresponding measurements were carried out on 19.1., 1.3., 2.3., 10.4., 3.5., 4.5., 15.6., 24.7., 28.8., 18.9., 11.10., and 6.11. Figure 1 shows an example of the obtained dependence of the chip sensitivity threshold as a function of the accumulated TID. At present the sensor accumulated a TID of 1.6 Mrad and is still fully operational. The chips irradiated at Rez were then further characterized at the test beams at the CERN PS. Results from this activity were published in the diploma thesis of Artem Isakov [1] and were presented on regular meetings of the ITS upgrade characterization group (10.5., 4.10., 25.10.). In the test performed on 14.6., we irradiated chips on the inner barrel stave and found that they follow the expected behavior. Further tests of radiation hardness were performed also with a field programmable gate array (FPGA) and the corresponding firmware design which are going to be used in the ITS readout unit (RU). On 22.–24.5. and 19.–20.6. we irradiated a RU prototype based on the Xilinx Kintex-7 325T FPGA. The goal of the test was to investigate various soft error mitigation firmware designs. Results from this activity were presented by Krysztof Sielkiewicz at the NSREC-2017 conference [2]. The final version of the RU based on Xilinx XCKU060 FPGA was tested during 4.–6.12. These measurements provide an important data for the Production Readiness Review of the ITS RU project which will take place in spring 2018.

## References

[1] A. Isakov, *Investigation of silicon pixel sensors for the ALICE Inner Tracking System upgrade project*, diploma thesis, Tomsk Polytechnic University, 2017.

[2] K. Sielkiewicz et al., *Experimental Methods and Results for the Evaluation of Triple Modulator Redundancy SEU Mitigation Techniques with the Kintex-7 FPGA*, IEEE NSREC-2017 conference.

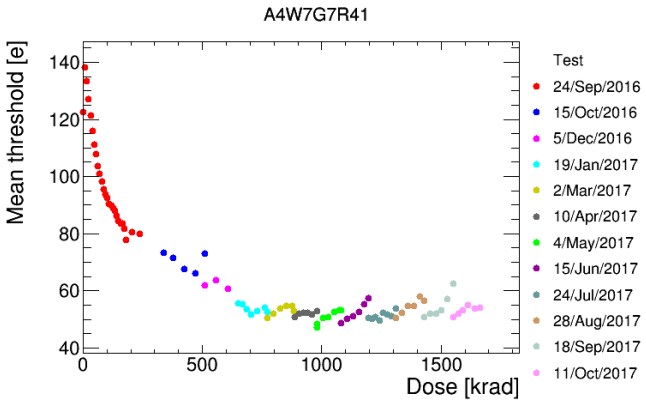


Figure 1: ALPIDE sensor sensitivity threshold as a function of the accumulated total ionization dose. The threshold is measured in electron charges. The sensor was irradiated with a beam of 30 MeV protons. The legend quotes the dates of irradiation campaigns.

# Study of CR-39 response to short range nuclei with the purpose of space radiation track analysis

Laboratory of Tandetron

Konstantin Inozemtsev

Proposal ID

314

Report on CANAM Research Project

# "Study of CR-39 response to short range nuclei with the purpose of space radiation track analysis" (*Proposal ID 314*; April, 23-28 2017)

*K.O. Inozemtsev*[1,2,*], *V.V. Kushin*[1,2], *V. Havránek*[3], *O. Ploc*[3], *I. Ambrožová*[3] and *V.A. Shurshakov*[2]

[1] National Research Nuclear University MEPhI (Moscow Engineering Physics Institute), Moscow, Russian Federation
[2] Russian Academy of Sciences, Institute of Biomedical Problems (IBMP), Moscow, Russian Federation
[3] Czech Academy of Sciences, Nuclear Physics Institute, Řež, Czech Republic

**Scope**

The purpose of this Project is to study the solid state nuclear track detector (SSNTD) CR-39 "Tastrak" response to particles with variable energy losses dE/dx in the Bragg peak vicinity. Low energy H and C nuclei are appropriate to simulate tracks of secondary nuclear fragments in the composition of cosmic rays onboard a spacecraft [1].

Since the key track parameter – etch rate ratio (sensitivity) $V$ is associated with dE/dx value, it is sufficient to use original scanning techniques and track analysis [2].

Results of this study are necessary for the reliable measurement of secondary space radiation [1] in the forthcoming joint "CZENDA" experiment onboard BION-M2 spacecraft, "MATRYOSHKA-R" and "PHOENIX" projects onboard the International Space Station.

**Experiment**

The series of CR-39 SSNTDs were irradiated at the LT laboratory of *NPI CAS* with H and C ions in the Bragg peak vicinity. The irradiation conditions are specified in Table 1.

**Table 1**

**The specification of ion species, energies and incident angles**

| Ion | Initial Energy [MeV] | LET ($H_2O$) on detector surface [keV/μm] | Incident angles, ° |
|---|---|---|---|
| H | 5.8 | 7.5 | 85, 90 |
| | 4 | 9.7 | 75, 90 |
| | 2 | 16.4 | 60, 75 |
| | 1.5 | 20.0 | |
| | 1 | 24.0 | 45, 60, 75 |
| C | 18 | 614 | 45, 60 |
| | 15 | 674 | |
| | 10 | 803 | 30, 45, 60, 75, 90 |

**Methods**

After irradiation, the SSNTD species were etched in 6 N NaOH solution under 70° C. The corresponding bulk etch ratio was 1.3 $\mu m^{-1}\cdot hr$. The etching duration was selected for each sample individually, taking into account the etch rate ratio and incident angle.

After chemical etching, the sets of track geometrical parameters are measured: the (*D,d,H*) set was measured for all tracks and (*D,d,l*) set was measured if possible. The abovementioned track parameters are: $H$ – the removed layer thickness, $d$ – the minor track opening ellipse diameter, $D$ – the major track opening ellipse diameter, $l$ – the track full projected length. These parameters were used to evaluate the values of mean etch rate ratio $V$, incident angle, amount of bulk etch and etched track length (residual range).

The track scanning was performed on Carl Zeis® AxioScope.A1 optical microscope manually.

Track data were processed with the use of two alternative approaches described in detail in Ref. [2].

**Results**

The evolution of etch rate ratio $V$ for protons versus initial energy, etching time $T$ and incident angle is presented in Fig.1 in comparison with *Hermsdorf, 2009* data [3].

The track data, obtained for the 1 MeV protons after 11 and 12 hr etching and Carbons after 1 hr etching allowed estimating the particle's residual range. The experimental values of residual range are compared with *SRIM-code* data [4] in Table 2.

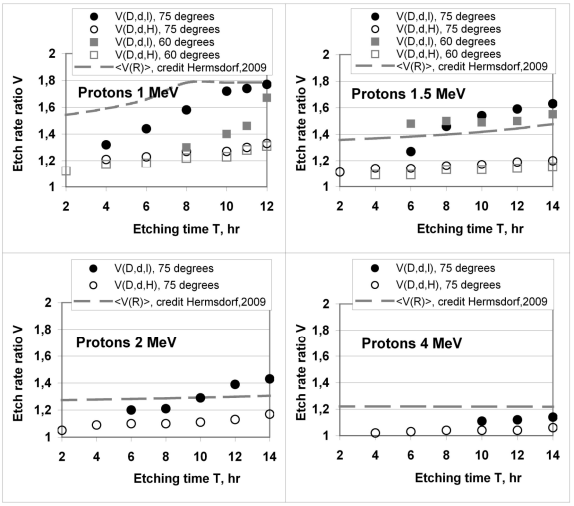


**Fig.1.** Evolution of etch rate ratio $V$ measured with the use of different sets of track geometrical parameters [1] versus etching time and incident angle in comparison with *Hermsdorf* data [3]. Experimental errors are < 5 % for *V(D,d,H)* data, and 10-15 % for *V(D,d,l)* data.

**Table 2**

**The comparison of experimental and theoretical values of ion's residual ranges**

| Ion | Initial Energy [MeV] | Mean residual range in CR-39 [keV/μm] | Theoretical residual range in CR-39, [keV/μm] |
|---|---|---|---|
| H | 1 | 15.84±1.21 | 19.81 |
| C | 18 | 16.41±1.26 | 20.41 |
| | 15 | 12.97±0.62 | 16.59 |
| | 10 | 9.31±0.49 | 10.96 |

The data obtained for 5.8 MeV protons allowed to estimate the SSNTD "Tastrak" lower LET threshold in ~ 9 keV/μm (in CR-39 material).

**Summary**

In this experiment, the data concerned the response of the CR-39 detector to the short-range protons and carbon nuclei are obtained. Two alternative approaches [2] are applied to estimate the key track parameter – etch rate ratio $V$. The results of the experiment are planned to be submitted to one of the international journals.

**References**

[1] Inozemtsev, K.O., Kushin, V.V., Kodaira, S., Shurshakov, V.A. *Observation of fragmentation events caused by space radiation: contribution to the LET spectrum as measured with CR-39 track detectors*, Radiation Measurements, 95, pp. 37-43, 2016

[2] Inozemtsev, K.O., Kushin, V.V. *Comparative analysis of CR-39 sensitivity for different sets of measurable track parameters*, Radiation Measurements, 91, pp. 44-49, 2016

[3] Hermsdorf, D. *Measurement and comparative evaluation of the sensitivity V for protons and hydrogen isotopes registration in PADC detectors of type CR-39*, Radiation Measurements, 44, (9–10), pp. 806-812, 2009

[4] Ziegler, J.F., Ziegler, M.D., Biersack, J.P. *SRIM – The stopping and range of ions in matter (2010)*, Nuclear Instruments and Methods in Physics Research Section B: Beam Interactions with Materials and Atoms, 268, (11–12), pp. 1818-1823, 2010

**Acknowledgments**

Authors would like to thank the stuff of the LT Laboratory for the perfect experiment, Mrs. Markéta Sommerová for the visit arrangement, and Dr. Anna Macková for the experiment organization.

* Project proposer, mailto: dio2014@yandex.com

# INTERNAL: Studying of nanoscaled precipitation in NiTi wires by SANS

Neutron Physics Laboratory - Neutron diffraction

Vasyl Ryukhtin

Proposal ID

187

# Studying of nanoscaled precipitation in NiTi wires by SANS

V. Ryukhtin, J. Pilch, Nuclear Physics Institute NPI (ASCR), Neutron Physics Department

NiTi shape memory alloy has been widely investigated and utilizedin a wide range of engineering application in medicine, aerospace and automotive sectors. Precipitation of finely dispersed $Ni_4Ti_3$ particles in Ni-rich (superelastic) alloys has been claimed effective in increasing fatigue life. Final microstructure of cold worked/heat treated NiTi strongly depends on the temperature and time of the heat treatment which controls precipitation processes, recovery of dislocation networks (residual stress relaxation) and recrystallization and through them the material properties (tensile strength, yield stress, transformation stresses, transformation strain,transformation temperatures and possibly the fatigue performance).

This measurements are part of investigation of precipitation behaivior in nano-grained NiTi materials. Measured data were fitted using sprerical model and the fitted functions are shown in Fig. 1. The mean size monotonically increases with temperature values.

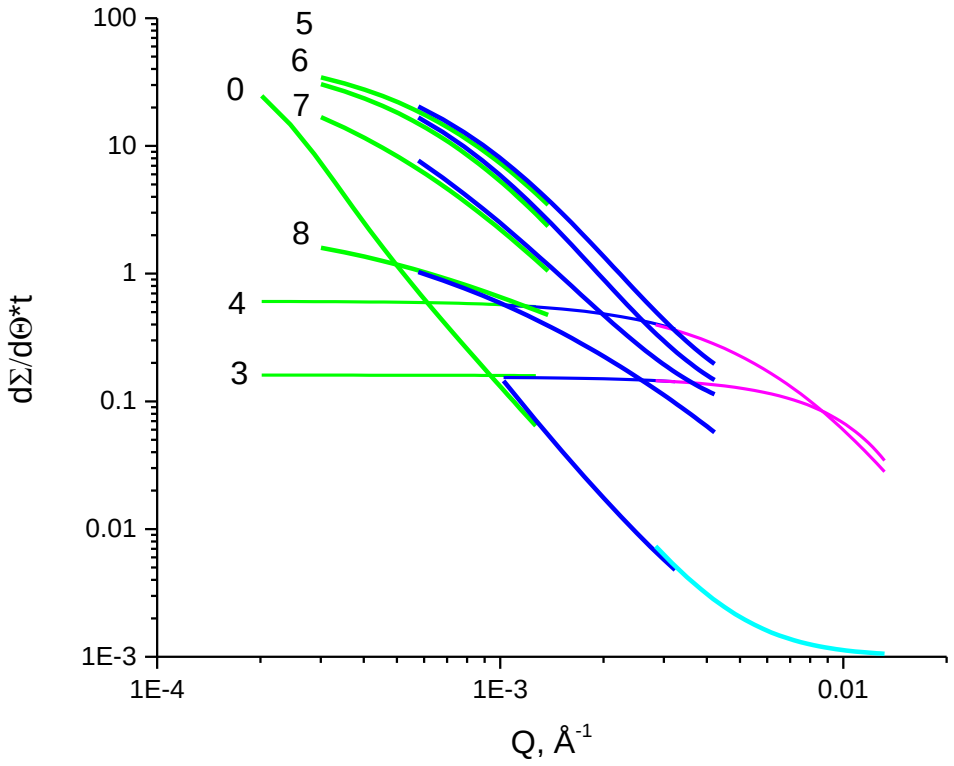


Fig. 1. Fitted SANS curves measured at MAUD.

# Phase analysis of HSSs

Neutron Physics Laboratory - Neutron diffraction

Darya Novikova

Proposal ID

315

# Report regarding proposal “Phase analysis of HSSs”

D. Novikova, Technopark Kralupy, UCT Prague, Czech Republic
P. Beran, Nucl. Physics Inst., Rez, Czech Republic

Neutron diffraction experiments were performed on two CP1000 and DP1000 specimens using MEREDIT instrument. The motivation of experiment was to study phase fractions content of CP1000 and DP1000 steels.

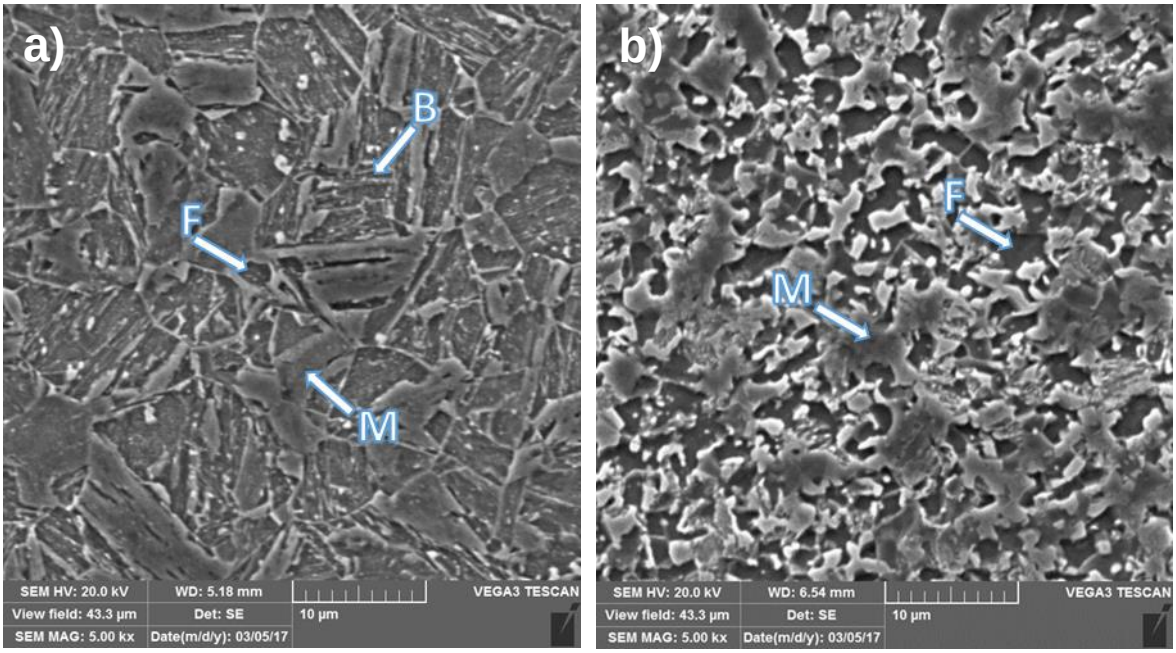


Fig. 1: SEM images of a) CP1000 and b) DP1000

Results obtained from neutron diffraction are shown in Table 1 and Table 2.

| | Phase N.1 martensite-alpha | Phase N. 2 ferrite | Phase N. 3 austenite |
|---|---|---|---|
| CP1000 | 2.87631(94) Å | 2.86551(91) Å | 3.6051(54) Å |
| DP1000 | 2.8738(13) Å | 2.8655(17) Å | 3.6022(24) Å |

Table 1: Unit cell parameters

| | Phase N.1 martensite-alpha | Phase N. 2 ferrite | Phase N. 3 austenite |
|---|---|---|---|
| CP1000 | 47.2 ± 1.22 % | 51.86 ± 1.26 % | 0.94 ± 0.05 % |
| DP1000 | 62.15 ± 3.1 % | 35.88 ± 2.6 % | 1.96 ± 0.08 % |

Table 2: Phase fractions

Martensite, ferrite and austenite volume content was evaluated. Martensite and ferrite phases were distinguished based on small differences in lattice parameters. Content of ferrite and martensite were in agreement with results from SEM and colour metallography analysis. CP1000 steel might also contain bainite fraction, but it was not possible to distinguish bainite from martensite using neutron diffraction results.

These results were used for conference paper [1]. It is also will be used for a paper about microstructure characterization of CP1000 and DP1000 steels.

[1] D. Rudomilova, T. Prosek, A. Muhr, H. Duchaczek, G. Luckeneder, P. Novak, P. Salvetr, P. Beran, Hydrogen permeability of high strength steels and model structures, SteelHydrogen2018 Proceedings (2018).

# Radiation Hardness of Si Pixel Chips and Components for ALICE Inner Tracker System Upgrade Project

Laboratory of Cyclotron and Fast Neutron Generators

Jozef Ferencei

Proposal ID

60

# CANAM project:
# "Radiation Hardness of Si Pixel Chips and Components for ALICE Inner Tracker System Upgrade

During the course of 2013 year the following measurements were made in U-120M cyclotron of Nuclear Physics Institute in the framework of CANAM project Nr. 60 "Radiation Hardness of Si Pixel Chips and Components for ALICE Inner Tracker System Upgrade":

1. Series of measurements to determine Single Event Upset (SEU) probability for SRAM memories in 180 nm technology from TowerJazz foundry in Israel, foreseen for mass production of silicon pixel chips for ALICE inner tracker system upgrade. Results confirmed the acceptable SEU rate at the level of $10^{-13}$ $cm^2bit^{-1}$ causing rather tolerable data corruption (~$10^{-9}$ $bit^{-1}$ for central most affected chip) with no necessity for special expensive protections. This is important verification of technology suitability for production of monolithic active pixel sensors (MAPS) with on-chip integrated electronics. Measurements at U-120M cyclotron together with the ones carried at higher energies in Paul Scherer Institute in Villigen, Switzerland are part of the published "*Technical Design Report for the Upgrade of the ALICE Tracking System*", CERN-LHCC-2013-024, ALICE-TDR-017, which is available at CERN document server using the following URL: http://cds.cern.ch/record/1625842/files/ALICE-TDR-017.pdf?version=3 (pages 38-39). This document was submitted to 116th meeting of LHC Experiments Committee held on 4.12.2013 for endorsement. Investigations will continue using higher beam currents to study Single Event Latch-ups, i.e. the functional failure studies.
2. After careful selection procedure made in CERN the suitable fast (up to 6 Gbit/s) signal cable candidate 30 AWG Micro Twinax Cable from Samtec Company was chosen. Proton irradiation up to the total ionization dose of 1 Mrad was made in U-120 M cyclotron. The cable was shipped back to CERN, where measurements using fast oscilloscope with specialized pseudo random bit sequence generator confirmed unchanged bit error rate probability. This activity will continue for the laminated version of same type of cable, which is more compact w.r.t. non-laminated version.
3. For ALICE Inner Tracker System upgrade project the field-programmable gate arrays (FPGA) are foreseen to cope with expected enormous data volume (up to 30 Gbit/sec). As these FPGA will be located in LHC accelerator radiation environment, the unavoidable selection procedure of radiation hard commercially available FPGA was initiated. To precede with this complex task two PhD students from Faculty of information technology Czech technical university in Prague joined our group. First test measurements using Xilinx Spartan XC3S200 FPGA were already made. The detailed radiation hardness studies of modern Flash FPGA (expected to be more radiation hard) SmartFusion2 from Microsemi Company are in preparation.

# INTERNAL: Measurements of structural anisotropy in natural rock samples using SANS technique

Neutron Physics Laboratory - Neutron diffraction

Vasyl Ryukhtin

Proposal ID

188

# Measurements of structural anisotropy in natural rock samples using SANS technique

V. Ryukhtin, Nuclear Physics Institute NPI (ASCR), Neutron Physics Department

S. Vratislav, Czech Technical University in Prague, Department of Solid State Engineering

The samples were exposed by neutrons of 2.09 Å wavelength. Resulted scattering intensities are significantly depended on sample orientation (see Fig. 1). Quite straightforward model of prolate elipsoids was chosen for simultaneous fitting of both orientations using *SASprofit* program [1]. Longer axis of the ellipsoids was fixed at $18^0$ with respect to **y** for sample VS1 and at $22^0$ - for sample VS2 (see inserted drawing in Fig. 2). Orientation of prolate inhomogenities was obtained by measuring of total scattering intensity in dependence on angle **x** and **Q**. Maximum of the intensity corresponds to orientation where longer axis of prolate ellipsoids is parallel to scattering vector **Q** (*i.e.* horizontal). Scattering length density contrast ($\Delta\rho = 4.8 \cdot 10^{-6}$ Å$^{-2}$) was calculated empirically from tabular values of natural calcite. Values aspect ratio of ellipsoids were obtained c/R= 4.29 ± 0.69 for VS1 and c/R= 2.136 ± 0.093 for VS2 sample respectively, by another words, microstructure in sample VS1 is twice more elongated than in VS2.

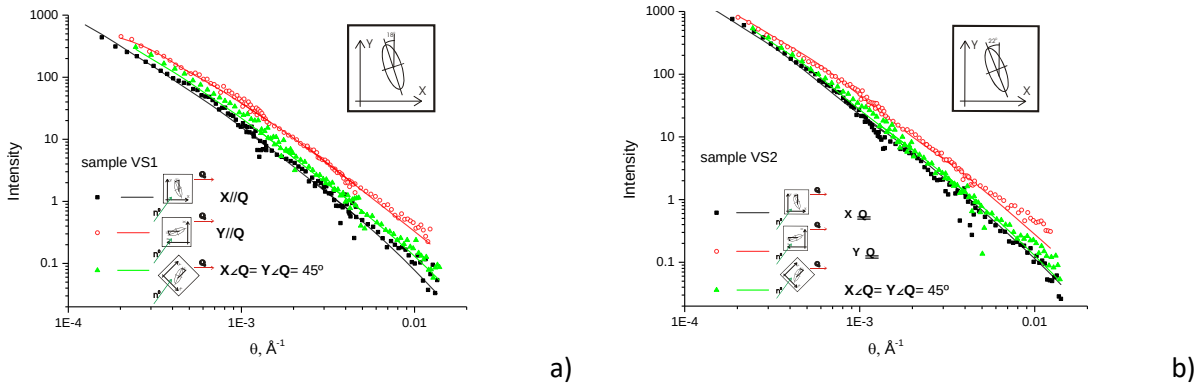


***Fig. 1.*** *SANS scattering functions (points) with fitted models (lines) of prolate ellipsoids with longer axe inclined to* ***Y*** *for sample VS1 at $18^0$ (a) and VS2 - $22^0$ (b) as shown in the inserted draw.*

To summarize fitting results one can conclude that inhomogenities in sample VS2 are larger but less anisotropic then in VS1 while total volume fraction is practically the same.Scattering curves measured nearly obeys exponentional dependence with noninteger power (D~2.3). It is typical behavior for mass fractal systems, so we can expect selfsimilarity in structure within measured size range.

## Reference

1. J. Šaroun, SASProFit - program for USANS data evaluation, IConUSAS conference, Oak Ridge, 9-10 July 2003.

# Excitation functions of the of proton- and deuteron-induced reactions on Zn-64, As-75, Y-89, Mo-100

Laboratory of Cyclotron and Fast Neutron Generators

Ondrej Lebeda

Proposal ID

64

## Excitation functions of the of proton- and deuteron-induced reactions on $^{64}$Zn, $^{75}$As, $^{89}$Y, $^{100}$Mo

Ondřej Lebeda, Vlasta Zdychová, Jaroslav Červenák and Jan Štursa

*Nuclear Physics Institute, Řež, Czech Republic*
*Czech Technical University, Prague*

Detailed measurement of the deuteron-induced excitation functions on $^{89}$Y in the energy range of 3.9–19.5 MeV was performed resulting in new excitation function for formation of $^{88}$Zr, $^{89m}$Zr, $^{89}$Zr, $^{88}$Y, $^{90m}$Y and $^{87m}$Sr (Fig. 1). The data were compared with previously published results and prediction of the TALYS code. Parallel use of titanium and aluminium beam monitors revealed systematic difference between the recommended cross-sections of both monitoring reactions and provided new cross-section data for formation of $^{24}$Na, $^{27}$Mg, $^{43}$Sc, $^{44m}$Sc, $^{44}$Sc, $^{46}$Sc, $^{47}$Sc and $^{48}$Sc (Fig. 1). Results were published in a peer-reviewed journal [1] and included in the EXFOR data base.

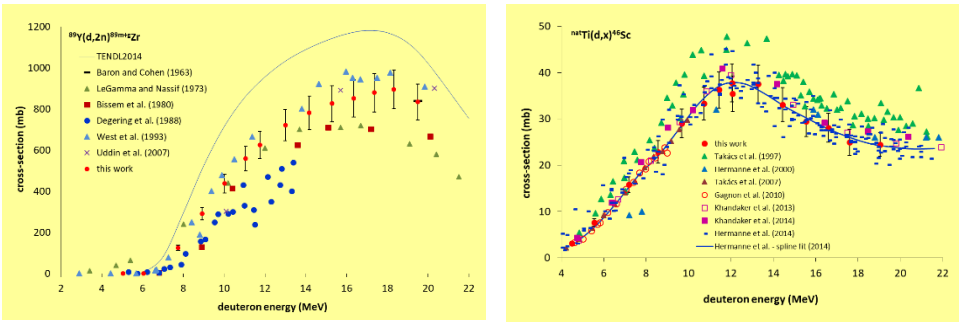


Fig. 1 Excitation function of the $^{89}$Y(d,2n)$^{89m+g}$Zr for the formation of medically relevant $^{89}$Zr amd excitation function of the $^{nat}$Ti(d,x)$^{46}$Sc suitable for the beam monitoring

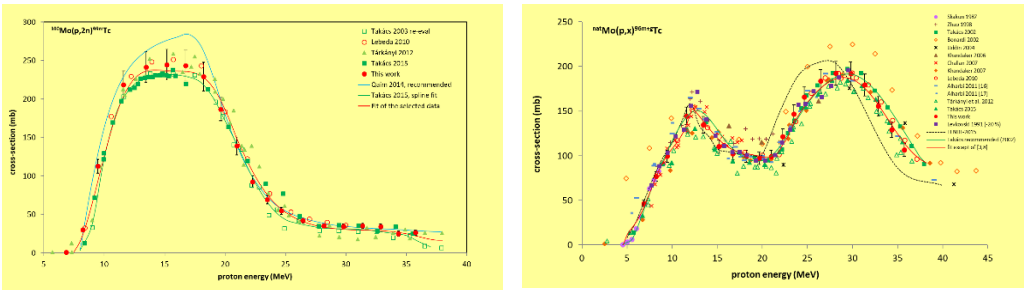


Fig. 2 Selected cross-sections for the $^{100}$Mo(p,2n) nuclear reaction and fit of the recommended values; cross-sections for the beam monitoring reaction $^{nat}$Mo(p,x)$^{96m+g}$Tc and their fitting resulting in the recommended data

Due to the lack of thin foils of precise thickness made out of highly enriched metals, we decided to re-measure excitation functions of protons on natural molybdenum, as the elemental cross-sections may be in the case of the nuclear reactions on $^{100}$Mo converted into isotopic cross-sections. The extensive experiment allowed us then to provide another set of data important not only for the production of medically relevant $^{99m}$Tc and $^{99}$Mo, but also for the $^{nat}$Mo(p,x)$^{96m+g}$Tc reaction relevant for both beam monitoring and TLA, as well as data for production of $^{95m}$Tc, a suitable long-lived technetium tracer. Altogether, almost 30 excitation functions were obtained covering the proton beam energy range of 7–36 MeV, some of them were provided for the first time ($^{97m}$Tc, $^{88g}$Nb, $^{88m}$Nb and $^{89m}$Nb) [2]. Results are included in the EXFOR data base.

Due to the problems with the target preparation, we have resigned on the measurement of the proton-induced excitation functions on $^{64}$Zn. The sputtered targets made out of $^{75}$As were not suitable for the proton beam activation, the bombardment resulted in their significant damage that didn't allow for obtaining reliable data.

The rich experimental material collected during the experiments was then included in an extensive works performed within the IAEA CRP project.

[1] Lebeda, O. – Štursa, J. – Ráliš, J. Experimental cross-sections of deuteron-induced reaction on $^{89}$Y up to 20 MeV; comparison of $^{nat}$Ti(d,x)$^{48}$V and $^{27}$Al(d,x)$^{24}$Na monitor reactions. *Nuclear Instruments and Methods in Physics Research B*, 2015, vol. 360, pp. 118–128.
doi: 10.1016/j.nimb.2015.08.036

[2] Červenák, J. – Lebeda, O. Experimental cross-sections for proton-induced reaction on $^{nat}$Mo. *Nuclear Instruments and Methods in Physics Research B*, 2016, vol. 380, pp. 32–49.
doi: 10.1016/j.nimb.2016.05.006

# Study of energy loss and energy straggling of heavy ions in polymers, silicon nitride and SOI.

Laboratory of Tandetron

Romana Mikšová

Proposal ID

199

**Report regarding proposal "Study of energy loss and energy straggling of heavy ions in polymers, silicon nitride and SOI."**

R. Mikšová, V. Hnatowicz, A. Macková, P. Malinský, Nucl. Physics Inst., Rez, Czech Republic
P. Slepička, Inst. Chem. Tech., Prague, Czech Republic

Our results of $C^{n+}$ and $O^{n+}$ ions the stopping powers in PP and $Si_3N_4$ show systematic differences between the experimental and semi-empirical predicted data. More significant discrepancies between the experimental and predicted stopping power of heavier O ions in SRIM and MSTAR code can be a result of a more significant radiation damage of the irradiated PP accompanied by the escape of volatile fragments. In the case of experimental straggling better comparison provides Yang's theory for both ion species than the Bohr and Bethe–Livingston theories. The Yang formula systematically underestimates the measured values with an average deviation of about 3–24% for silicon nitride and 4–25% for PP.

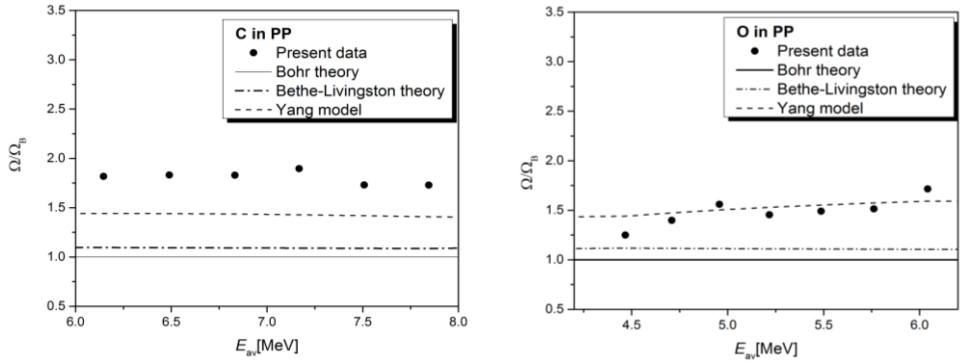


Figure 1. Experimental reduced ($\Omega/\Omega_B$) for (a) C and (b) O in PP (points) versus reference energy, compared to straggling predicted values by Bohr, Bethe–Livingston theories and Yang's empirical formula (lines).

The channelling stopping power decreases with increasing energy, which is a general trend for both ion species. At higher ion energy, the differences between the channelling and random stopping powers of helium ions are quite similar to those obtained for lithium ions, so that for both ion species at higher energy the channelling stopping powers are close to 50 % of the random stopping powers (see Figure 2). This confirms the basic theory that the best channelling ions have a stopping power in the order of one-half of the stopping power in the corresponding random direction.

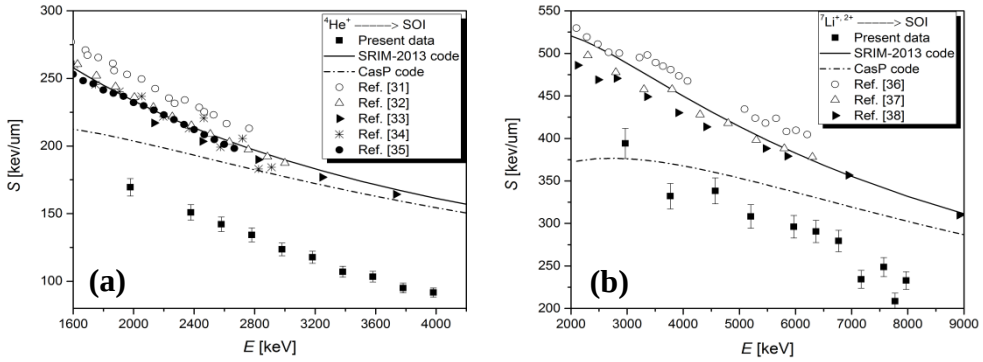


Figure 2. The experimental stopping powers for helium (a) and lithium (b) ions along the ⟨100⟩ direction in Si (points) and the calculated random stopping powers using SRIM-2013 (solid line), the UCA model from the CasP code (dash-dot line) and the experimental random stopping powers from literature for comparison (points).

The results have been accepted for publication in NIMB Proceedings

# Ion-implantation of erbium into the nanocrystalline diamond thin films

Laboratory of Tandetron

Pavla Nekvindová

Proposal ID

223

In the frame of CANAM program 2015 the single-crystalline diamond and NCD films was implanted by $Er^+$ ions. Four samples of single-crystals and nine samples of NCD films were implanted with 190 keV energy $Er^+$ ions (7° off-axis to avoid channeling) with the fluences of $1.0\times10^{14}$, $1.0\times10^{15}$ and $5.0\times10^{15}$ ion/cm$^2$. The ion implantation was performed at 200 kV ion implanter in the Helmholtz-Zentrum, Dresden-Rossendorf, Germany. The concentration-depth profiles of the incorporated erbium were measured by Rutherford Backscattering Spectroscopy (RBS). The damages introduced by the implantation process to the host lattice were examined in single-crystal wafers by RBS/channelling measurements using a 1.7 MeV $He^+$ beam at VdG. The analysis was performed at Tandetron Laboratory NPI.

*Single-crystals:* From the theoretical model it turned out that both the substitutional and the interstitial erbium positions models are able to exist without serious structure changes or bond cracking. According to the comparison of the cohesive energies of two theoretical structural models, more probable erbium location in diamond is substitutional site of carbon. The ion implantation process in single crystal caused substantial damage to the structure of implanted layer of up to 69% of disordered atoms, and the absolute erbium positions in the structure therefore could not be determined.

*NCD-films:* The prepared NCD thin films guided up to two optical modes in the range of 633–1552 nm. It was found out that for the waveguiding to occur the size of grains of more than 100 nm should be used (according to experimental conditions used). The erbium ion implantation process affected the waveguiding properties negligibly – the value of refractive index of 2.3394 for 1552 nm decreased by approximately 1.3 % after the ion implantation process. The erbium implanted NCD samples with higher concentration of grain boundaries (corresponded to the smaller grain sizes of less than 25 nm) revealed measurable luminescence at around 1530 nm.

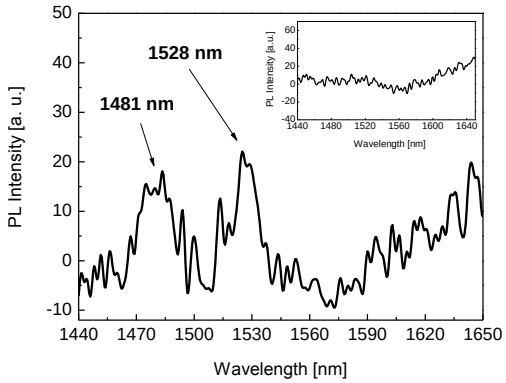


**Fig. 1** The luminescence spectra of the erbium-doped NCD film and of the the erbium-doped diamond single-crystal (100) sample (inset graph). (*Experimental conditions:* 190 keV $Er^+$ ions, a fluence of $1.0\times10^{14}$ cm$^{-2}$)

Moreover same experiments with co-implantation with Yb and Al were also done, but their characterization has not been yet completed. In the experiments we would like to continue in the next year.

Two papers on the results of the experiments have been submitted at journals (see list of publication).

**List of publication:**

1. Jakub Cajzl, Pavla Nekvindová, Oleg Babchenko, Alexander Kromka**,** Anna Macková, Petr Malinský, Jiří Oswald, Václav Prajzler, Zdeněk Remeš, Marian Varga: *Ion-implantation of erbium into the nanocrystalline diamond thin films* – submitted at Journal of advanced materials in optoelectronic

2. Cajzl J. , Nekvindová P. , Macková A., Malinský P., Sedmidubský D., Hušák M., Remeš Z., Varga M. , Kromka A., Böttger R.: *Erbium ion implantation into diamond – measurement and modeling of the crystal structure* - submitted at *Physical Chemistry Chemical Physics*

# Effect of applied magnetic field on internal structure of multiferroi nanocomposites

Neutron Physics Laboratory - Neutron diffraction

Aleksandr Naberezhnov

Proposal ID

228

**Effect of applied magnetic field on internal structure of nanocomposites with coexisting magnetic and ferroelectric orderings**

Instrument MAUD. Experimental team V. Ryukhtin, A. Naberezhnov

The principle idea of measurements was to study of temperature evolution of internal organization of ferroelectric nanoparticles embedded into magnetic porous glasses near the ferroelectric phase transition at application of external magnetic fields.

We have used two types of nanocomposites (NCM) on base of microporous magnetic glasses Fe4-MIP with average pore diameter ~ 5 nm. The first type contained the sodium nitrite (NaNO2) where we have earlier observed the crossover [1] of the ferroelectric phase transition from the first order to the second one. The second nanocomposite contained the potassium nitrate (KNO3). In KNO3 the ferroelectric phase exists in the temperature interval 397 – 378 K at cooling only, but in a restricted geometry this phase becomes stable at cooling down to 100 K [2]. NaNO2 and KNO3 were introduced into the pores from the melt. In Figure the results of SANS data at 310 K (a) and 438 K (b) for NCM NaNO2+Fe4-MIP are presented.

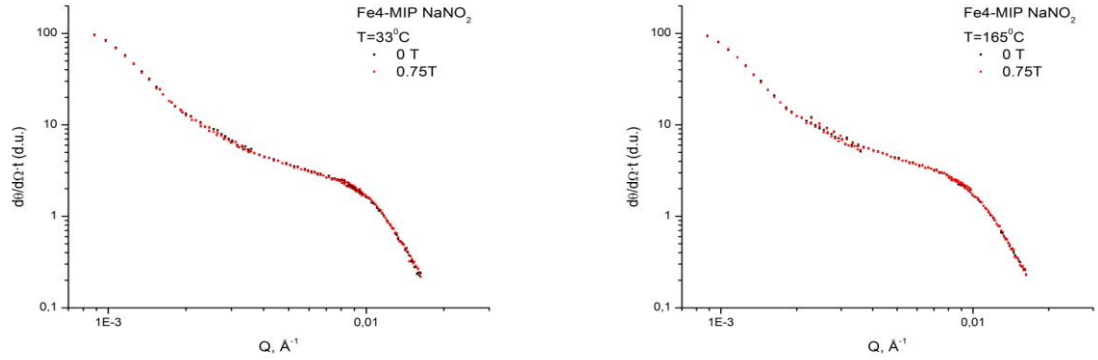


(a) (b)

***Figure*** *S(Q) for Fe4-MIP with NaNO2 embedded into the pores. Black points correspond to zero field, red points - at field 0.75 T.*

The anomalies at small Q and at Q~0.01 $Å^{-1}$ correspond to magnetic nanoparticles which we have earlier observed in our studies of empty microporous magnetic glasses. It is easy to see that there is no effect of applied magnetic field (up to B=0.75 T) on their space organization. It confirms our results devoted to study of magnetostriction in these glasses [3] where it have been shown that the magnetostriction has appeared at B above 1 T. Unfortunately we had no possibility to apply the field higher 1 T due to experimental restrictions. The scattering objects at Q~ $2\times10^{-3}$ $Å^{-1}$ correspond to the embedded ferroelectrics and demonstrate a weak dependence on temperature. The dependence on applied magnetic field for ferroelectric nanoparticles we could not observed due to insufficient magnetic field.

References

1 A. Naberezhnov, A. Fokin, Yu. Kumzerov , A. Sotnikov , S. Vakhrushev, and B. Dorner, "Structure and properties of confined sodium nitrite", ***Eur. Phys. J.*** **E 12**, s21-s24 (2003)

2 A. Naberezhnov, E. Koroleva, E. Rysiakiewicz-Pasek, A. Fokin, A. Sysoeva, A. Franz, M. Seregin and M. Tovar "Phase transitions in nanostructured potassium nitrate" ***Phase Transitions*** , 87, 1148-1156 (2014)

3 A. Naberezhnov, N. Porechnaya, V. Nizhankovskii, A. Filimonov, and B. Nacke "Morphology and Magnetic Properties of Ferriferous Two-Phase Sodium Borosilicate Glasses" ***The Scientific World Journal***, Volume 2014, Article ID 320451, 7 pages, (2014)

# Optical devices by focused MeV ions

Laboratory of Tandetron

István Rajta

Proposal ID

231

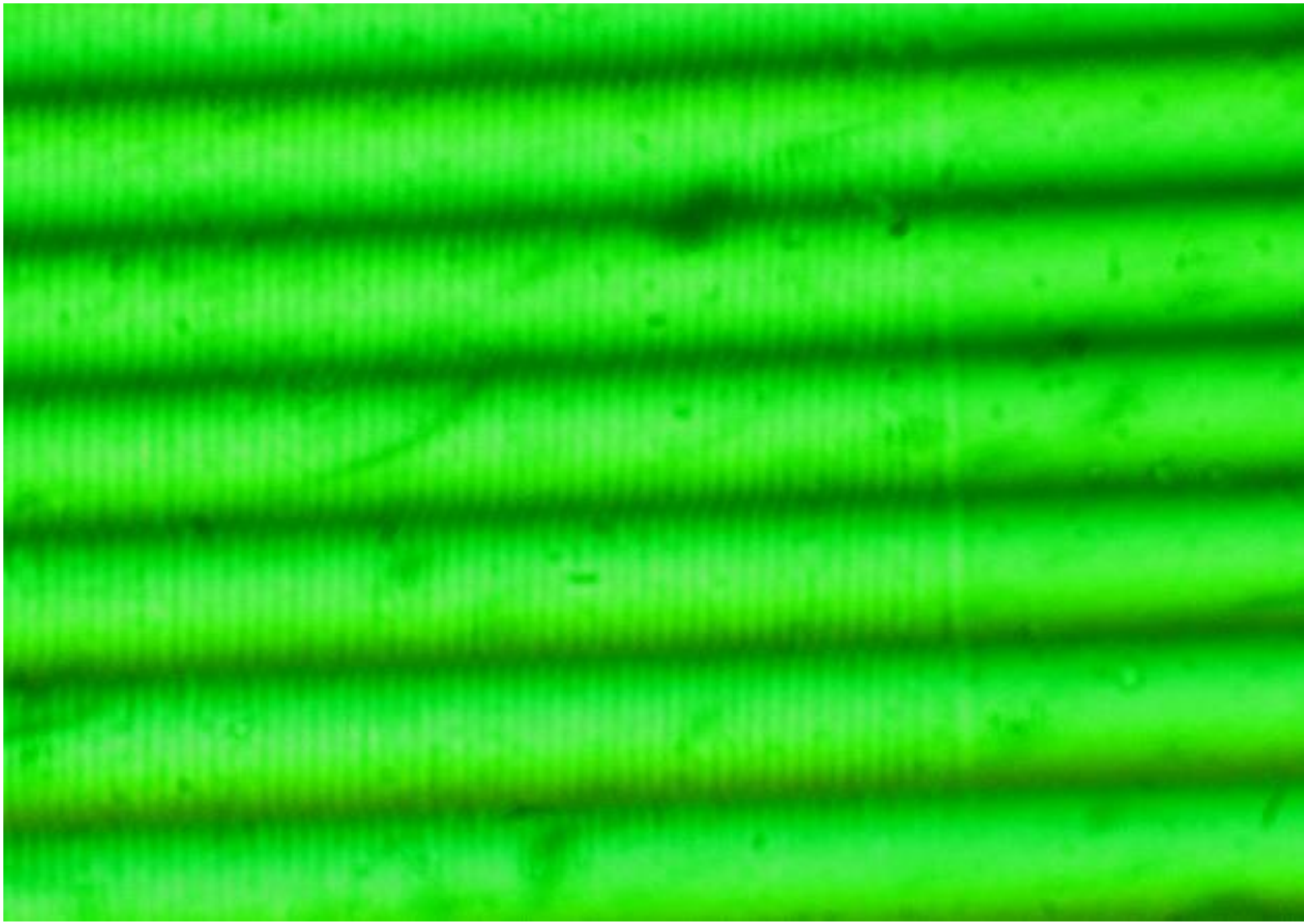

***Figure 1.*** *Transmission interference microscopic image of a grating with $\Lambda = 8\ \mu m$, written by a 5 MeV $N^{4+}$ microbeam at a fluence of $5 \times 10^{15}$ ions/cm$^2$ in an Er:$LiNbO_3$ crystal.*

# Depth analysis of nanostructured surfaces

Laboratory of Tandetron

Petr Slepika

Proposal ID

235

**Report regarding proposal: „Depth analysis of nanostructured surfaces“**

***P.Slepicka, V. Svorcik,*** *Department of Solid State Engineering, The University of Chemistry and Technology, Prague, Czech Republic*

High power plasma was successfully used as an efficient and inexpensive tool for polymethylpentene cytocompatibility enhancement. Proper surface roughness and morphology as well as the surface chemistry of a material are essential factors for successful utilization of a substrate intended for tissue engineering applications.

We applied oxygen and argon plasma treatments to activate the polymethylpentene (PMP) surface. We focused on investigation of the changed properties. The AFM and FIB-SEM study demonstrated that plasma treatments of PMP induced structured surfaces depending on the applied plasma setting. Measurement of the goniometry, chemical changes (functional groups by FTIR, element concentration by XPS and RBS/ERDA) was included. RBS method revealed the depth concentration profile of oxygen concentration and by ERDA, the depth concentration profile of hydrogen was measured. Plasma treatment takes place in the polymer surface layer, which corresponds to the plots, where the oxygen decreases towards the bulk, up to the depth of 150 nm, where no oxygen was detected. The results from XPS, RBS and ERDA analysis show the trends (the increase in oxygen or the decrease of hydrogen after the treatment) remain resembling.

Experiments on treated substrates with mouse fibroblasts NIH 3T3 has shown a significant increase in cell adhesion and proliferation on treated PMP substrates when compared to untreated polymer. This study demonstrates how to easily improve cytocompatibility of a very inert and resistant polymer for tissue engineering applications.

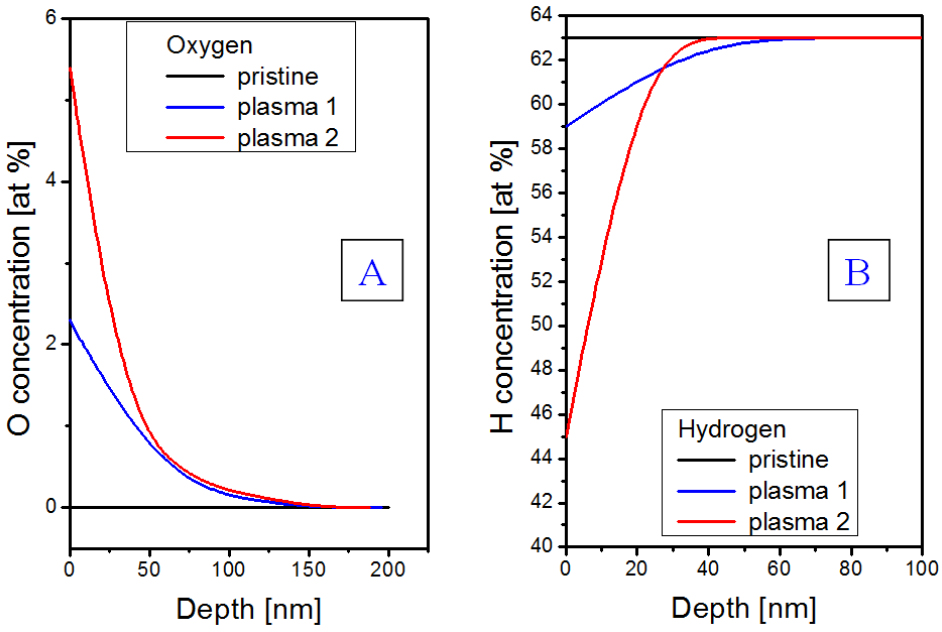


*Figure. Depth concentration profile of (A) oxygen measured using RBS and (B) hydrogen measured using ERDA for pristine PMP and samples treated by plasma (200 W, 240 s): 1 – in O2/Ar atmosphere and 2 – in Ar atmosphere.*

Paper:

I. Michaljaničová, et al., *High power plasma as an efficient tool for polymethylpentene cytocompatibility enhancement*, RSC Adv. 6 (2016) 76000–76010.

# direct observing lithium ion transfer during (dis)charging via neutron depth profiling

Neutron Physics Laboratory - Nuclear analytical methods with neutrons

Jie Xie

Proposal ID

242

In-Situ Detect of the Mobilization of Li Ions in All-Solid-State Lithium-Ion batteries

In all-solid-state Li-ions batteries, during charging, Li-ions migrate from cathode to anode (cathode will be delithiated and anode will be lithiated), and Li-ions will move in the contrary direction during discharging operation. The cross-section view of the measured microbattery is shown in Figure 1. In our case the current collector is Pt of about 800 nm, cathode is LiCoO2 about 8 µm, the electrolyte is Li3PO4 (3.6 µm) and Li (14 µm) is used as anode.

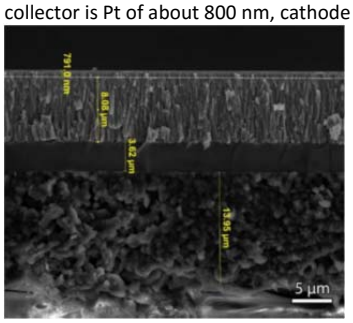


Figure 1. Cross-section view of microbattery.

The geometry of NDP setup is shown in Figure 2. The spectrum of the α particles suffers in the latter case from too high energy loss to determine an accurate profile, thus the spectra of triton will be used for analysis.

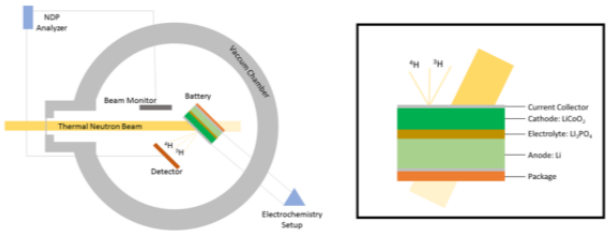


Figure 2. Schematic representation of the NDP set-up. The inset below shows the orientation of the battery inside the NDP measurement chamber.

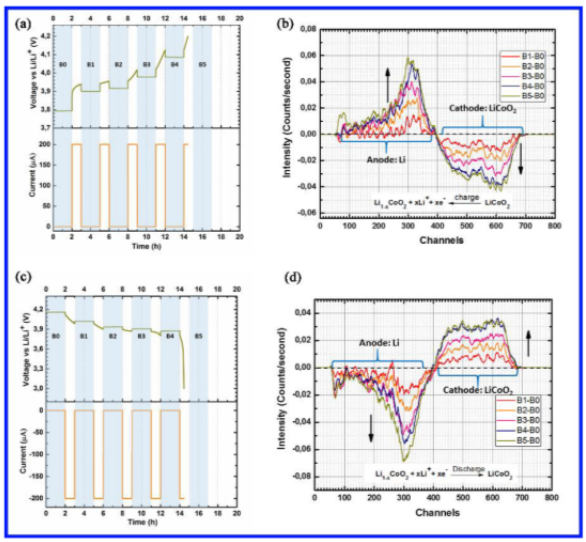


Figure 3. The charging at 0.2 mA (~0.2 C-rate) and NDP data collecting procedures (a), NDP spectra during charging (b), discharging at 0.2 mA (~0.2 C-rate) and NDP data collecting procedure (c), NDP spectra during discharging (d).

The charging/discharging electrochemical procedure is shown in Figure 3(a) and (c), in which B0, B1, B2, B3, B4 and B5 represents the neutron beam time for collecting the tritonsignal. Before the NDP measurement, the battery will be fully discharged, in this state the cathode is LiCoO2. It should be noted that during charging the cutoff voltage is set as 4.2 V to avoid overcharge, which means when the potential amounted to this value the charging process will stop. It is indicated in Figure 3(a) that in this recipe in the stage 0-2 h, the battery is full discharged and the NDP data collected during this time would be used as base spectrum (B0). After 1 h charge (current is selected as 0.2 mA, without NDP data collecting), the NDP spectrum, indicated as B1, would be collected again. To obtain obvious net intensity difference between each state-of-charge (SOC), the base spectrum (B0) would be subtracted from the 1 h charged spectrum (B1), indicated as B0-B1. In the similar way, B2-B0, B3-B0, B4-B0 and B5-B0 were obtained (Figure 3 (b)). It is indicated in the NDP spectra that, with the charging process moving on, the amount of Li-ions transferred from the cathode to the anode. It is clearly visible that the cathode (LiCoO2) profile is reduced in intensity while an intense narrow peak with an equal area appears at the anode (Li) side. After the charging process, the battery was in the fully charged state and the cathode was Li0.5CoO2, due to the delithiation of LiCoO2. After ~6 h rest, the discharging process followed (see Figure 3(c)). The NDP spectrum of the fully charged was collected for 2 h and was set as the base data B0. Similarly, the spectra (B1-B0, B2-B0, B3-B0, B4-B0 and B5-B0) of different SOC was obtained, displayed in Figure 3(d) .It is found that along with continuous discharging the lithium intensity in the cathode increased and that of the anode decreased.

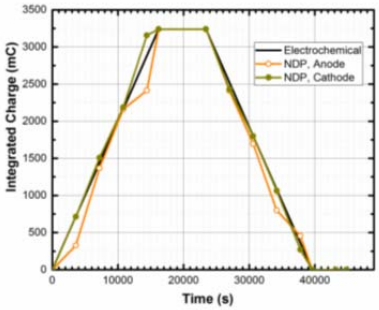


Figure 4. The lithium migration determined by in situ 3H NDP measurements for the cathode and the anode compared to the electrochemically integrated charge (b).

It is possible to in situ monitor the charge-discharge profile by integrating the difference between the continuously measured NDP spectra and the spectrum of the as-deposited (discharged) battery in the energy range of the cathode and the anode. The amount of lithium removed or stored on both sides can with this difference be determined accurately, even when the depth profile is relatively inaccurate. The NDP spectra areas at anode and cathode at different SOC are proximately proportional to the amount of changed Li-ions in electrodes. The results of this measurement are plotted in Figure 4 and show that the NDP results for both the anode and the cathode coincide closely with the electrochemical measurement. It can therefore be concluded that NDP is a technique that can follow lithium motion during charging/discharging of a thin-film battery with adequate accuracy.

Overall, it was shown that NDP is a valuable tool to reveal the processes occurring inside a thin-film solid-state battery during cycling in in-situ way.

# : Elemental characterization of environmental and botanical samples from Ethiopia by NAA Lab: Neutro

Neutron Physics Laboratory - Nuclear analytical methods with neutrons

teshager Aklie bitewlign

Proposal ID

243

**Multi-elemental analysis of environmental samples from Ethiopia using INAA** **Teshager Aklie**

In the region of Gondar, the residence of different areas suffered by different types of abnormalities or on adverse health effects. These health challenges have direct relation to essential and toxic elements. The aim of the experiment was to identify elemental contents with their amounts from the environmental samples. Types of the samples were geological (soil and coals), botanical (crops and medicinal plants) and liquid (drinking stream waters and industrial byproducts). Starting from the sample preparation the experiment was carried out in the Czech Republic, using LVR-15 research reactor at the CANAM infrastructure of NPICAS, Rez.

The coal samples were crushed by jaw crusher. The crushed coal, soil samples and crop samples were powdered to the 200mesh size and homogenized by ball mill and inserted into the oven to dry by 50 $^0$c for three days until their mass become constant. The liquid samples were acidified by 1ml nitric acid of 65% concentration for each 0.5l amount of water, in-order to precipitate trace elements absorbed by the wall of the container, which is to avoid loss of trace elements with the interaction of the wall of the polyethylene bottle. The liquid samples were filtered by a filter whose pores diameter is 0.6micro meter and centrifuged by digital centrifuge at 400 rpm angular speed for 5 minutes to separate the solid part from them. The liquid fraction was evaporated to dryness on a hotplate in a glass and Teflon beakers. The solid fraction was dried at 80 $^0$c.

The Standard reference materials (SRM), which were irradiated with the sub samples for verification and quality control, were prepared properly according to the following SRM of the National Institute of Standard Technology (NIST). NIST SRM 2711 (Montana soil) and 1633b (coal fly ash) were used for analysis of the geological samples and liquid samples where as NIST SRM1515 (Apple leaves) and 1547 (Peach leaves) were used for analysis of botanical samples. The LVR-15 experimental reactor of the research center, Rez was operated at a power of 9.7MW with providing $3.2x10^{13}xcm^{-2}s^{-1}$ neutron fluence rate for short thermal irradiation,$1.1x10^{13}cm^{-2}s^{-1}$ neutron fluence rate for short epithermal and fast irradiation and $3.6x10^{13}cm^{-2}s^{-1}$ fluence rate for long thermal irradiation. The procedure used from irradiation up to analyzing with the counting system are summarized through the following tables

*Tab. 1 HPGe detectors used for counting of irradiated samples*

| Lable | Type | Relative efficiency | Resolution FWHM | Active area | Window material |
|---|---|---|---|---|---|
| CAN | Coaxial | 78% | 1.9 Kev* | - | - |
| ORT | Coaxial | 53% | 1.8 Kev* | - | - |
| PGT | Coxial | 21% | 1.8 Kev+ | - | - |
| PLANAR | Planar | - | 0.52 Kev+ | 500 sq mm | Be |
| PLANAR-R | Planar | - | 0.53 Kev+ | 500 sq mm | Be |

** for 1.33 Mev gamma-line of Co-60 + for 122 Kev gamma-line of Co-57*

Table-2 *Mode of irradiation with values of irradiation time, decay time, counting time and type of detectors with the distance between the detector and irradiated samples*

| Samples | Geological samples | | | | | Botanical samples | | | | Liquid samples | | | | |
|---|---|---|---|---|---|---|---|---|---|---|---|---|---|---|
| Irradiation mode | S | E | | L | | S | E | L | | S | E | | L | |
| $t_{ir}$ | 0.5min | 0.75min | | 2hrs | | 1min | 0.75min | 2hrs | | 1min | 0.75min | | 2hrs | |
| $t_{dec}$ | 13min | 10min | 22min | 5d | 30d | 10min | 8min | 4-7d | 30d | 13min | 10min | 22min | 4-7d | 35d |
| $t_{cnt}$ | 13min | 10min | 20min | 25min | 3hrs | 10min | 15min | 25min | 3hrs | 13min | 10min | 20min | 25min | 3hrs |
| Detector | PGT | PGT | Planar R | CAN | CAN | PGT | Planar | CAN | ORT | PGT | PGT | Planar R | CAN | ORT |
| geometry | 15cm | 3cm | 2cm | 20cm | 5cm | 5cm | 2cm | 7cm | 1cm | 15cm | 3cm | 2cm | 7cm | 1cm |

*S=short TINAA, E=EINAA, L = long INAA, $t_{ir}$ = irradiation time, $t_{dec}$ = decay time, $t_{cnt}$ = counting time*

In this study forty-eight elements in the geological samples, forty-six elements from botanical samples and forty-five elements from liquid sample were identified, including the essential elements K, Mg, Ca , Cl, Fe, I, Co, Mn, Cr ,Cu, Se, Zn, Ni and potentially toxic elements Al, As, Au, Ba, Br, Cd, Cs, Rb, Sb, Sc, Si, Sm, Sr, La, Ti, W, V. In the soil samples the amounts of the most macro and micro nutrients are above from their worldwide mea values and the coals are rich in the amounts of the rare earth elements.

# Residual stress determination by neutron diffraction in low-carbon steel wires with accumulated shea

Neutron Physics Laboratory - Neutron diffraction

Massimo Rogante

Proposal ID

244

**CANAM_244 Report Form**

# Residual stress determination by neutron diffraction in low-carbon steel wires with accumulated shear deformation

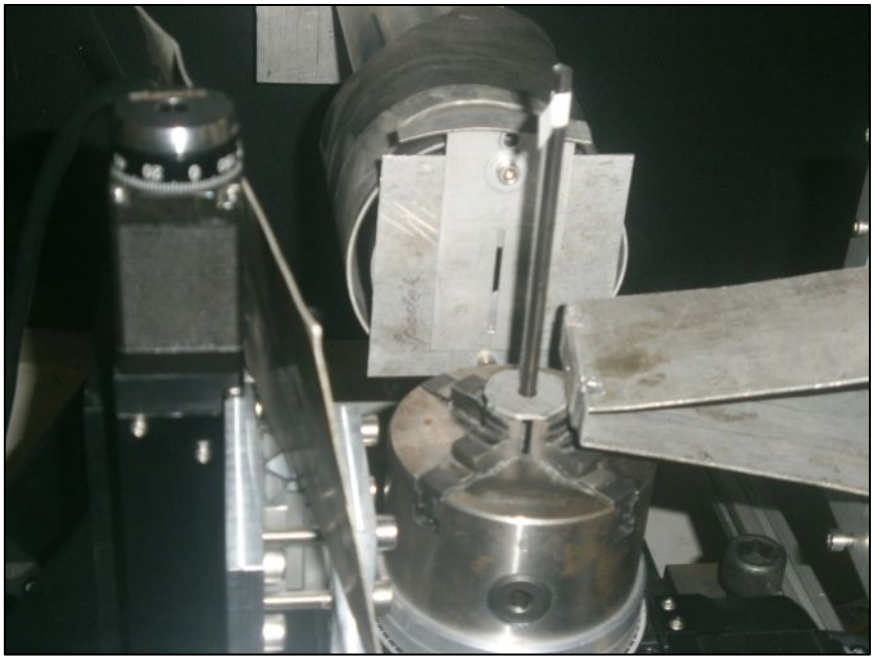

Fig. 1

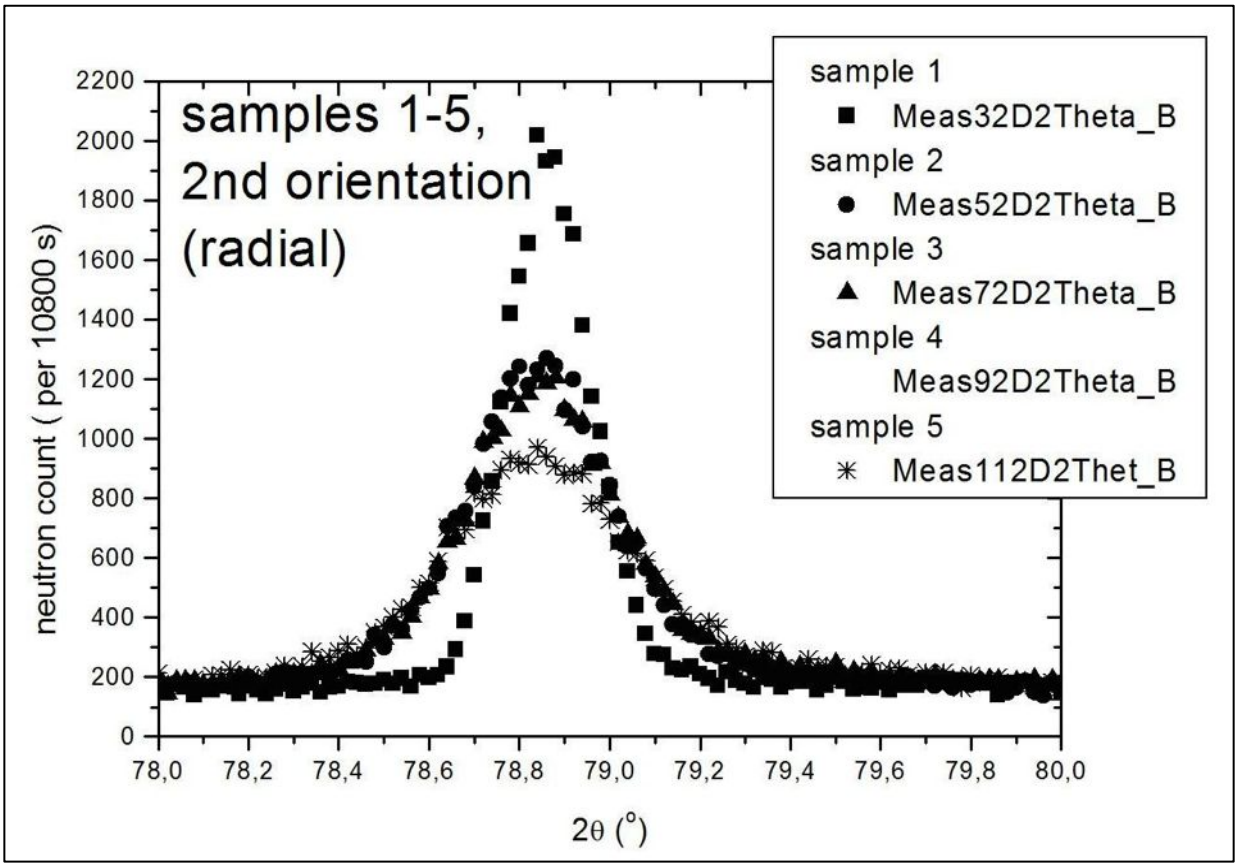


Fig. 2

# Investigation of novel composite CoNiAl-Ti by neutron diffraction and small-angle neutron scattering

Neutron Physics Laboratory - Neutron diffraction

Pavel Strunz

Proposal ID

245

Report regarding proposal "**Investigation of novel composite CoNiAl-Ti by neutron diffraction**"

Pavel Strunz (email: strunz@ujf.cas.cz, affiliation: Ústav jaderné fyziky AV ČR, v. v. i.),
**P. Beran**, NPI, Oleg Heczko, IP Prague, CZ, Jaromír Kopeček, IP Prague, CZ, Tomáš Chráska, Institute of Plasma Physics, CZ, Radek Mušálek, Institute of Plasma Physics, CZ, Zdenek Pala, Institute of Plasma Physics, CZ, Josef Stráský, MFF UK Prague, CZ,

Investigation of phase composition and microstructure of composite material CoNiAl-Ti produced by Spark Plasma Sintering was proposed. The properties of the composite are expected to depend strongly on minority phase content and thus on the parameters of preparation of the material. The results complement characterization by other techniques, predominantly electron microscopy and XRD.

Measured samples of CoNiAl plus Ti prepared by SPS:

| Sample | T, C | P, Mpa | time,min | CoNiAl:Ti | Ti, % |
|---|---|---|---|---|---|
| 150713_2 | 911 | 5 | 0 | 1:1 | 50 |
| 150715_1 | 950 | 80 | 1 | 1:1 | 50 |
| 150714_1 | 950 | 80 | 5 | 1:1 | 50 |
| 150909_1 | 950 | 80 | 5 | 2:1 | 33.3 |
| 150915_1 | 950 | 80 | 1 | 2:1 | 33.3 |
| 150916_1 | 950 | 80 | 1 | 1:2 | 66.7 |
| 150916_2 | 950 | 80 | 5 | 1:2 | 66.7 |

An example of measured and evaluated neutron diffraction profile:

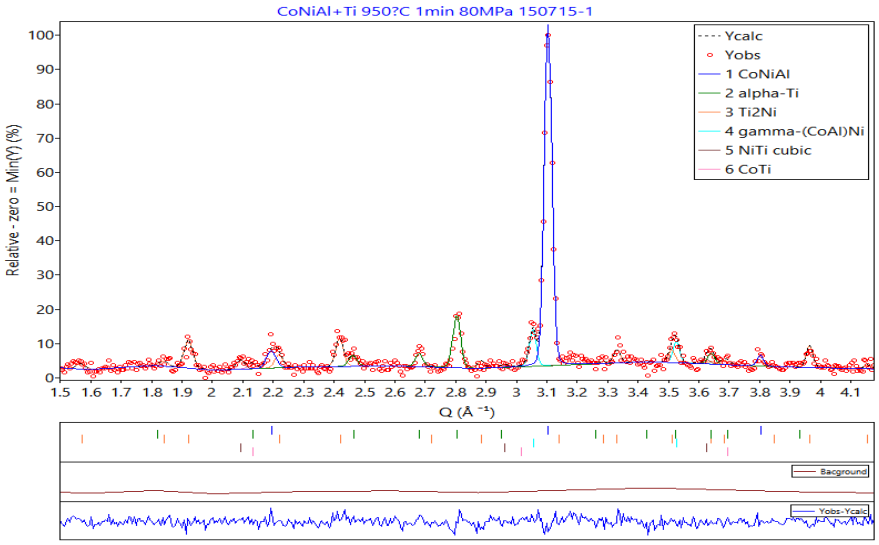


Dependence of phase content
on the mode of sample preparation

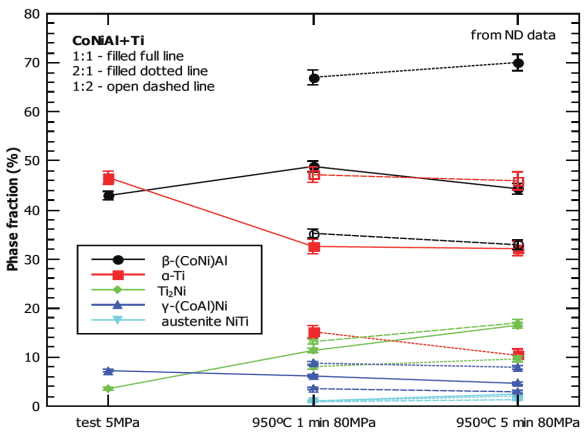


… and on the amount of Ti in the sample:

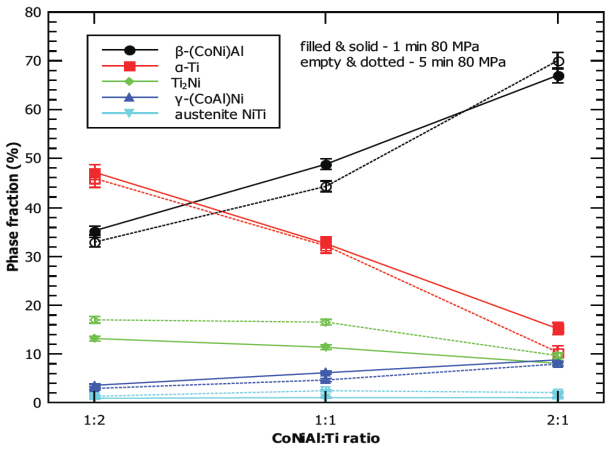

# Investigation of novel composite CoNiAl-Ti by small-angle neutron scattering and neutron diffraction

Neutron Physics Laboratory - Neutron diffraction

Pavel Strunz

Proposal ID

246

Report regarding proposal "**Investigation of novel composite CoNiAl-Ti by small-angle neutron scattering and neutron diffraction**"

Pavel Strunz (email: strunz@ujf.cas.cz, affiliation: Ústav jaderné fyziky AV ČR, v. v. i.),
V. Ryukhtin, Oleg Heczko, IP Prague, CZ, Jaromír Kopeček, IP Prague, CZ, Tomáš Chráska, Institute of Plasma Physics, CZ, Radek Mušálek, Institute of Plasma Physics, CZ, Zdenek Pala, Institute of Plasma Physics, CZ, Josef Stráský, MFF UK Prague, CZ,

Investigation of phase composition and microstructure of composite material CoNiAl-Ti produced by Spark Plasma Sintering was proposed. The properties of the composite are expected to depend strongly on minority phase content and thus on the parameters of preparation of the material. The results complement characterization by other techniques, predominantly electron microscopy and XRD.

Measured samples

| Sample | T, C | P, Mpa | time,min | CoNiAl:Ti | Ti, % | <R>, nm | dR |
|---|---|---|---|---|---|---|---|
| 150713_2 | 911 | 5 | 0 | 1:1 | 50 | 55.25 | 0.69 |
| 150715_1 | 950 | 80 | 1 | 1:1 | 50 | 70.39 | 1.2 |
| 150714_1 | 950 | 80 | 5 | 1:1 | 50 | 75.73 | 2.1 |
| 150909_1 | 950 | 80 | 5 | 2:1 | 33.3 | 103.9 | 3 |
| 150915_1 | 950 | 80 | 1 | 2:1 | 33.3 | 86.1 | 1.2 |
| 150916_1 | 950 | 80 | 1 | 1:2 | 66.7 | 82.17 | 1.1 |
| 150916_2 | 950 | 80 | 5 | 1:2 | 66.7 | 69.26 | 1.5 |

Comparison of SANS between pure CoNiAl and with Ti

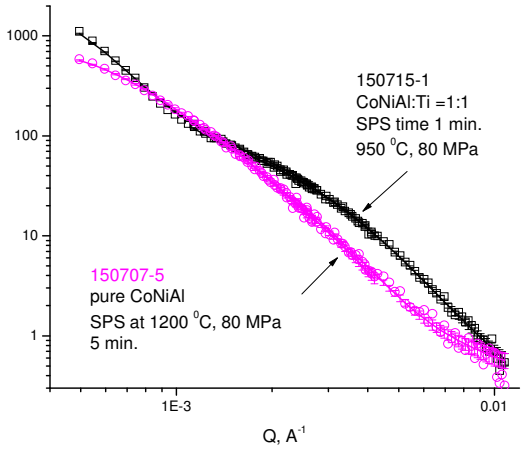


Exmple of SANS from CoNiAl+Ti samples:

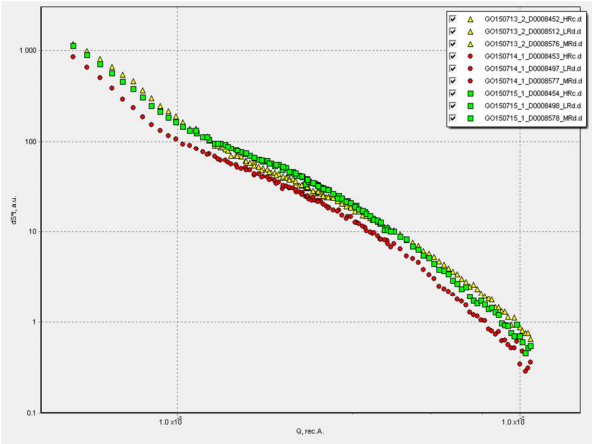

Probable cause of scattering: nanopores. Then, their volume fraction and mean size change according to the following figures:

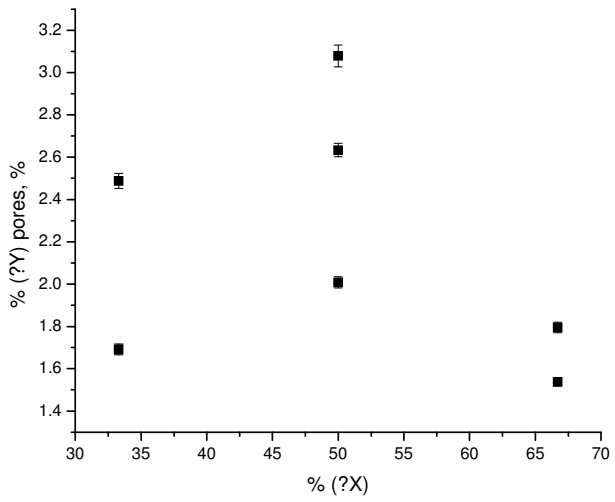


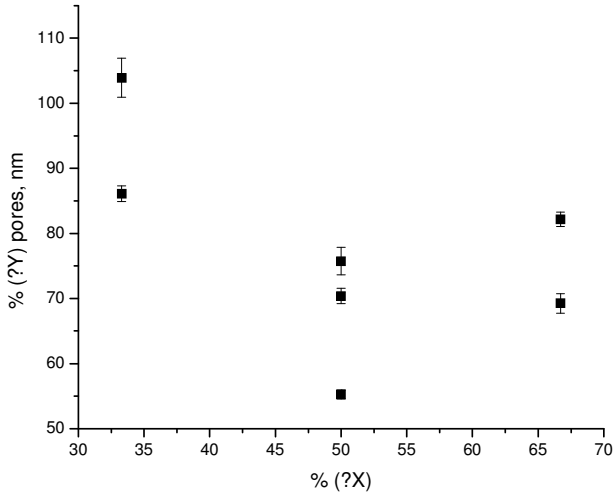

# Microstructural investigations of BaTiO3-based ceramics prepared by Sparc Plasma Sintering (AdMat)

Neutron Physics Laboratory - Neutron diffraction

Vasyl Ryukhtin

Proposal ID

249

# Microstructural investigations of BaTiO3-based ceramics prepared by Sparc Plasma Sintering (SPS)

Vasyl Ryukhtin, Nuclear Physics Institute NPI (ASCR), Neutron Physics Department

Pavel Ctibor, Institute of Plasma Physics, Prague Czech Republic

A set of BaTiO3-based samples were sintered by SPS at Institute of Plasma Physics (IPP) of ASCR. Spark plasma sintering enables very rapid fabrication of bulk ceramic materials. It is an emerging consolidation technique, which combines pulsed electric currents and uniaxial pressure induced compaction. Heating rates, applied pressures and pulsed current patterns are the main factors responsible for the enhancement of densification kinetics and conservation of the submicron-scale structure of the materials [1]. This material was widely studied at material engineering (ME) department of IPP ASCR as excellent material for plasma spraying (PS).

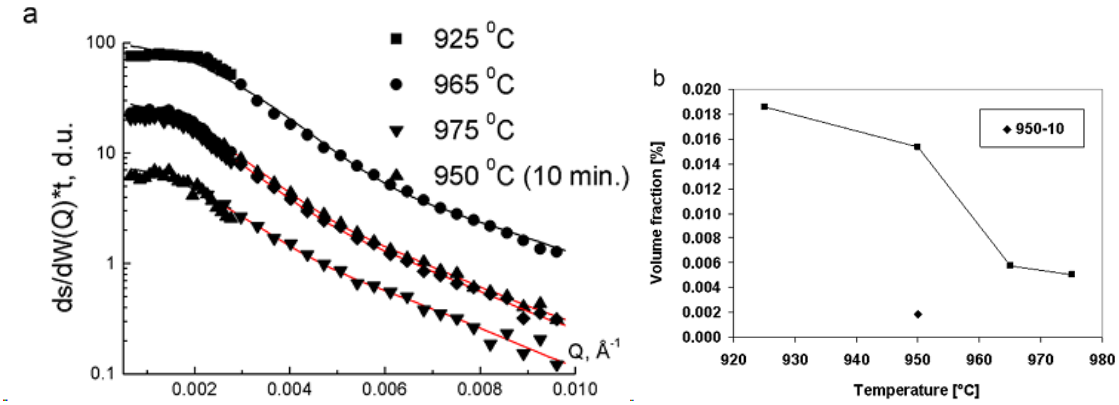


Fig. 1. SANS scattering spectra (a) and fitted volume fractions of pores (b).

The SANS curves were fitted using simple structural model of spherical particles (Fig. 1a) with help of SASprofit software. Although, for some samples scattering data in low angle region were distorted by multiple scattering a part of spectra with high angles were fitted reasonably good. However, because of the multiple scattering, a pore size distribution cannot be specified and only the volume fraction V is representative (Fig. 1b). The results include all pores between 20 nm and 3 mm. Certain trend could be seen (Fig. 1b) – the higher is the sintering temperature, the lower is the porosity. Increasing the dwell time at 950 °C led to further decrease in the porosity volume fraction. For the sample 950-10 the volume fraction is nearly 10 times smaller compare to the most porous sample 925.

**Reference**

[1] P. Ctibor et al, *Barium titanate nanometric polycrystalline ceramics fired by spark plasma sintering* Ceramics International 42 (2016) 15989–15993.

# Characterization of RS Distribution in Thick Welded Sheets after MAG and LASER Welding

Neutron Physics Laboratory - Neutron diffraction

Kamil Kolarik

Proposal ID

251

**Report regarding proposal "Characterization of RS Distribution in Thick Welded Sheets after MAG and LASER Welding"**

K. Trojan [1,a], Ch. Hervoches [2], K. Kolařík [1], N. Ganev [1], P. Mikula [2], J. Čapek [1]

[1] CTU in Prague, Department of Solid State Engineering, Faculty of Nuclear Sciences and Physical Engineering, Trojanova 13, 120 00 Prague 2, Czech Republic
[2] Nuclear Physics Institute, ASCR, v.v.i., Department of Neutron Physics, 25068 Řež, Czech Republic
[a] trojaka2@fjfi.cvut.cz

It was found from the measured residual stresses (RS) by neutron diffraction in three different sample's orientations and in three different depths under the surface (see Fig. 1) that the greatest gradient of residual stresses is in the direction parallel to the weld (L – longitudinal direction) for both the laser and the MAG welds. According to the literature study (for example [1]) and our results, greater tensile RS exhibits the laser weld in almost all measured lines. Furthermore, the results describing width of the heat affected zone (changes in values of RS and full widths of the measured diffraction lines at half of the maximum) are very similar for both the analytical methods (XRD and neutron diffraction).

The resulting RS distributions obtained by using both the methods with a different approach are in certain correlation. Each method describes the outcome of RS in different context. The redistribution of RS during the cutting has not yet been accurately described, so further measurements and verification using mathematical modelling will be needed.

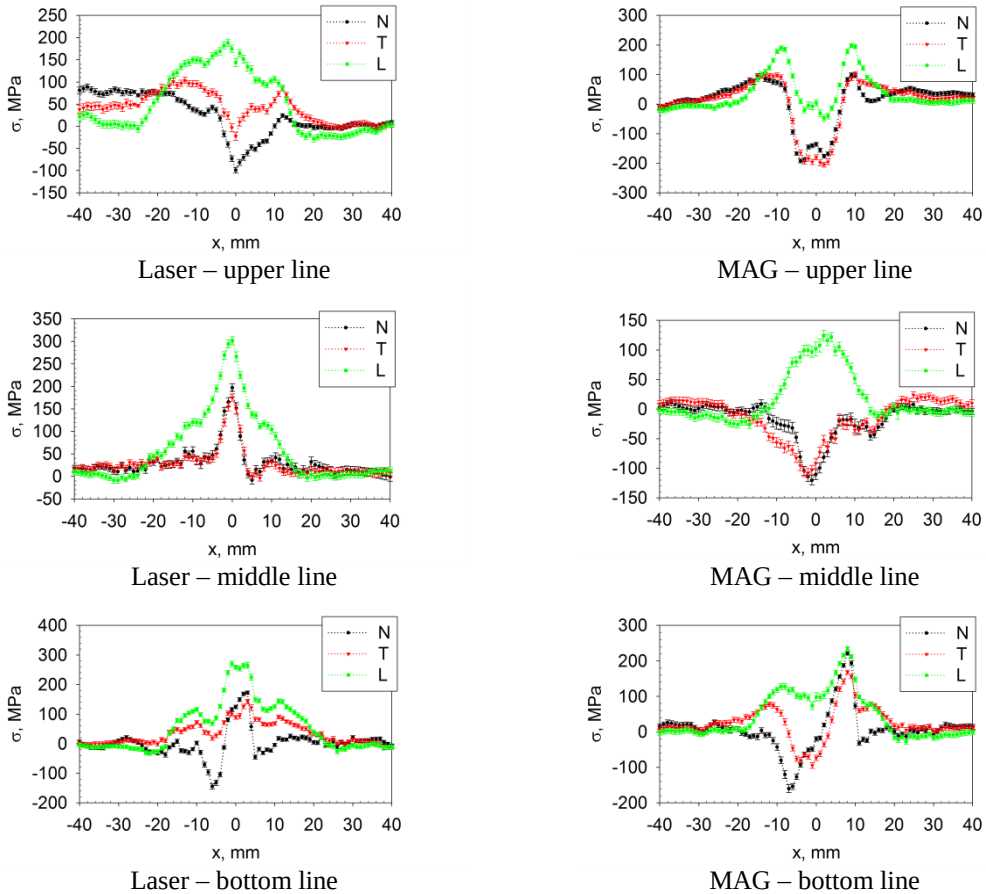


Laser – upper line | MAG – upper line

Laser – middle line | MAG – middle line

Laser – bottom line | MAG – bottom line

Fig. 1: RS for laser and MAG sample along three measured lines obtained by neutron diffraction.

## Reference

[1] T. Nitschke-Pagel, K. Digler. Sources and Consequences of Residual Stresses due to Welding, *Materials science forum*: 2777-2785, 2014.

# SANS characterization of Polymer Cement Concretes with added  Al2O3 and redispersible dry polymers

Neutron Physics Laboratory - Neutron diffraction

Massimo Rogante

Proposal ID

254

**Report regarding the proposal "SANS characterization of Polymer Cement Concretes with added γ Al2O3 and redispersible dry polymers"**

**Proposer:** M. Rogante, Rogante Engineering Office, Italy
**Experimental team:** M. Rogante, V. Ryukhtin

Twelve Polymer Cement Concretes (PCC) samples (CEM00 ÷ CEM11), made of Portland cement with added γAl2O3 and redispersible dry polymers with different additives ratios, have been investigated by SANS by using the MAUD instrument within CANAM experiment 254. Measured scattering functions show power low angle dependence over the whole Q-range of the setup ($2 \cdot 10^{-4}$ Å$^{-1}$ ÷ $2 \cdot 10^{-2}$ Å$^{-1}$) (see Fig. 1). This behaviour well correlates with conventional SANS data [1]. Power law scattering with non-integer exponent can be evidence of self similar fractal microstructure of porosity in this material. Moreover, power exponent is close to 2 in slit smeared geometry of small-angle scattering from sedimentary rocks [2]. It says about similarity in microstructures of the cements and sedimentary rocks.

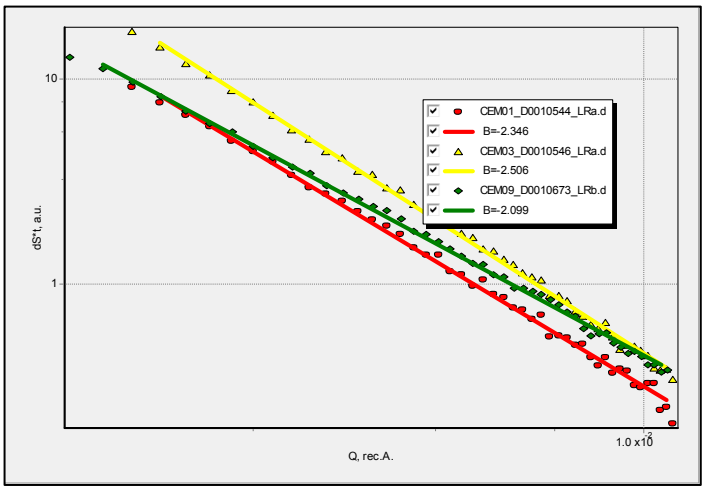


Fig. 1. Example of measured SANS functions for 3 samples with fitted power law model.

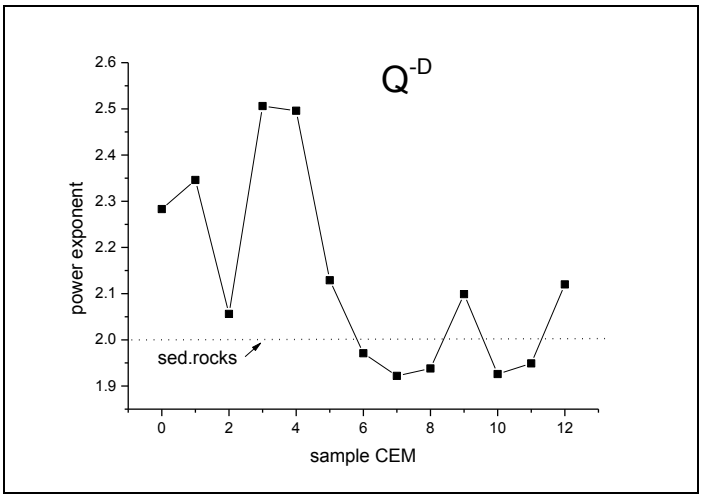


Fig. 2. Power exponent as dependent on sample.

Most of the investigated samples (CEM02, CEM05 - CEM12) have power exponent as sedimentary rocks (see Fig. 2). However, several samples (CEM00, CEM01, CEM03, CEM04) scatter with higher slope in log-log scale, which may mean that structure is more dense and compact in this size range.

[1] M. Rogante et al., Science and Engineering of Composite Materials (2015), ISSN (Online) 2191-0359, DOI: 10.1515/secm-2015-0013.

[2] Radlinski, A.P.: Small-angle neutron scattering and the microstructure of rocks. Rev. Miner. Geochem. 63, 363 (2006)

# Proton beam lithography to fabricate micro-patterns

Laboratory of Tandetron

Mariapompea Cutroneo

Proposal ID

256

**Ion Micro Beam, promising methods for interdisciplinary Research**

**M. Cutroneo, V. Havranek, L. Torrisi and B. Svecova**

The proton beam is an attractive technique for direct-writing high aspect ratio structure for wide types of materials (insulators, semiconductors and metals) as well as for many applications such as microfluidics, bioscience and miniaturized sensors. Energetic proton beam penetrating the resist with the characteristic straight trajectory, deposits energy and creates damage along the ion trajectory (Fig.1). The velocity of the energetic particles slows down due to the increase of the interaction cross-section with the surrounding atoms and just before they come to rest, in the energy loss a Bragg peak occurs, at which the nuclear energy loss assumes the maximum value. We exploited this effect to fabricate our cavities, taking into account the resist characteristics like sensitivity, contrast and nature of the resist. The involved material usually used are PMMA (positive resist) and SU-8 (epoxy-type negative resist). Polymethylmethacrylate (PMMA) is a resist material with optical clarity, low attenuation and interesting weathering used in PBW to create microstructures such as waveguides, polymeric structuration of microcavities, waveguides fabrication concerning photolithography and ion implantation.

The primary p-beam induces secondary electrons (delta rays) with low energy that generate main chain-scission in PMMA or crosslinking in SU-8 material. In this way, a suitable developer has been chosen to dissolve the damaged area.

At the Tandetron Lab (TL) of CANAM infrastructure of the NPI ASCR, Rez in the Czech Republic a Tandem accelerator delivered a proton beam between of 2.0 MeV. The spot size was 1.4 $\mu m^2$ in diameter and the delivered beam current was 8 pA. PMMA foils, 9 μm thick, were irradiated with the following proton fluences: 3.1 $x10^{13}$ ions·$cm^{-2}$ (50 nC /$mm^2$), 6.2 x $10^{13}$ ions·$cm^{-2}$ (100 nC/$mm^2$), 1.2 x $10^{14}$ ions·$cm^{-2}$ (190 nC/$mm^2$) and 1.8 x $10^{14}$ ions·$cm^{-2}$ (280 nC/$mm^2$). These low fluences have been chosen to prevent cross-linking occurring at higher fluences and taking into account the important control and role played by the low fluences in proton beam writing.

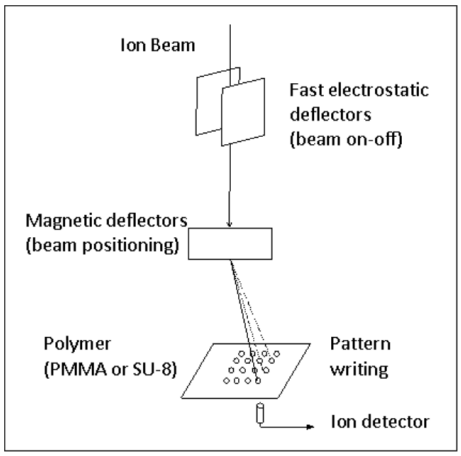


Fig.1 The proton beam writing system

The patterns written in 9 μm thick PMMA irradiated using a scan size of 25 μm x 25 μm and fluence of 3.1x $10^{13}$ ions/$cm^2$ were not fully exposed and the PMMA was incompletely removed in depth direction, as showed in figure 2.

To evaluate the quality of the produced microstructures, STIM analysis has been performed using a 0.6 μm x 0.6 μm of beam spot size, 500 μm x 500 μm and 10 μm x 10 μm of scan size, 0.2 μm of resolution, and 1000 protons $s^{-1}$ of beam current. The primary beam before and after every set of measures and each time was found to be 10 keV for 2.0 MeV of protons, confirming the negligibility of the degradation of the energy resolution.

The STIM images present the two dimensional scansions indicating the shape of the produced holes at different depth written in the PMMA foil.

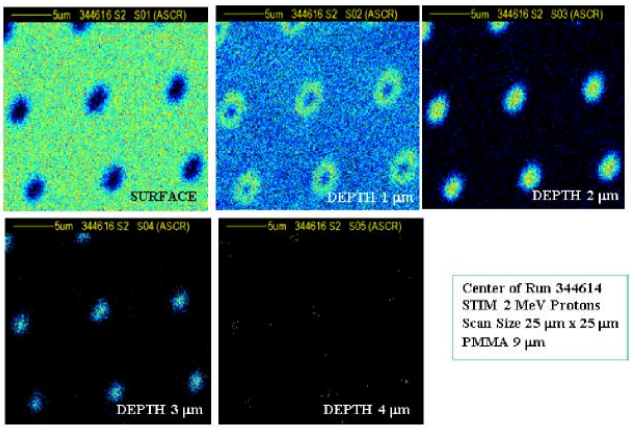


Fig.2 STIM image for PMMA foil 9 microns thick patterned at low fluence as a function of the depth, from surface (first image) up to 4 microns ( last image).

In the next work we plan to make a selection of patterns different in shapes and dimension written in PMMA ( different in thickness) using the proton beam writing and then, to evaluate the optical, structural and morphological properties to enhance their absorbance and make of them suitable to be laser irradiated. The obtained microstructures find many interesting applications in different scientific fields. One of this concerns the use of the PMMA foils as biocompatible microfilters, useful to filter biological liquids inside the human body organs, or to realize filters to collect pollutants for measurements of environmental contamination. Another consists in the realization of thin targets to be irradiated by laser in order to generate plasma with peculiar properties. In this case the micrometric patterns can be employed to withhold metallic nanoparticles and nano-aggregated promoting high laser absorption useful to generate plasmas with high temperature and electronic density.

**[1] M. Cutroneo, V. Havránek, L. Torrisi, B. Švecová,** Ion Micro Beam, promising methods for interdisciplinary research. Journal of Instrumentation. 11 (2016) C05001 Full text was for disposal in May 2016.

# Comparison between ion implantation by using laser and traditional accelerator

Laboratory of Tandetron

Mariapompea Cutroneo

Proposal ID

257

**Multi-energy ion implantation from high-intensity laser**
**M. Cutroneo, L. Torrisi, J. Ullschmied, R. Dudzak**

The dominant regime in most of experiments on ion acceleration from solid targets is the target normal sheath acceleration (TNSA). It is used in laser-matter interaction for laser intensities ranging approximately between $10^{16}$ and $10^{22}$ W/cm$^2$ as reported in several publications. Several models and scaling laws have been suggested to predict the maximum ion energy of accelerated ions in the TNSA regime on the basis of the laser and target parameters. A recent study showed the significant acceleration effect observed at laser intensities of the order of $10^{16}$ W/cm$^2$. Experimental detection of ions with energy higher than 4 MeV/charge state as well as the generation of multi-MeV electrons and of intense UV and X-ray emission are referred to the TNSA regime applied to thin foils. In the discussed experiment an iodine high-intensity laser at the Prague Asterix Laser System (PALS) was employed with an intensity of about $10^{16}$W cm$^{-2}$ to irradiate a gold (Au) foil 10 microns thick to generate a plasma of multienergy and multispecies ion. Many substrates, constituted by pure monocrystals of Si wafers, were exposed to the laser-generated plasma emitted in the forward direction.
The extracted ions are multi-energy and multi-species with Boltzmann-like distributions and are shifted towards high energies by increasing the ion charge state, according to the literature. The use of repetitive laser pulses, i.e. of repetitive laser-inducing implantations, makes it possible to increase and control the total implanted ion dose.
All accelerated ions are implanted in the substrate surfaces. The maximum kinetic energy is 1.04, 6.7 and 52.4 MeV for protons, carbon and Au ions, respectively. This result indicates an ion acceleration of about 1 MeV per charge state and also demonstrates that C ions are full ionized and that the Au ions have a maximum charge state of about 52+. Due to the ionization potential of Au52+ of 5.01 keV, the expected plasma electron temperature is of the same order of magnitude. Protons, carbon and Au ions are thus implanted at different depths based on their Boltzmann energy distribution and ion charge state distribution (Fig.1).

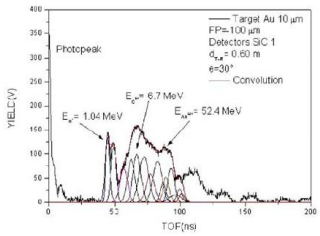


Fig.1 SiC spectrum of plasma emission in the forward direction, as measured using 10 micron Au foil and ion deconvolution using Coulomb-Boltzmann-shifted distribution.

The range of 1 MeV protons, 6 MeV C ions and 70 MeV Au ions in Si is 16.3 $\mu$m, 5.9 $\mu$m and 575 nm, respectively. In order to increase the implanted dose, 12 laser shots have been employed under the same experimental conditions. A typical RBS spectrum carried out on a Si substrate with gold ions implanted provides a maximum concentration, of about 100%, measured in the first surface layers with a thickness of about 50 nm, indicating that a thin fi lm of gold is deposited due to neutral atoms and very low energetic ions emitted from plasma. RBS shows that the concentration of the Au at 100 nm depth in silicon is of the order of 40 atm%; at 200 nm, the value falls to 20% and at 500 nm, the implantation is below 10% decreasing at about 0.05 atm% at about 1 micron depth, confirming the implantation of Au ion occurred at high energy but at low concentration. The maximum energy of the Au ions is 4.5 MeV; in fact, this beam has a range of 1 micron in silicon, as calculable using SRIM code of Ziegler. The limited energy of implanted ions is due to the Si exposition at 30° and not at 0° at which the maximum acceleration occurs. The integral amount of the implanted Au $2.08 \times 10^{15}$ atoms per cm$^2$. During the free expansion in vacuum of laser-generated plasma, the emitted ions are accelerated and their current signal was measured by SiC detectors in time of flight (TOF) configuration.
AFM analysis of the irradiated substrates has shown the presence of nanostructures on their surfaces. Owing to Au and Si nucleation, these structures can be induced by the high ion stopping power in the surface layers. High stopping powers are obtained for nuclear interactions, such as those produced by relatively low-energy Au ions implanted in the Si. For example Au ions at 25 keV, 100 keV, 1 MeV and 10 MeV have a nuclear stopping powers in Si corresponding to 1.89 MeV $\mu$m−1, 2.73 MeV $\mu$m−1, 2.92 MeV $\mu$m−1 and 1.20 MeV $\mu$m−1, respectively. Figure 2 shows two typical AFM images, providing a comparison between the substrate surface before the ion implantation (figure 2 (a)) and after the ion implantation (figure 2(b)) process using 12 laser shots to enhance the deposited ion dose. The achieved results are representative of the entire nanostructure surface because areas of first 20 $\mu$m × 20 $\mu$m, then of 1 $\mu$m × 1 $\mu$m, were investigated. The monocrystal Si substrate has a roughness too low to be highly polished, while the ion implanted surface shows an average roughness of the order of 30 nm. A strong difference is evident due to the increment of roughness and the formation of many sound drops. The whole of the implanted substrate area, which is of the order of 1 cm$^2$, shows the presence of such nanostructures. They have dimensions ranging mainly between 2 and 25 nm.

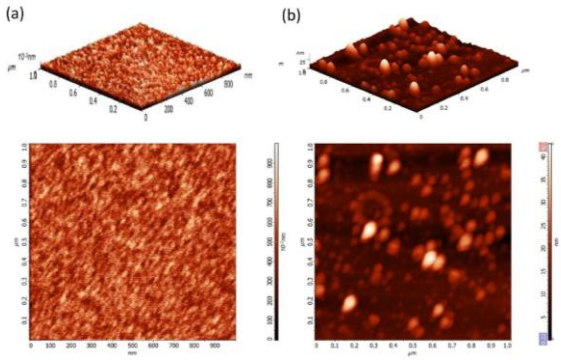


Fig. 2 A comparison of AFM images sized 1 μm x 1 μm, relative to the Si substrate surface before the plasma ion implantation a) and after the plasma ion implantation obtained using 12 laser shots irradiating an Au thin foil b).

AFM, in agreement with RBS analysis, indicates that structures are also present in the surface at a depth of the order of 40 nm. This is caused by the Au ion energy distribution, showing a contribution at low ion energy that produces Au deposition in the first surface layers of the substrate. that structures are also present in the surface at a depth.

[1] M. Cutroneo, L. Torrisi,J. Ullschmied, R. Dudžák, Multi-energy ion implantation from high-intensity laser, Nukleonika, **61** (2) (2016) 109-113.
[2] L. Torrisi, M. Cutroneo, A. Macková, V. Lavrentiev, M. Pfeifer, E. Krouský, An unconventional ion implantation method for producing Au and Si nanostructures using intense laser-generated plasmas, *Plasma Physics and Controlled Fusion*, **58** (2) (2016) 025011

# New understanding of the atomic structure and nonstoichiometry of Sc-doped TiO2 photocatalystst

Neutron Physics Laboratory - Neutron diffraction

Snejana BAKARDJIEVA

Proposal ID

260

# New understanding of the atomic structure and nonstoichiometry of Sc-doped $TiO_2$ photocatalysts with core-shell geometry by using neutron diffraction technique

Snejana Bakardjieva[1], Premysl Beran[2], Petr Bezdicka[1], Pavel Strunz[2], Robert Klie[3], Victor Zenou[4]

[1] Institute of Inorganic Chemistry AS CR, 25068 Rez, Czech Republic
[2] Nuclear Physics Institute AS CR, 25068 Rez, Czech Republic
[3] University of Illinois at Chicago, 1740 W Taylor St, Chicago 60612, USA
[4] Nuclear Research Center - Negev, P.O. Box 9001, 84190, Beer-Sheva, Israel

The nano-size powdered sample of Sc-doped $TiO_2$ annealed at 200, 400, 600 and 800°C was studied on MEREDIT diffractometer with the wavelength of 1.46 Å. The amount of Sc dopant estimated by STEM/EDS methods was pointed out 4.18 at.%. The neutron diffraction (ND) and X-ray powder diffraction (XRD) patterns were exanimated with the Rietveld profile method using both FULLPROF and GSAS programs. The refinements were allowed to vary Sc atom occupation on the possible Ti sites in anatase $TiO_2$ crystal lattice. The refined atomic coordinates over the whole temperature range were used to calculate the M-O-M bond distances and angles. It was found that Sc doping process led to non-stoichiometric material with a few percent of oxygen vacancies and $Ti^{3+}$ species. The best photocatalytical properties in degradation of 4-cholorophenol shown sample annealed at 600°C. This results could be explain on the basis of the unique structure arose after introducing of Sc "impurity" atoms into $TiO_2$ lattice: the anisotropic broadening of ND and XRD profiles as well lattice strains were observed. On account of joined ND and XRD refinements we can draw our conclusion that the lattice expansion might vary as a function of maximum strain toward one particular direction within the $TiO_2$ crystal (see Fig.1). Accepting the molecular formula $(Ti^{3+}_{x}Ti^{4+}_{1-x})Sc_xO_{2-x}$ for a tetragonal system we acquired lattice parameters as a function of the temperature (see Fig.2).

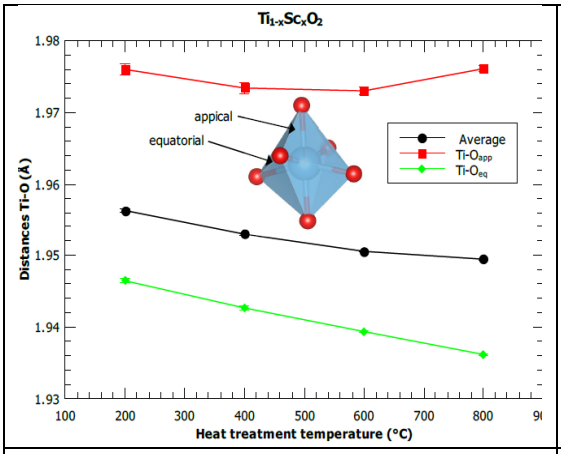


**Figure 1.** Anisotropy in the structure of Sc-doped $TiO_2$

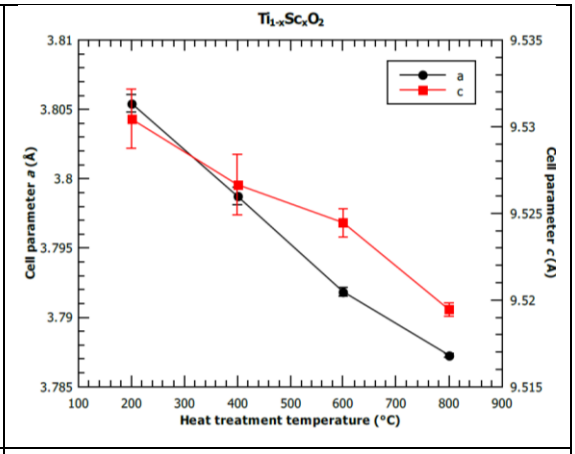


**Figure 2.** Lattice parameters (*a* and *c*) as a function of the temperature